

8-2012

Understanding the Influence of Photon Energy on 6MV Non Reference Dosimetry and CT Dosimetry using TLD and OSLD

Sarah B. Scarboro

Follow this and additional works at: https://digitalcommons.library.tmc.edu/utgsbs_dissertations

 Part of the [Medicine and Health Sciences Commons](#)

Recommended Citation

Scarboro, Sarah B., "Understanding the Influence of Photon Energy on 6MV Non Reference Dosimetry and CT Dosimetry using TLD and OSLD" (2012). *The University of Texas MD Anderson Cancer Center UTHealth Graduate School of Biomedical Sciences Dissertations and Theses (Open Access)*. 275.
https://digitalcommons.library.tmc.edu/utgsbs_dissertations/275

This Dissertation (PhD) is brought to you for free and open access by the The University of Texas MD Anderson Cancer Center UTHealth Graduate School of Biomedical Sciences at DigitalCommons@TMC. It has been accepted for inclusion in The University of Texas MD Anderson Cancer Center UTHealth Graduate School of Biomedical Sciences Dissertations and Theses (Open Access) by an authorized administrator of DigitalCommons@TMC. For more information, please contact digitalcommons@library.tmc.edu.

UNDERSTANDING THE INFLUENCE OF PHOTON ENERGY ON 6MV NON
REFERENCE DOSIMETRY AND CT DOSIMETRY USING TLD AND OSLD

by

Sarah B. Scarboro, M.S.

APPROVED:

Stephen F. Kry, Ph.D.
Supervisory Professor

David Followill, Ph.D.

Dianna Cody, Ph.D.

Laurence Court, Ph.D.

Francesco Stingo, Ph.D.

APPROVED:

Dean, The University of Texas
Graduate School of Biomedical Sciences at Houston

UNDERSTANDING THE INFLUENCE OF PHOTON ENERGY ON 6MV NON
REFERENCE DOSIMETRY AND CT DOSIMETRY USING TLD AND OSLD

A

DISSERTATION

Presented to the Faculty of
The University of Texas
Health Science Center at Houston
and
The University of Texas
M. D. Anderson Cancer Center
Graduate School of Biomedical Sciences
in Partial Fulfillment
of the Requirements
for the Degree of

DOCTOR OF PHILOSOPHY

by

Sarah B. Scarboro, M.S.
Houston, Texas

August, 2012

Copyright (c) 2012 Sarah Scarboro. All rights reserved.

Acknowledgements

I would like to thank my advisor, Dr. Stephen Kry, for his guidance through this work, as well as my entire committee for their helpful discussions, generous contributions, and time committed to my growth as a medical physicist and to this project: Dr. David Followill, Dr. Dianna Cody, Dr. Laurence Court, Dr. Allen White, and Dr. Francesco Stingo.

I want to also acknowledge the financial support received from the PEO International Scholar Award and the American Legion Auxiliary Fellowship. Both of these organizations served to inspire and motivate me dramatically, and I am grateful for both the financial assistance and the vote of confidence for my work and my academic development.

Many thanks go to the RPC staff, especially Ms. Paola Alvarez for being so generous with your time and OSLD knowledge. Also, to Lynda McDonald, Sonia Gonzalez, and Sarah Willis for irradiating countless standards at the Cobalt machine for me, and for all your patience with my continuous questions about reading OSLD.

I want to thank Virginia Mohlere for your tireless editing of all my manuscripts, even after you moved on from the department of Scientific Publications.

I must say a special thank you to Dr. Rebecca Howell for teaching me most of what I know about medical physics. Thank you for your mentorship, your time, and your friendship. I'm also grateful to my classmates for their companionship through this project. And, thank you to Ryan Grant, for keeping me both hydrated and caffeinated through all the dissertation writing.

I want to thank my parents for all their advice and support over the years, and for teaching me that I could do anything I put my mind to. I am where I am today because of the foundation that you provided me. Thank you Bayla, for making sure that I took a walk at least once a day; and thank you Asher, for putting this all into perspective for me. Finally, thank you PJ. There is no doubt you have earned this degree more than I have. Thank you for your perpetual patience, encouragement, and your unique and valuable perspective on my project. You have added more than you know to my

understanding of my own work. Thank you for your frequent and frequently last-minute editing of so many documents, presentations, and spreadsheets, and for helping me prepare for this final academic milestone. I love you.

UNDERSTANDING THE INFLUENCE OF PHOTON ENERGY ON 6MV NON REFERENCE DOSIMETRY AND CT DOSIMETRY USING TLD AND OSLD

Publication No. _____

Sarah Brashear Scarboro, M.S.

Supervisory Professor: Stephen F. Kry, Ph.D.

Abstract

Measurement of the absorbed dose from ionizing radiation in medical applications is an essential component to providing safe and reproducible patient care. There are a wide variety of tools available for measuring radiation dose; this work focuses on the characterization of two common, solid-state dosimeters in medical applications: thermoluminescent dosimeters (TLD) and optically stimulated luminescent dosimeters (OSLD).

There were two main objectives to this work. The first objective was to evaluate the energy dependence of TLD and OSLD for non-reference measurement conditions in a radiotherapy environment. The second objective was to fully characterize the OSLD nanoDot in a CT environment, and to provide validated calibration procedures for CT dose measurement using OSLD.

Current protocols for dose measurement using TLD and OSLD generally assume a constant photon energy spectrum within a nominal beam energy regardless of measurement location, tissue composition, or changes in beam parameters. Variations in the energy spectrum of therapeutic photon beams may impact the response of TLD and OSLD and could thereby result in an incorrect measure of dose unless these differences are accounted for.

In this work, we used a Monte Carlo based model to simulate variations in the photon energy spectra of a Varian 6MV beam; then evaluated the impact of the perturbations in energy spectra on the response of both TLD and OSLD using Burlin Cavity Theory. Energy response correction factors

were determined for a range of conditions and compared to measured correction factors with good agreement.

When using OSLD for dose measurement in a diagnostic imaging environment, photon energy spectra are often referenced to a therapy-energy or orthovoltage photon beam – commonly 250kVp, Co-60, or even 6MV, where the spectra are substantially different. Appropriate calibration techniques specifically for the OSLD nanoDot in a CT environment have not been presented in the literature; furthermore the dependence of the energy response of the calibration energy has not been emphasized. The results of this work include detailed calibration procedures for CT dosimetry using OSLD, and a full characterization of this dosimetry system in a low-dose, low-energy setting.

Table of Contents

Acknowledgements	iii
Abstract	v
Table of Contents	vii
Terms and Symbols.....	xii
List of Figures	xiv
List of Tables	xviii
Chapter 1: Introduction	1
1.1 Purpose Statement	1
1.2 Background and Significance	1
Introduction to TLD and OSLD	1
Use of TLD and OSLD in Radiation Therapy Applications	4
Use of OSLD for CT Dosimetry	6
1.3 Hypothesis and Specific Aims.....	8
Central Hypothesis	8
Specific Aims	9
1.4 Dissertation Organization	10
Chapter 2: Concepts for Methods	12
2.1 RPC Protocol for Point Dosimetry using TLD and OSLD.....	12
2.2 Underlying Assumptions of Burlin Cavity Theory.....	16
2.3 Monte Carlo Simulations of Photon Energy Spectra.....	17
Chapter 3: Variations in photon energy spectra of a 6MV beam and their impact on TLD response ...	20
3.1 Introduction	20

3.2 Materials and Methods	21
Monte Carlo Simulations of Photon Energy Spectra	21
Impact of Variations in Energy Spectrum on the TLD Response.....	22
Dosimeter response based on Photoelectric Effect	22
Determination of Secondary Effects on TLD Response	24
3.3 Results	26
Spectral Variations	26
Impact of Spectral Variations on Energy Response according to Cavity Theory.....	30
Determination of Total Energy Correction Factor	32
3.4 Discussion.....	33
3.5 Conclusion	36
Chapter 4: Characterization of energy response of $\text{Al}_2\text{O}_3\text{:C}$ optically stimulated luminescent dosemeters (OSLD) using cavity theory	38
4.1 Introduction	38
4.2 Materials and Methods	39
Calculation of dose to OSLDs using Burlin cavity theory	39
Determination of the energy response.....	40
4.3 Results	42
Use of cavity theory to determine energy response	42
Dependence of energy response on photon spectra	43
Comparison of calculated and measured energy response.....	44
Comparison to energy response reported in literature	46
4.4 Discussion.....	47
4.5 Conclusions	50

Chapter 5: Energy response of optically stimulated luminescent dosimeters for non-reference measurement locations in a 6MV photon beam	51
5.1 Introduction	51
5.2 Materials and Methods	52
Calculation of the non-reference energy correction factor.....	52
Measurement of the non-reference energy correction factor	54
5.3 Results	55
Energy correction factors determined using Burlin Cavity Theory	55
Comparison of calculated and measured energy correction factors.....	58
5.4 Discussion.....	59
5.5 Conclusions	61
Chapter 6: Characterization of the nanoDot OSL dosimeter for use in CT point dosimetry	62
6.1 Introduction	62
6.2 Methods and Materials	66
Basic characterization of the nanoDot	68
Dependence on Irradiation Geometry	70
Angular Dependence.....	71
Energy dependence	72
6.3 Results	76
Basic characterization	76
Dependence on Irradiation Geometry	80
Angular Dependence.....	80
Energy dependence	81
6.4 Discussion.....	84

6.5 Conclusion	87
Chapter 7: Establishing standard calibration protocols for OSLD nanoDots in computed tomography dosimetry	89
7.1 Introduction	89
7.2 Calibration Formalism	92
7.3 Results and Discussion	103
7.4 Conclusion	109
Chapter 8: Summary and Conclusions	110
8.1 General Summary and Conclusions	110
8.2 Evaluation of the Hypothesis	112
8.3 Future Research and Applications	112
References	114
Appendices	125
Identification of Photon Spectra	125
6MV 10cm × 10cm Open Field Spectra	125
6MV 5cm × 5cm Open Field Spectra	126
6MV 20cm × 20cm Open Field Spectra	127
6MV 10cm × 10cm Open Field Spectra with Lung Heterogeneity	128
6MV 10cm × 10cm Open Field Spectra with Bone Heterogeneity	128
6MV 10cm × 10cm Modulated Spectra	129
Photon Energy Spectra Tabular Data	130
6MV 10cm × 10cm Open Field Spectra	130
6MV 5cm × 5cm Open Field Spectra	134
6MV 20cm × 20cm Open Field Spectra	137

6MV 10cm × 10cm Open Field Spectra with Lung Heterogeneity	139
6MV 10cm × 10cm Open Field Spectra with Bone Heterogeneity	140
6MV 10cm × 10cm Modulated Spectra.....	141
Energy Correction Factors for TLD and OSLD for non-reference conditions in 6MV beam.....	145
6MV 10cm × 10cm Open Field Spectra Non-Reference Energy Correction Factors.....	145
6MV 5cm × 5cm Open Field Spectra Non-Reference Energy Correction Factors.....	146
6MV 20cm × 20cm Open Field Spectra Non-Reference Energy Correction Factors.....	147
6MV 10cm × 10cm Open Field Spectra with Lung Heterogeneity Non-Reference Energy Correction Factors.....	148
6MV 10cm × 10cm Open Field Spectra with Bone Heterogeneity Non-Reference Energy Correction Factors.....	148
6MV 10cm × 10cm Modulated Spectra Non-Reference Energy Correction Factors	149
Vita.....	150

Terms and Symbols

Symbol	Definition	Typical Units
T_{max}	Maximum electron energy	<i>MeV</i>
β	Attenuation coefficient	$\frac{cm^2}{g}$
D_g or D_{cav}	Absorbed dose to the cavity	<i>Gy</i>
D_w or D_{med}	Absorbed dose to the surrounding medium	<i>Gy</i>
d_m or d	Cavity size weighting factor	--
L	Mean chord length	<i>cm</i>
\bar{S}_w^g	Ratio of mass stopping power of the cavity to the mass stopping power of the wall	$\frac{MeV\ cm^2}{g}$
$\left(\frac{\mu_{en}}{\rho}\right)_w^g$	Ratio of the mass energy absorption coefficient of the cavity to the mass energy absorption coefficient of the wall	$\frac{cm^2}{g}$
φ	Particle fluence	$\frac{particles}{cm^2}$
Ψ_E	Particle energy fluence	$\frac{MeV}{cm^2}$
P_{TP}	Temperature, pressure correction factor	--
P_{elec}	Electrometer correction factor	--
D	Absorbed Dose	<i>Gy</i>
T	TLD signal (per unit mass)	<i>counts/mg</i>
S	TLD system sensitivity	$\frac{(counts/mg)}{Gy}$
K_L	TLD dose-linearity correction factor	--
K_F	TLD fading correction factor	--
K_E	TLD energy correction factor	--
K_{NR}	Non-reference energy correction factor	--
K_{PE}	Energy correction factor due to photoelectric interactions	--
K_{SE}	Energy correction factor due to intrinsic and secondary effects	--
M_{raw}	Raw OSLD signal reading	<i>counts</i>
M_{corr}	Corrected OSLD signal reading	<i>counts</i>
C_D	OSLD Calibration Coefficient	$\frac{counts}{Gy}$
k_L	OSLD dose-linearity correction factor	--
k_F	OSLD fading correction factor	--

k_G	OSLD irradiation geometry correction factor	--
k_θ	OSLD angular position correction factor	--
k_E	OSLD energy correction factor	--
$k_{d,i}$	OSLD depletion correction factor	--
$k_{s,i}$	OSLD element sensitivity factor	--

List of Figures

Figure 1.1: Typical photon energy spectrum for 140kVp CT (tungsten anode).	7
Figure 2.1: Capsule containing powder-form LiF TLD.	12
Figure 2.2: Landauer OSLD nanoDot - shown in open (left) and closed (right) position. The dosimeter will remain in the closed position for the entirety of the patient measurements.....	13
Figure 2.3: (a) Acrylic ^{60}Co mini-phantom used for irradiating OSLD standards. An equivalent block to fit TLD capsules is used for TLD standard irradiations. (b) Setup at the ^{60}Co unit with acrylic block positioned on jig.....	15
Figure 3.1: Customized TLD holder	26
Figure 3.2: Variations in photon energy spectra as a function of depth along central axis for a 6 MV 10cm x 10cm field.	27
Figure 3.3: Photon energy spectra at depth of 10 cm in water along central axis for three field sizes.....	27
Figure 3.4: Variations in out-of-field photon energy spectra as a function of distance from the central axis for 10cm x 10cm field.	28
Figure 3.5: Variations in out-of-field photon energy spectra for three different field sizes.	28
Figure 3.6: Variation in photon energy spectra for both an in-field and out-of-field measurement location for an IMRT field compared to 10x10 open field.	29
Figure 3.7: Variation in photon energy spectra with depth along central axis due to presence of bone tissue and lung tissue.....	30
Figure 3.8: Variation of parameter d as a function of incident photon energy (mean bin energy, MeV).....	30

Figure 3.9: K_{PE} for various field sizes in water and presence of heterogeneities, as a function of mean photon energy.....	32
Figure 3.10: Comparison of theoretical energy response (K_{PE}) and total measured response	33
Figure 3.11: Literature comparison of TLD response to photon energy spectra.....	36
Figure 4.1: Variation of d as a function of photon energy for three approximations of the OSLD cavity size.	42
Figure 4.2: Relationship between dose to cavity and dose to medium calculated using Burlin cavity theory for several different sized cavities.	43
Figure 4.3: Three unique photon energy spectra with similar mean energies.....	43
Figure 4.4: Monte Carlo simulated photon spectra for five measurement positions using a Varian 6MV photon beam.	45
Figure 4.5: Aluminum oxide energy response, when compared based on mean energy and not the complete spectrum, shows substantial errors (up to 50%) in the estimated relative response.	48
Figure 4.6: Energy response of two common dosimeters: LiF TLD and Al ₂ O ₃ :C OSLD, calculated using Burlin cavity theory.	49
Figure 4.7: The ratio (Al ₂ O ₃ :water) of mean electron collisional stopping power and mass energy absorption coefficient as a function of photon energy.	50
Figure 5.1: Variation of d as a function of (monoenergetic) photon energy.....	53
Figure 5.2 Custom OSLD holder built to simulate the PTW Farmer chamber dimensions. The holder is constructed of solid water and holds two OSLD nanoDots. Shown disassembled (above) and assembled (below).	55

Figure 5.3 Non-reference energy correction factor (k_{NR}) calculated using Burlin cavity theory as a function of mean spectral energy. The error bars represent the one-sigma uncertainty.	56
Figure 5.4: Comparison of theoretical and measured energy response factor (k_{NR}) for 15 unique positions in 6MV photon beam.	59
Figure 6.1: OSLD nanoDot: (left) active volume visible when open; (right) front and back of closed dosimeter	66
Figure 6.2: Acrylic block used to hold two OSLD nanoDots during ^{60}Co irradiations.	68
Figure 6.3: Custom OSLD nanoDot acrylic holder used for CT measurements. Shown open (top) and closed (bottom).	69
Figure 6.4: Experimental set-up for determining effect of rotating beam irradiation compared to a static beam.	71
Figure 6.5: Experimental set up for determining OSLD signal dependence on angle of dosimeter relative to CT gantry.	72
Figure 6.6: Signal depletion over sequential readings of OSLD nanoDots	77
Figure 6.7: Signal fading as a function of elapsed time since irradiation	78
Figure 6.8: Dose-linearity response over a range of low doses. (a) OSLD reading as a function of delivered dose with linear fit to data. (b) Dose per reading as a function of delivered dose	79
Figure 6.9: Monte Carlo simulated spectra for a 120 kVp beam, standard acrylic 32cm CTDI phantom and two scan extents: a single axial rotation using a 40 mm beam width and a 15 cm helical scan extent (also using a 40 mm beam width).	82

Figure 6.10: Value of energy correction factor (kE) for all simulated scan conditions as a function of mean spectral energy.....	82
Figure 7.1: (a) OSLD setup for free-in-air CT calibration; (b) ion chamber setup using empty cardboard box for free-in-air calibration.....	95
Figure 7.2: Acrylic mini-phantom used for irradiating OSLD standards in ^{60}Co Calibration Protocol.....	96
Figure 7.3: (a) ^{60}Co unit used for standard irradiations; (b) in-air jig to hold acrylic mini- phantom for ^{60}Co irradiations	97
Figure 7.5: Comparison of three OSLD calibration protocols to ion chamber measured dose. Error bars on each dataset represent the total uncertainty for that calibration protocol.....	104

List of Tables

Table 3.1: Calculated KPE for in-field spectral variations (Monte Carlo) due to field size and depth	31
Table 3.2: Calculated KPE for spectral variations (determined via Monte Carlo) occurring at out-of-field locations.....	32
Table 3.3: Total Energy Correction Factor (KNR) for selected locations with varying mean photon energy	35
Table 4.1: Dimensions of the three models for approximating OSLD cavity size and geometry	39
Table 4.2: Relative response (RR) (using a ^{60}Co source ($E = 1.25 \text{ MeV}$) as the standard energy) for three unique spectra calculated using both mean photon energy and full spectral information.....	44
Table 4.3: Comparison of energy response relative to ^{60}Co ($E=1.25\text{MeV}$) for selected measurement positions in a 6MV therapy beam. Measured values were measured using a Varian 21EX accelerator, calculated values were determined using spectra generated using a benchmarked Monte Carlo model of a Varian 6MV accelerator.	46
Table 4.4: Comparison of calculated energy response relative to ^{60}Co ($E=1.25\text{MeV}$) determined using cavity theory for OSLD to measured values reported in the literature for photon beams of varying energies.	46
Table 5.1. Calculated energy response factor (kNR) values for spectral variations (determined via Monte Carlo simulations) occurring at selected in-field locations for a 6-MV photon beam.....	57
Table 5.2. Calculated energy response factor (kNR) values for spectral variations (determined via Monte Carlo simulations) occurring at selected out-of-field locations for a 6-MV photon beam.....	58

Table 6.1: Scan parameters, CTDI phantom, position in phantom, and mean spectral energy for conditions simulated using benchmarked MCNP model of GE VCT scanner. Center and peripheral positions in phantom correspond to center and peripheral (1cm depth) chambers in the CTDI phantoms.	74
Table 6.2: Average signal counts, average, and maximum coefficient of variation (CoV) for low-dose irradiations using both CT and ^{60}Co and high-dose irradiations using ^{60}Co	78
Table 6.3: Ratio of full rotation OSLD signal to static beam OSLD signal (see Figure 6.4) under various conditions for three nominal CT energies.	80
Table 6.4: Relative OSLD signal for dosimeters oriented at 0° , 45° , and 90° relative to the signal at 0° (see Figure 6.5) for two nominal energies and two irradiation conditions (in air and in the center of the 16cm diameter CTDI phantom).	81
Table 6.5: Comparison of measured and calculated energy correction factors for a range of clinical CT scanning parameters. Peripheral position denotes chamber located at 1cm depth from phantom surface. Mean spectral energy is defined at the dosimeter position.....	83
Table 7.1: Measurement conditions for calibration protocol validation measurements	99
Table 7.2: Energy correction factor values for two different calibration protocols	101
Table 7.3: Comparison of measured OSLD dose using three independent calibration protocols with ion chamber measured absolute dose for subset of 11 measurement conditions.	105
Table 7.4: Values of energy correction factor relative to the CT-based calibration protocol for a range of CT parameters.....	107
Table 7.5: Values of energy correction factor relative to the ^{60}Co based calibration protocol for a range of CT parameters.....	107

Table 7.6: Relative uncertainties in corrected OSLD signal, calibration coefficient, and dose
determination for each calibration protocol.....108

Chapter 1: Introduction

1.1 Purpose Statement

The use of photon radiation in medical applications utilizes photon beams that consist of a range of energies. The selection and characterization of photon energy is a fundamental aspect of effective use of radiation in both radiation therapy and diagnostic imaging. Measurement devices in medical applications often depend on photon energy, and careful characterization and calibration is necessary such that the dosimeter response provides accurate dosimetric information.

Thermoluminescent dosimeters (TLD) and optically stimulated luminescent dosimeters (OSLD) are commonly used passive solid state dosimeters for measuring radiation dose. Each of these dosimeters offers multiple benefits to clinical dosimetry; however, both TLD and OSLD carry an inherent energy dependence which must be appropriately accounted for. Complete characterization of the dosimeter response to a range of photon energies is needed for accurate dosimetry; additionally, detailed calibration procedures should be specific to the dosimeter application.

This work has two main objectives. First, to evaluate the impact of spectral variations in a clinical radiotherapy beam on two common dosimeters: TLD and OSLD. This investigation will determine whether the general disregard for variations in photon energy spectra has introduced large errors into dose measurement in a radiotherapy environment. Second, this work sought to characterize the OSLD nanoDot in a CT environment and to provide detailed calibration protocols for performing CT dosimetry with the nanoDot.

1.2 Background and Significance

Introduction to TLD and OSLD

Medical use of radiation is both fundamental and indispensable in modern cancer treatment regimens. Ionizing radiation is used in almost every aspect of diagnosis, staging, tumor delineation, and treatment of cancer. The measurement of radiation dose to patients is crucial to providing safe

and effective care – both for applications utilizing relatively low doses of radiation (diagnostic imaging) and applications depending on high doses of radiation (radiation therapy). A number of devices are employed to measure radiation in the medical industry, including active devices such as ionization chambers or other electronic devices, and passive devices such as film, diodes, MOSFETS, and other solid state dosimeters. This work will examine characteristics of two passive solid state dosimeters – LiF and $\text{Al}_2\text{O}_3\text{:C}$.

A passive dosimeter is one that works as both a sensor and a storage device for dosimetric information, accumulating data until the point that it is ‘read out’. The two materials of interest to this work, LiF and $\text{Al}_2\text{O}_3\text{:C}$, are crystals which exhibit properties of thermoluminescence (TL) or optically stimulated luminescence (OSL), respectively. These phenomena are similar in the method that dosimetric information is stored, and differ only in the read-out mechanism. When irradiated, free electrons in the crystal structure are excited and become ‘trapped’ in a meta-stable energy state due to defects in the lattice structure. At a later point, the material can be stimulated (either by heat in the case of thermoluminescent materials or light for optically stimulated luminescent materials) such that these electrons are liberated, recombine with nearby particles of the opposite sign and emit a characteristic luminescence (light). The intensity of the emitted signal is monitored as a function of time, and can be related to the amount of trapped charge in the material, which is directly proportionally to the absorbed radiation dose^{1;2}.

TLD and OSLD have similar advantages for use in diagnostic and therapy environments. These dosimeters are small, inert, widely available, and relatively inexpensive. As previously mentioned, TLD are commonly used to verify proper calibration of radiation output, and have historically been the standard dosimeter used by the Radiological Physics Center (RPC, MD Anderson Cancer Center; Houston, TX) for credentialing institutions for clinical trials³. Traditionally, OSLD have been used as the dosimeter in radiation workers’ monitoring devices, but have gained popularity for dose measurement in clinical settings, including radiation therapy and diagnostic imaging largely due to the simpler and non-destructive readout method⁴. OSLD demonstrate sensitivity to a wide range of

absorbed dose values, even to very small doses like those generally found in diagnostic imaging^{5; 6}. In clinical practice, TLD and OSLD are safe to use on (or inside) patients during therapy or imaging procedures, and they can provide an estimate of the absorbed dose to tissue at the location where the dosimeter is placed^{2; 7}.

One of the primary advantages of OSLD over TLD is the stimulation by light rather than heat. The sensitivity of TLD is highly dependent on its thermal history as well as the heating rate and temperature during readout⁸, and improper heating may result in damage to the detector. The use of light for dosimeter readout is preferable as it avoids these risks to both dosimeter integrity and accuracy of results. OSLD offer a higher luminescent sensitivity relative to TLD, such that all dosimetric traps do not need to be liberated in a single simulation. As a result, OSLD may be read multiple times with minimal signal loss, and can therefore serve as a long-term dosimetric record. Total purging of the dosimetric signal requires only UV light, and OSLD can be bleached in a relatively short time frame (hours) and then reused⁹. On the basis of their overall stability, easier readout process, and the ability to read a single dosimeter multiple times, OSLD have recently replaced TLD in the remote verification mailing service operated by the RPC¹⁰.

The RPC is a National Cancer Institute (NCI) funded organization that has been tasked with providing external quality audits to institutions participating in NCI clinical trials, and is arguably one of the largest users of both TLD and OSLD. The RPC currently services nearly 1900 institutions both in the United States and abroad. One of the primary tools used at the RPC to accomplish this task is a mailable TLD and OSLD audit service. The mailable system consists of acrylic phantoms loaded with either TLD or OSLD at various depths. Institutions set up the phantom, irradiate it as specified, and then return it to the RPC, where the dosimeters are read and analyzed. The delivered dose is compared to the institution's stated beam output as an independent check. The RPC has over 30 years of experience using TLD and more recently, 3 years' experience using OSLD, auditing over 14,000 beams in 2011. The basic dosimetry protocols used in this work for both TLD and OSLD, (including characterization and calibration approaches) are based on the RPC protocols.

TLD and OSLD must be calibrated using a known dose of radiation and a standard protocol to establish the sensitivity of the reader. Proper calibration also monitors the stability of the reading system, ensuring that there is not significant drift in the reader over a reading session. The RPC uses an ADCL-maintained ^{60}Co beam as a calibration source, and has a well defined standard calibration set up and protocol. The dosimeter calibration for experiments investigating radiotherapy beams are consistent with the RPC protocol, and are further described in Chapter 2.

Given the dependence of TLD and OSLD on the energy characteristics of the incident photon spectra, two applications (therapy and diagnostic environments) will be considered separately. In external beam radiation therapy, photon beams are considered to be high-energy (megavoltage) and penetration of tissue largely depends on beam energy. Conversely, low-energy photon beams (in the kilo-voltage range) are more commonly used in diagnostic imaging. First, the use of both dosimeters in a radiation therapy environment will be considered through an investigation of variations in the photon energy spectra of a 6MV radiotherapy beam. Subsequently, the use of OSLD for CT dosimetry will be investigated, and appropriate standard calibration procedures developed.

Use of TLD and OSLD in Radiation Therapy Applications

TLDs have a long history of use in both *in-vivo* and *in-vitro* dose measurement in radiation therapy applications. TLD work well as an *in-vivo* dosimeter on account of their small size, high sensitivity and the lack of wires or accompanying electronics. TLD are easy to affix to a patient's skin surface, and have been used to measure skin dose as well as to estimate dose to other organs, both *in-vivo*¹¹⁻¹⁶ and using anthropomorphic phantoms¹⁷⁻¹⁹. TLD have also been widely used as an out of field dosimeter, used to measure leakage and scatter radiation to locations beyond the primary field border²⁰⁻²⁴. They work well as an out of field dosimeter due to their small size and relatively high sensitivity. OSLD have seen growing clinical use in recent years^{25; 26}, and will likely see increased clinical use in the future.

In the therapy environment, variations in photon energy spectra occur through attenuation of the primary beam that is not uniform with energy, as well as the introduction of scatter and leakage into the primary field as a result of changes in beam parameters (field size, collimation, field modulation), measurement location, and the presence of heterogeneous materials in the beam path. As a result, the photon energy spectrum existing within the patient or at a point of measurement other than the calibration location may be vastly different from the primary energy spectrum under reference conditions.

Some recent studies have demonstrated variations in the photon energy spectra of therapeutic radiotherapy beams; however the range of conditions examined in the literature is limited. Liu et al and Yang et al sought to examine spectral variations for small field sizes, such as those used in intensity-modulated radiation therapy (IMRT)^{27; 28}. Other studies have also demonstrated that variations exist as a function of field size, depth, and distance away from central axis for large symmetric fields^{27; 29}. The presence of heterogeneities, such as lung or bone tissue, may also perturb the photon energy spectra compared to homogeneous tissues or soft tissue. The extent of variations in the photon energy spectra for a complete range of clinical conditions has not been thoroughly examined, especially for megavoltage therapy units.

When using an energy-dependent dosimeter such as TLD or OSLD, the measurement of dose is corrected by an ‘energy correction factor’ (k_E , further described in Chapter 2) which is based on the photon energy spectrum occurring under standard reference conditions. Current protocols for dose measurement using TLD and OSLD generally assume a constant photon energy spectrum within a nominal beam energy regardless of measurement location, tissue composition, or changes in beam parameters. Variations in the energy spectrum of therapeutic photon beams may impact the response of TLD and OSLD and could thereby result in an incorrect measure of dose unless these differences are accounted for. We hypothesize that this assumption has introduced error of at least 5% into dose measurement using these dosimeters.

A thorough evaluation of the impact on both TLD and OSLD from IMRT fields is of particular importance due to the large number of such treatments employed in clinical practice. Additionally, most NCI and Cooperative Group sponsored clinical trials allow IMRT treatments. The credentialing procedure for institutions participating in such trials includes dose verification through irradiation of TLD or OSLD, a program that is monitored by the RPC. Unless the variations in photon energy for IMRT fields are better understood and accounted for in TLD and OSLD dose measurement, these dose readings may be largely inaccurate.

Use of OSLD for CT Dosimetry

CT imaging offers high-quality images at a relatively fast acquisition time, especially since the advent of multi-detector row CT (MDCT) systems. The main drawback of CT imaging is the radiation dose to the patient. According to UNSCEAR (2008), CT imaging accounts for less than 10% of diagnostic x-ray examinations, but it contributes almost 50% of the collective radiation dose³⁰. Patient-specific dosimetry for diagnostic CT procedures is limited, and current methods for estimating patient dose are usually based on measurements made in homogeneous cylindrical acrylic phantoms (Computed Tomography Dose Index (CTDI) phantoms). This approach provides a good estimate of the scanner output, but extrapolation of these measurements to estimate the actual patient dose is unreliable and likely inaccurate³¹. Given the large number of diagnostic studies (65 million adult CT studies and 5 million pediatric CT studies in 2009)³², there is a growing need for a more accurate measurement of radiation dose during CT examinations.

In this work, Landauer's OSLD nanoDots (Landauer Inc., Glenwood, IL) are considered as a possible alternative solution for achieving high-accuracy CT dosimetry. Implementation requires the entire dosimetry system to be characterized for both the low-dose and low-energy environment characteristic of CT. Also, in addition to the basic characterization, the over-response of the dosimeter to low-energy photons must be addressed. Photon energy spectra in diagnostic imaging applications are lower in energy than radiotherapy photon beams, but still contain a range of photon energies.

Several studies in the literature have presented algorithms or computational methodologies for determining CT spectra given the difficulty of direct spectral measurements³³⁻³⁷. The results of these simulations vary, and validation is often conducted through a comparison of dose measurements.

A typical computed tomography (CT) spectrum for a peak target potential of 140kVp is shown in Figure 1.1³⁵. This spectrum is not computationally determined, but rather based on an interpolation model of empirical data that was measured by Fewell et al^{34; 38}, which are tabulated for energies as low as 2keV.

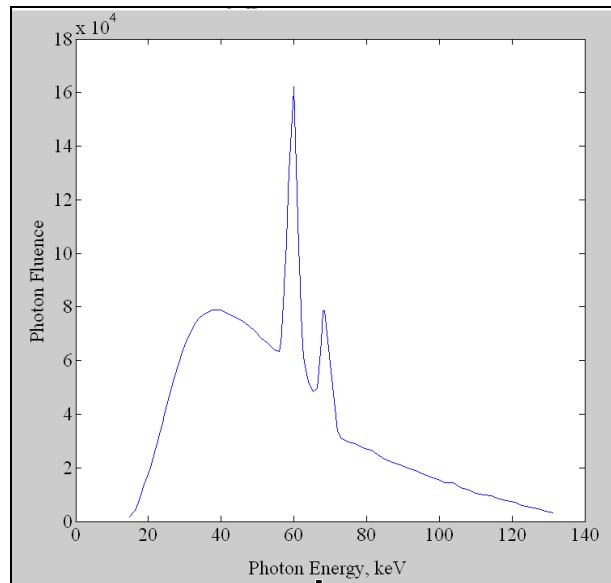


Figure 1.1: Typical photon energy spectrum for 140kVp CT (tungsten anode).

While several interpolation models have been generated based on this dataset; the results cannot be directly validated, and are not specific to a particular set of scan parameters. Our study will rely on spectra simulated using Monte Carlo and based on a benchmarked algorithm developed at the University of California, Los Angeles^{39; 40}.

In its entirety, this work is aimed at improving the care and safety of cancer patients – especially those undergoing radiation therapy, but also those undergoing diagnostic procedures and exams that involve ionizing radiation. With superior accuracy and understanding of the radiation dose to patients

for all of the applications mentioned, clinicians will be better equipped to make decisions and design treatments that will optimize the control of disease and limit the risk of any adverse effects, thus improving the quality of life for these patients both during their treatment and for the years following.

1.3 Hypothesis and Specific Aims

Measurement of the absorbed dose from radiotherapy beams is an essential component of providing safe and reproducible treatment. Measurement techniques using TLD are common and widespread in radiation therapy as a method for determining, verifying, reporting, and tracking photon radiation dose to patients being treated for cancer. OSLD have seen increased use in recent years in radiation therapy applications. Diagnostic imaging dosimetry, particularly for CT, remains deficient, but may be substantially improved with the introduction of OSLD to this environment. Measurements made with these dosimeters in a radiation therapy environment rely on a standard assumption that the photon energy spectrum is constant, being based on a single reference condition, and ignore the potential impact of variation in the photon energy spectra with the measurement location or treatment parameters. This assumption is not valid, and may be introducing substantial error into measured radiation doses. Furthermore, OSLD have not been fully characterized for use in a CT environment, and calibration procedures are not standardized.

Central Hypothesis

The assumption of a single and constant photon energy spectrum introduces an error of at least 5% into dose measurements using TLD and OSLD in typical radiotherapy photon beams. In a CT setting, OSLD nanoDots can be used to measure dose with total uncertainty of less than 20% compared to ion chamber readings.

Specific Aims

This hypothesis will be tested through the following specific aims:

1. *Investigate variations in photon energy spectra resulting from non-reference measurement conditions for megavoltage radiation therapy treatment units due to measurement location, treatment parameters, and the presence of heterogeneous materials.*
2. *Assess the variability in the energy correction factor using both cavity theory and direct measurement for two common dosimeters (TLD and OSLD) due to variations in the energy spectra in 6MV radiation therapy photon beams.*
3. *Characterize the OSLD nanoDot for use in routine clinical CT dosimetry and define useful correction factors for signal depletion, linearity, angular dependence, and energy dependence.*
4. *Describe a calibration procedure that is both realistic and viable for imaging facilities and determine the associated uncertainty after necessary correction factors have been applied.*

At its core, this project seeks to determine whether a standard assumption used in common measurements of radiation dose is valid and defensible for the applications being used in clinical settings today. This research will seek to expose vulnerabilities in the assumption of a constant photon energy spectrum and establish better criteria for conditions when this assumption is acceptable and when it is not, and provide a method to correct the measured dose for those conditions where constant photon energy should not be assumed. The results of this work are relevant and directly applicable to clinical dose measurements. This work provides useful correction factors for non-reference positions in a radiotherapy environment, and establishes standard calibration protocols and correction factors for using OSLD to measure dose in a CT setting.

1.4 Dissertation Organization

This dissertation is meant to serve as a permanent record of the body of work that was undertaken to evaluate the hypothesis of the project. Chapters 3 through 7 are self-contained studies, each including an introduction, methods, results, discussion, and conclusions. These chapters each describe a specific portion of the work required to complete this project.

Chapter 2, Concepts for Methods, contains detailed methodology beyond what is presented in each self-contained study. This includes parameters and assumptions used for the photon energy simulations, underlying assumptions of Burlin Cavity Theory, and details of the measurement techniques. Additionally, the general protocol for dose determination using TLD and OSLD is described.

Chapter 3 is a study of specific aims 1 and 2, providing a derivation for the energy correction factor from fundamental Burlin Cavity Theory, and addressing the use of TLD in a radiotherapy environment.

Chapter 4 describes the determination of the energy response of the OSLD nanoDot from fundamental Burlin Cavity Theory, addressing specific aim 2 for OSLD. Chapter 4 also serves as a validation for the cavity theory-based approach for OSLD through a comparison to both measured data and reported literature values.

Chapter 5 is a study of specific aim 2 and describes the application of a non-reference energy correction factor for measuring out-of-field dose in a radiotherapy environment.

Chapters 6 and 7 address the use of OSLD in a CT environment. The basic characterization of the OSLD nanoDot is described in Chapter 6, and directly addresses specific aim 3.

Chapter 7 presents standard calibration protocols for CT dose determination along with details uncertainty analysis for each protocol and addresses specific aim 4.

Finally, Chapter 8 is a summary of the research project as a whole. This section evaluates the hypothesis, draws meaningful conclusions from the comprehensive study, and explores future related work. Selected photon energy spectra and values of the energy correction factor appear within each

chapter; however, a comprehensive of all data generated during this investigation appears in the appendices.

Chapter 2: Concepts for Methods

2.1 RPC Protocol for Point Dosimetry using TLD and OSLD

LiF TLD and Al_2O_3 OSLD can be manufactured in different configurations, such as rods, chips, thin strips, discs, and powder form, depending on the application. For the purposes of this work, capsules containing powder-form LiF were used (Figure 2.1). Capsules measure 2.5cm in length and 4mm in diameter and contain roughly 22mg of LiF powder.



Figure 2.1: Capsule containing powder-form LiF TLD.

LiF TLD capsules are still used for third party verification by Radiation Dosimetry Services (MD Anderson Cancer Center, Houston, TX), and in various dosimetry phantoms by the RPC. TLD capsules are also often used in phantoms and for patient dose verification in a clinical setting.

The OSLD used in this study are composed of a carbon-doped aluminum oxide crystal ($\text{Al}_2\text{O}_3:\text{C}$) which is enclosed in a black, light-tight plastic cassette. The cassette prevents signal fading from light exposure following irradiation, or during storage. These dosimeters, the OSLD nanoDot, are commercially available from Landauer, Inc. (Glenwood, IL). The total dosimeter dimensions are approximately $10\text{mm} \times 10\text{mm} \times 2\text{mm}$, and the dosimeter is shown in the open (left) and closed (right) position in Figure 2.2.

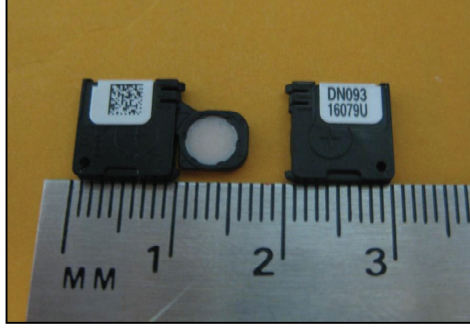


Figure 2.2: Landauer OSLD nanoDot - shown in open (left) and closed (right) position. The dosimeter will remain in the closed position for the entirety of the patient measurements.

The crystal itself used in TLD and OSLD is manufactured in batches, where a particular batch of material possesses inherent qualities that may affect the dosimetry response. In order to understand these variations in response, a complete characterization of a batch of material should be performed before using the dosimeters in dose measurements. When characterizing either TLD or OSLD, the response of the dosimeter with respect to dose (dose-linearity), time since irradiation (fading), and photon energy (energy dependence) should be examined. In addition to these factors, the signal depletion as a function of number of readings should be characterized for the OSLD nanoDot.

As described in the introduction, there is a long history of point dosimetry using both TLD and OSLD at the RPC. In this study dose was determined using a single approach which is consistent with the RPC methodology and with the recommendations of the upcoming report of AAPM Task Group 191. For all TLD measurements in this work, dose (D) was determined using Equation 2.1, where (T) is the LiF signal per mass, (S) is the system sensitivity, (k_L) is the linearity correction factor, (k_F) is the fading correction factor, and (k_E) is the energy correction factor.

$$D = T \times S \times k_L \times k_F \times k_E \quad (2.1)$$

Dosimeter linearity, fading, and energy response are generally determined experimentally for the batch as a whole, and empirically-based correction factors are applied to subsequent dosimeter readings. Detailed expressions for these factors appear in the literature⁴¹ and are calculated on a batch-by-batch basis. In this work, the batch-specific correction factors for fading and linearity that were previously determined by the RPC were used for TLD readings. The RPC energy correction factors

were not used. Rather, the energy response of TLD was one of the primary focuses of this work, particularly for non-reference measurement conditions; this is the subject of the investigation provided in Chapter 3.

Dose (D) to an OSLD nanoDot was determined using Equation 2.2, which is of the same form as Equation 2.1, with a few minor changes.

$$D = \overline{M}_{corr} \times C_D \times k_L \times k_F \times k_G \times k_\theta \times k_E \quad (2.2)$$

When determining dose to the OSLD, the average of three readings is used, rather than a single reading as for TLD. Also, each reading is individually corrected for system depletion using an empirically determined factor, $k_{d,i}$. As described further in Chapter 6, the depletion is largely dependent on the strength of the LED light used to stimulate the dosimeters. For dosimeters irradiated to a low dose, a stronger LED is used, and as a result larger signal depletion occurs with each reading. Depletion for the weak beam was previously characterized by the RPC for the reader used in this work; characterization of the strong beam depletion was completed as part of the analysis of CT dosimetry using this system.

The average signal is then multiplied by an element correction factor ($k_{s,i}$) which accounts for that unique element's sensitivity compared to the mean of the batch. This factor is also empirically determined for each dosimeter during batch commissioning. It is RPC practice to determine a unique element sensitivity factor for every element in a batch (~10,000 elements per batch).

Linearity (k_L) and fading (k_F) were empirically determined by the RPC for therapy-applications of the OSLD system, these factors were applied to experimental measurements performed in a 6MV beam. The correction factors for irradiation geometry and angular dependence (k_G and k_θ , respectively) are only necessary in CT dosimetry, and are fully described in Chapter 6. Finally, the energy correction factor of OSLD was one of the primary focuses of this work, and is the subject of Chapters 4 and 5, in particular.

System sensitivity (S for TLD or C_D for OSLD) was determined using a standard calibration protocol. Unless otherwise specified, calibration for both TLD and OSLD was performed using a Theratron 780C cobalt unit (AECL/Theratronics International Ltd., Kanata, Ontario, Canada) and an acrylic ‘mini-phantom’. The mini-phantom (Figure 2.3a) holds two dosimeters side-by-side for simultaneous irradiation. The dosimeters are at a depth of 0.75cm in acrylic, and placed on an in-air jig for irradiation. The jig (Figure 2.3b) attaches to the cobalt unit such that its surface is 80.0cm from the source, and therefore the dosimeters are set to 79.25cm from the source. For all irradiations, the mini-phantom is placed in a slight recess in the platform to minimize set up uncertainties, and the field size is set to 10cm \times 10cm at the platform surface.



Figure 2.3: (a) Acrylic ^{60}Co mini-phantom used for irradiating OSLD standards. An equivalent block to fit TLD capsules is used for TLD standard irradiations. (b) Setup at the ^{60}Co unit with acrylic block positioned on jig.

The desired dose to the standards was determined by applying a decay correction to the calculated dose rate of the source and then setting the timer to the appropriate value to deliver the required dose. The dose rate to muscle at the location of the dosimeters was previously determined by the RPC to be 147.9 cGy/min on October 15, 2005. The cobalt unit uses a solid state timer which achieves a reproducibility of better than 0.1%, however for very low doses only a short irradiation time is necessary, and thus, the time required for the source to move into and out of position increases this

uncertainty. The dose delivered to standards used for experiments in the therapy environment was 100 cGy; the dose delivered to standards for CT experiments was 45 mGy.

2.2 Underlying Assumptions of Burlin Cavity Theory

Burlin Cavity Theory was used as a basis for a theoretical determination of the energy response of a small solid state dosimeter. This particular cavity theory was derived by Burlin in 1968 as a theory that would bridge the gap between Bragg-Gray theory (intended for small cavities) and large cavities, for which the effect of the wall is negligible⁷. In effect, Burlin Cavity Theory was meant for medium-sized cavities, where the dose to the cavity can be determined by use of a ‘weighted sum’ of the contribution to dose of electrons crossing the cavity and created in the cavity wall.

The underlying assumptions behind Burlin theory include several which are also in place for small cavity theory, such as the assumption of homogeneous media composing the cavity and the surrounding material. The remaining underlying assumptions of Burlin Cavity Theory are as follows⁷:

- Charged Particle Equilibrium (CPE) exists surrounding the cavity at distances greater than the range of an electron with highest energy, T_{\max} .
- The equilibrium spectrum of secondary electrons is consistent both within the cavity and the surrounding medium.
- The energy fluence entering the cavity from the cavity wall is assumed to be attenuated exponentially through the cavity; in other words, there is no change in the spatial distribution of this fluence.
- Likewise, the energy fluence originating within the cavity builds up to the equilibrium value exponentially as a function of distance into the cavity. These parameters are related by the coefficient, β .

In its simplest form, Burlin Cavity Theory is stated as follows (Equation 2.3):

$$\frac{\bar{D}_g}{D_w} = d \cdot \left(\frac{\bar{S}}{\rho} \right)_w^g + (1-d) \left(\frac{\bar{\mu}_{en}}{\rho} \right)_w^g \quad (2.3)$$

Burlin Cavity theory is known for being especially useful for estimating the dose to condensed-state dosimeters (such as TLD and OSLD), and as a result, this theory was useful for understanding the impact of energy on the dose measured by these dosimeters. Essentially, if the dose to a solid state dosimeter can be calculated using Burlin Cavity Theory, then the energy correction factor, which by definition is the ratio of the dose under two different photon energy spectra, can also be calculated. This is the fundamental approach of the determination of energy response in this work; a complete derivation of the energy correction factor from the general form of Burlin Cavity Theory appears in Chapter 3, Equations 3.4 to 3.11.

There is some inherent uncertainty in the tabulated data (mass energy absorption coefficients and restricted stopping powers) that are used in the cavity theory. All of the data for this study was taken from NIST-traceable sources, and the uncertainty that is introduced from this data is thought to be very low. The largest uncertainty for this data is likely at low energies; in fact, this data is generally unavailable for energies less than 5-10keV. As a result, this methodology would not be appropriate for predicting the response of these dosimeters to very low-energy spectra, such as those encountered in mammography.

2.3 Monte Carlo Simulations of Photon Energy Spectra

The first aim of this work was to characterize the photon energy spectra for both in-field and out-of-field measurement locations for clinically relevant scenarios using computational simulations. To accomplish this, a Monte Carlo based model of a Varian 6MV linear accelerator was used⁴²⁻⁴⁴. This model was previously built at our institution using the MCNPX⁴⁵ code and was benchmarked for in-field and out-of-field dose calculation through comparison to direct dose measurements^{42; 43}. The model geometry incorporates all major beam-line components including X- and Y- jaws, a 120-leaf

multileaf collimator (MLC), head-shielding, and structural components. Also, a large (50cm x 70cm x 50cm) volume of water, intended to represent a water phantom, was simulated at a position 100cm SSD below the target.

For this work, cells were added within the water phantom to allow tallies at various locations. Particles were tallied using an F4 tally (particle flux with units particles/cm²) in each cell, using a logarithmic bin structure, with 30 energy bins between 0.001 MeV up to 10 MeV. A total of 9×10^8 particle histories were completed for each simulation, such that the average bin error in particle flux was less than 2%, including cell locations farthest away from the primary radiation beam. Photon and electron cut-off energies were specified at 0.005 MeV using the phys cut:e and cut:p cards.

Two cylindrically shaped cells were included on central axis, at depths of 0.5 cm and 1.6 cm below the water surface. The volume of these two tallies was 1.57 cm³. All other tallies were rectangular parallelepiped (RPP) shaped. This included eight additional cells along the central axis, with depths centered at 3 cm, 5 cm, 8 cm, 10 cm, 12 cm, 15 cm, 20 cm, and 25cm. Tallies along central axis were 3 cm width × 3 cm length × 1 cm depth (for a cell volume of 9cm³). Tallies were also included at three depths (1.6 cm, 5 cm, and 20 cm) for a range of distances away from central axis. Each of these cells was larger in size, such that sufficient tally data was collected within a reasonable computing time. These tallies were placed at 5 cm, 10 cm, 15 cm, 20 cm, 25 cm, 30 cm, 40 cm, and 50 cm away from central axis, and were each RPPs with dimensions 3 cm width × 3 cm length × 2 cm depth (for a cell volume of 18 cm³).

To ensure an investigation of a range of photon energy spectra, simulations were completed for three field sizes (5 cm × 5 cm, 10 cm × 10 cm, 20 cm × 20 cm). The field size was specified by the X- and Y- jaw settings, and for the 10 cm × 10 cm field size, the MLC was completely retracted. For the 5 cm × 5 cm field size, the MLC was also retracted to reduce scatter as much as possible and simulate conditions where the spectra would be relatively hard. Conversely, for the 20cm × 20cm field size, the MLC was also set to a 20cm × 20cm field size to maximize the amount of in-field scatter, creating photon energy spectra that were relatively soft.

In addition to the simulations with various field sizes, a set of photon energy spectra were generated in the presence of bone and lung heterogeneities. The superior 9 cm of water in the simulated water phantom was replaced with either bone material (density 1.7 g/cm^3) or lung material (density 0.26 g/cm^3) in two separate simulations. Nine centimeters was selected to represent a ‘worst case scenario’ or a condition that would perturb the radiation spectrum more severely than anything expected to occur in a clinical setting. Photon energy spectra were tallied in all cells existing beneath the heterogeneity; as a result, the tallies at a depth of 1.6cm or 5cm were not used for these simulations.

A comprehensive list of the photon energy spectra that were generated in this work appears in Appendix A of this work.

Chapter 3: Variations in photon energy spectra of a 6MV beam and their impact on TLD response

Chapter 3 was published in the journal of Medical Physics in May 2011. [MedPhys. 38(5) 2619-2628 (2011)]. Written permission has been obtained from the journal for use of these materials in this dissertation.

3.1 Introduction

Recently published data have demonstrated variations in the photon energy spectra of therapeutic radiotherapy beams. These variations are especially pronounced for small field sizes, such as those used in intensity-modulated radiation therapy (IMRT)^{27; 28}, but variations also exist as a function of field size, depth, and distance away from central axis for large symmetric fields^{27; 29}. The presence of heterogeneities, such as lung or bone tissue, may also perturb the photon energy spectra compared to homogeneous tissues or soft tissue. Outside of the treatment field the photon spectra is likely to be very different from the spectrum on the central axis. Out-of-field radiation is known to be composed of leakage radiation from the head of the treatment machine and scatter produced from the collimator system or inside the phantom or patient⁴⁶. While head leakage has a comparable spectrum to the primary beam, scattered radiation has a much lower (softer) energy spectrum. These variations in the energy spectrum of a therapeutic radiotherapy beam will impact the response of energy-dependent dosimeters and could thereby result in an incorrect measure of dose unless these variations are accounted for.

Thermoluminescent dosimeters (TLDs) are one such type of energy-dependent dosimeter, and they are widely used for dose measurement because of their availability, small size, and accuracy. TLDs use the principles of thermoluminescence to estimate the absorbed dose to the reference medium at the location of the TLD. While many materials exhibit thermoluminescent properties, the most widely used in medical applications is lithium fluoride (LiF). LiF has an effective atomic number similar to that of soft tissue (8.3 versus 7.2), indicating that there is a close correlation between the energy deposited in LiF and that deposited in soft tissue^{2; 7; 47}. To determine absorbed dose (D), the raw TLD signal (T), is multiplied by the system sensitivity factor (S). A series of correction factors must also be applied to account for the specific application of the TLD (Equation 3.1); these include linearity (K_L), fading (K_F), and energy response (K_E), which are generally determined during commissioning of the TLD⁴¹.

$$D = T \times S \times K_L \times K_F \times K_E \quad (3.1)$$

In this work we investigated the final correction factor: energy response. The standard energy response factor (K_E) is required to account for differences in the TLD response to the experimental beam energy (6MV, for example) relative to the reference beam energy (e.g., ^{60}Co). This standard energy correction factor is commonly established by measuring the response of the TLD to a known dose of 6MV photons (determined on the central axis at a depth of maximum dose for a 10cm x 10cm field) versus the response of the TLD to a known dose of ^{60}Co photons (determined under the same reference conditions). The basic definition of the energy response factor is given in Equation 3.2⁴¹.

$$K_E = \frac{D^{6MV} T^{Co-60}}{D^{Co-60} T^{6MV}} \quad (3.2)$$

In practice, this single energy response/characterization is used for any measurement conducted at a nominal beam energy (e.g., 6MV). Either a single energy response is used, or if both experimental and reference TLD are irradiated at the same nominal energy, a value of 1 is assumed. This is done regardless of difference in field size, depth, measurement position inside or outside the treatment field, and regardless of any tissue or phantom heterogeneity. Inherent to this use of a single energy correction factor is the assumption that there is no variation in the energy spectra at that given nominal beam energy. This is clearly not a valid assumption, but the impact of this faulty assumption has not been evaluated.

The objectives of this study were, first, to evaluate the variability in the energy spectrum of a Varian 6MV beam as a function of the treatment field size, measurement location, field modulation, and presence of heterogeneities; and second, to evaluate the impact of these variations in photon energy spectra on the response of a common energy-dependent dosimeter, TLD.

3.2 Materials and Methods

Monte Carlo Simulations of Photon Energy Spectra

Photon spectra were calculated using a Monte Carlo model of a Varian 6MV linear accelerator that was developed using the Monte Carlo N-Particle Extended (MCNPX) transport code⁴⁵ and was benchmarked for in-field dose calculations within 2% and out-of-field dose calculations within 16%^{42; 43}. The model geometry incorporated beam-line components including a 120 leaf multileaf collimator (MLC), head-shielding, and structural components, and was used to calculate photon energy spectra in water at several locations and for various treatment parameters. A large water phantom (50cm width x 70cm length x 50cm depth) was simulated at 100 cm source to surface distance (SSD). Photon flux-tally voxels were added throughout the water phantom, including in-field as well as out-of-field locations, to capture the full range of energy spectra that could be clinically encountered. The spectra were calculated from 0.05 keV – 10 MeV, and were normalized to the total photon fluence for comparisons between simulations.

Three field sizes were investigated for static fields: 5cm x 5cm, 10cm x 10cm, and 20 cm x 20 cm. These three field sizes were selected to provide a range of low-energy scattered photons to the dose in the water tank, and to represent the range of field sizes commonly used in radiation therapy. The 20cm x 20cm field (defined by both jaws and MLC) represents a relatively soft spectrum, with a larger contribution of scattered photons from within the water tank. The smaller field size (5cm x 5cm, defined by jaws with the MLC completely retracted) represents a relatively hard spectrum as the head leakage contribution is more pronounced for small fields. The 10cm x 10cm field size was defined using the jaws with the MLC completely retracted to represent the typical reference conditions used for beam calibration and determination of the standard correction factors. For each field size, photon energy spectra were calculated for more than 30 unique positions at various depths along central axis and various depths and distances off axis (up to 50cm from the central axis).

The impact of field modulation through the use of IMRT on the photon spectrum was evaluated by simulating a 10cm x 10cm field as a series of 5 rectangular strips (each strip 2cm x 10cm), giving an IMRT field with a modulation factor of 5. The photon energy spectra were calculated at each of the same positions in the water phantom as for the static fields.

Finally, photon energy spectra were calculated at numerous positions with heterogeneous materials (simulated bone and lung tissue) placed within the simulated water phantom. Simulated bone and lung tissue, density of 1.85g/cm³ and 0.26g/cm³, respectively, were each considered in separate analyses as 9cm of the heterogeneous material replacing the top 9cm of the water phantom. Thus, the SSD was unchanged, and the positions of the tally voxels also remained constant. The photon spectra were calculated in water, below the heterogeneous material.

Impact of Variations in Energy Spectrum on the TLD Response

The energy response of TLD for non-reference measurement conditions has been divided into two components: the component due to the relative probability of photoelectric interactions (K_{PE}) and the component due to solid state effects and all other intrinsic and secondary effects (K_{SE}). The overall energy response for measurement under non-reference conditions (K_{NR}) is the product of these two components, as shown in Equation 3.3.

$$K_{NR}(E) = K_{PE}(E) \times K_{SE}(E) \quad (3.3)$$

Dosimeter response based on Photoelectric Effect

As mentioned previously, LiF has a slightly greater atomic number (Z) than that of tissue, which results in an enhanced probability of photoelectric interactions and energy deposition. This increased probability of photoelectric interactions has the potential of exaggerating the response of the TLD to low-energy x-rays and gamma rays^{2, 7} relative to those that would occur in tissue, resulting in an artificially high reading. To determine the impact of this effect on TLDs, we calculated the energy response correction factor for the photon spectra resulting from each case described in the previous paragraphs.

LiF TLD capsules represent a cavity that can be placed in a medium (water) as a means to measure the absorbed dose. Thus, cavity theory can be used to theoretically determine the energy response correction factor, given the energy spectrum of the photon beam incident on the TLD capsule. Burlin cavity theory in particular is well suited for medium-sized cavities in which the dose arises both from electrons crossing the cavity as well as from secondary electrons that are created inside of the cavity⁷. These conditions are consistent with the interactions in LiF TLD100. The general form of Burlin cavity theory is shown in Equation 3.4⁷.

$$\frac{D_{cav}}{D_{med}} = d \left(\frac{S}{\rho} \right)_{med}^{cav} + (1-d) \left(\frac{\mu_{en}}{\rho} \right)_{med}^{cav} \quad (3.4)$$

In this expression, D_{med} is the dose to the medium (water), D_{cav} is the dose to the cavity (TLD), (S/ρ) is the collisional stopping power, and (μ_{en}/ρ) is the mass energy absorption coefficient. Finally, d is a parameter that describes the average value of the relationship of electron fluence generated in the cavity wall (Φ_w) to the initial equilibrium electron fluence (Φ_w^e)⁷. The extreme values of 1 and 0 for d provide the traditional formalisms for small or large cavity theory⁷. In this work, d was determined as a function of incident photon energy for each discrete energy bin used in the Monte Carlo simulations based on a 2mm diameter TLD capsule.

$$d \equiv \frac{\overline{\Phi}_w}{\Phi_w^e} = \frac{1 - e^{-\beta L}}{\beta L} \quad (3.5)$$

The parameter L is equal to the mean chord length, taken as four times the TLD volume divided by its surface area. The parameter β was determined using Equation 3.6, where t_{max} is the maximum depth of electron penetration, approximated using the continuous slowing down approximation range for the maximum electron energy in each discrete energy bin. In this equation, the value of 0.04 has been previously found to be the most consistent with experimental data⁷.

$$e^{-\beta t_{max}} = 0.04 \quad (3.6)$$

The right side of Equation 3.4 is denoted “MCT” for “medium-sized cavity theory” for the remainder of this work. Thus,

$$MCT = d \left(\frac{S}{\rho} \right)_{med}^{cav} + (1-d) \left(\frac{\mu_{en}}{\rho} \right)_{med}^{cav} \quad (3.7)$$

and the response of the TLD is given by

$$D_{cav} = D_{med} \left[d \left(\frac{S}{\rho} \right)_{med}^{cav} + (1-d) \left(\frac{\mu_{en}}{\rho} \right)_{med}^{cav} \right] = D_{med} MCT_{med}^{cav} \quad (3.8)$$

Absorbed dose can be reasonably approximated by kerma for each of the selected positions in the phantom, given the existence of electronic equilibrium in these locations⁴². The absorbed dose to water was therefore determined using Equation 3.9 where ψE is the energy fluence, which was calculated using the results of the Monte Carlo simulations for each location.

$$D_w = \sum_E \psi_E \left(\frac{\mu_{en}}{\rho} \right)_{water, E} \quad (3.9)$$

The dose to LiF (inside the TLD) can then be determined (Equation 3.10) by the application of Burlin cavity theory, as described in Equation 3.8, and the dose to water, as described in Equation 3.9.

$$D_{LiF} = \sum_E \left(\psi_E \frac{\mu_{en}}{\rho_{water, E}} \times (MCT_{water}^{LiF})_E \right) \quad (3.10)$$

An appropriate energy-response correction factor accounts for the differences in absorbed dose between the point of measurement (at some arbitrary position away from the reference position, or under non-reference conditions) and the point of reference, where the dose calibration has taken place. For dosimetry using TLDs, the point of reference is found at the depth of maximum dose on the central axis for a 10cm x 10cm field size. A dose measured at an arbitrary position would be multiplied by the factor defined in Equation 3.11 to correct for the response of the detector due to variations in the photon energy spectrum at the arbitrary position, such that it is equivalent to the response expected at the reference position

$$K_{PE} = \frac{D_{\text{LiF, reference}}}{D_{\text{LiF, non-reference}}} = \frac{\sum_j \left[\frac{\varphi_j E_j \left(\frac{\mu_{en}}{\rho} \right)_{\text{water},j} \times (MCT_{\text{water}}^{\text{LiF}})_j}{\sum_i \varphi_i E_i \left(\frac{\mu_{en}}{\rho} \right)_{\text{water},i}} \right]_{\text{reference}}}{\sum_j \left[\frac{\varphi_j E_j \left(\frac{\mu_{en}}{\rho} \right)_{\text{water},j} \times (MCT_{\text{water}}^{\text{LiF}})_j}{\sum_i \varphi_i E_i \left(\frac{\mu_{en}}{\rho} \right)_{\text{water},i}} \right]_{\text{non-reference}}} \quad (3.11)$$

Thus, Equation 3.11 is equal to the calculated energy correction factor for non-reference conditions and effectively corrects for the different interaction coefficients arising from differences in the photon energy spectra between the point of measurement and the reference position.

Determination of Secondary Effects on TLD Response

While the above approach accounts for theoretical differences arising from differences in the interaction coefficients, there is also a known solid-state energy response. Solid state effects, such as the charge density effect, are those effects which introduce variation in the energy deposition on the scale of the electron track length. These effects are not predicted by interaction coefficients. To isolate the different components and to determine the total energy correction factor for non-reference conditions, a set of measurements were made with both ion chambers and TLDs. The absorbed dose was measured for several positions corresponding to locations where the photon energy spectra were simulated using the Monte Carlo model. The component of the TLD energy response that is due to the solid-state energy response and other secondary effects that do not include differences in photoelectric interactions is described in Equation 3.12.

$$K_{SE} = \frac{D_{\text{ion chamber}}}{D_{\text{TLD}}} \times \frac{1}{K_{PE}} \quad (3.12)$$

All measurements were performed using a Varian Clinac 21EX accelerator (Varian Medical Systems, Palo Alto, CA) using 6MV photons in a water phantom (Blue Phantom, Scanditronix Wellhofer, Uppsala, Sweden). At each location in the water phantom, dose was measured using both TLDs and a PTW Farmer-type ionization chamber (type 30001, 0.6cm³ volume). Measurement locations included in field and out of field locations for the 10cm x 10cm, 5cm x 5cm, and 20cm x 20cm field sizes. The depth in the water phantom was also varied and dose was measured for depths of 1.6cm, 5cm, and 20cm.

The measured charge at the thirteen selected positions in the water phantom were adjusted according to the protocol outlined in AAPM TG-21⁴⁸ to determine dose at each location based on the photon spectrum at that location (as calculated by the Monte Carlo simulations). For this adjustment, the TG-21 protocol was used. As this protocol extends only to energies as low as 1.25MeV (Co-60), additional consideration was required to extrapolate correction factors to lower energies when needed. The TG-21 protocol was more appropriate for this purpose than the newer TG-51 protocol because cavity theory is explicitly included in this formalism, whereas the TG-51 formalism is simplified by the combining of several factors.

Using the chamber reading, M_{raw} , the dose to the medium (water) was determined using the following expression⁴⁸:

$$D_{med} = \overline{M}_{raw} P_{TP} P_{elec} P_{pol} N_{gas} \left(\frac{L}{\rho} \right)_{gas}^{med} P_{ion} P_{repl} P_{wall} \quad (3.13)$$

Each measurement of charge was corrected for temperature and pressure (P_{TP}), the electrometer factor (P_{elec}), and polarity effects (P_{pol}). The cavity-gas calibration factor (N_{gas}) was determined using the ratio of the chamber's absorbed dose to water calibration factor ($N_{D,w}$, provided by an ADCL) and data in the literature for N_x for the chamber used in this study (PTW 30001)⁴⁹. As this value is considered constant for all photon energies that expend an average of 33.97eV to produce one ion pair (which is the case for photon energies as low as 10keV⁴⁸) it was sufficient for all of the measurements collected in this study, regardless of the non-reference conditions. The ratio of the mean restricted stopping power for the phantom material (water) to the chamber gas (air) was determined as a function of average photon energy at each measurement location using published values⁵⁰. The ion-recombination correction factor (P_{ion}) was directly measured. The replacement correction factor (P_{repl}) is dependent on the photon energy and the radius of the chamber cavity and was estimated using the TG-21 protocol⁴⁸ and data reported by Cunningham and Sontag⁵¹ for each individual measurement position. Extrapolation was necessary for photon spectra with average energy less than 1.25MeV, but uncertainty in the extrapolated values was expected to be small (<1%) based on the minimal dependence on energy. Finally, the P_{wall} factor was determined using the expression in Equation 3.14, where α is the fraction of the total ionization produced by electrons arising in the chamber wall⁴⁸.

$$P_{wall} = \frac{\left[\alpha \left(\frac{\overline{L}}{\rho} \right)_{gas}^{wall} \left(\frac{\mu_{en}}{\rho} \right)_{wall}^{med} + (1 - \alpha) \left(\frac{\overline{L}}{\rho} \right)_{gas}^{med} \right]}{\left(\frac{\overline{L}}{\rho} \right)_{gas}^{med}} \quad (3.14)$$

For photon energies lower than 1.25MeV (⁶⁰Co), Lempert *et al* has shown that α is equal to unity⁵² for our chamber type. Values for the stopping power and mass energy absorption coefficients as a function of photon energy were determined from tabulated data in the literature, and P_{wall} was individually determined for each of the measurement locations.

These measurements were repeated using TLDs in a customized holder that simulated the shape and size of an ion chamber, shown in Figure 3.1. Two TLDs were irradiated for each measurement, and the TLDs were read according to the protocol used by the Radiological Physics Center (RPC, MD Anderson Houston, Texas) and were individually corrected for sensitivity, linearity, and fading, and reference energy⁴¹ as previously described.

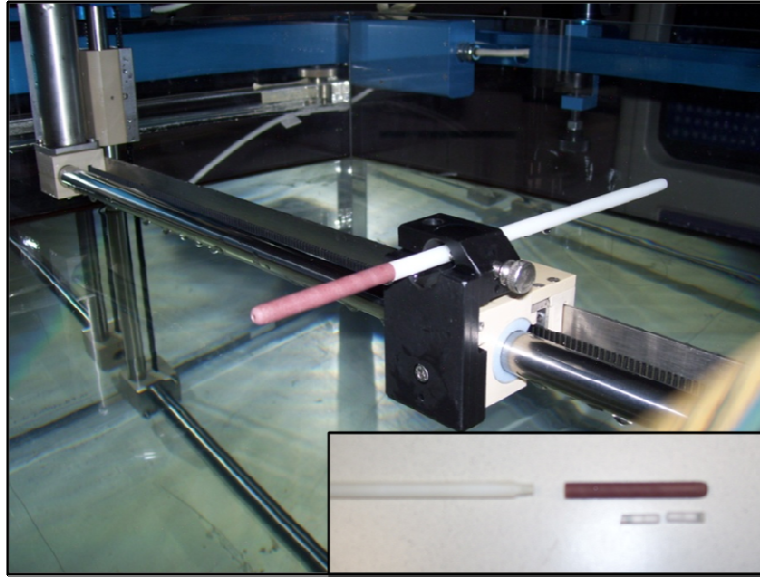


Figure 3.1: Customized TLD holder

3.3 Results

Spectral Variations

Photon energy spectra were calculated using MCNPX. The energy spectra for the most pertinent cases of the variety of sampled locations are shown in Figures 3.2-3.7. The particle flux was tallied for each simulation using a logarithmic energy binning structure from 1keV to 10MeV. The top energy bin collected particles in the energy range of 7.36MeV to 10MeV, and therefore has a value of zero for all 6MV simulations. All curves were normalized to have the same area, and error bars are included based on the 1-sigma statistical uncertainty in the MCNPX simulations.

Variations in in-field photon spectra

The variation in photon energy spectra for a 6MV therapeutic beam along the central axis at depths of 0.1mm, 1.6cm (reference spectrum), 10cm, and 25cm for the 10cm x 10cm field size is shown in Figure 3.2. The spectra show some minor variation with depth; however they appear to be qualitatively similar, peaking at approximately the same energy.

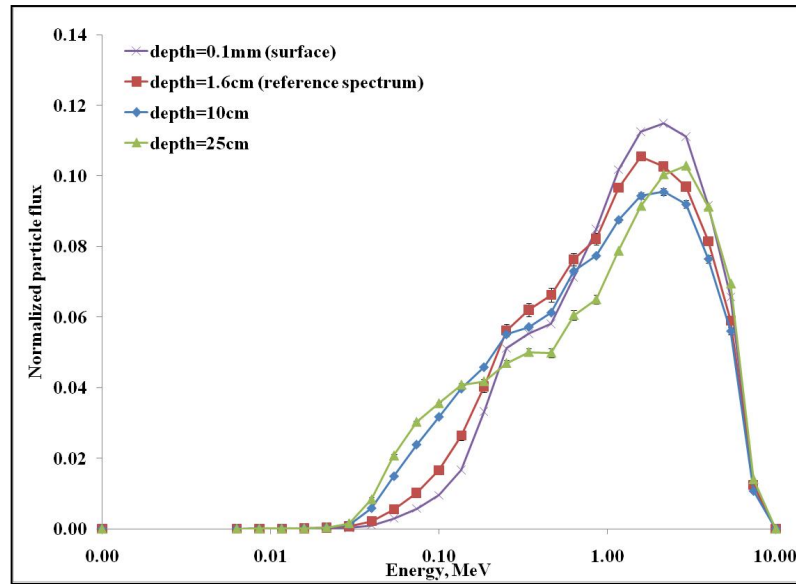


Figure 3.2: Variations in photon energy spectra as a function of depth along central axis for a 6 MV 10cm x 10cm field.

The variations in photon energy spectra for three field sizes (5cm x 5cm, 10cm x 10cm and 20cm x 20cm) are compared in Figure 3.3 at a depth of 10cm on the central axis in water. As expected, the 5cm x 5cm field resulted in a slightly harder spectrum relative to the spectrum from the 10cm x 10cm field while the 20cm x 20cm field (designed to maximize scatter) resulted in a softer spectrum relative to the spectrum from the 10cm x 10cm field.

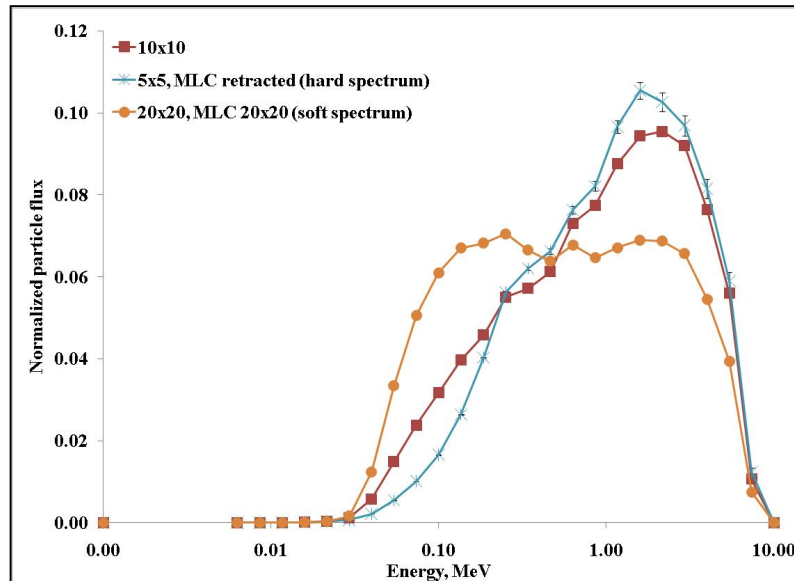


Figure 3.3: Photon energy spectra at depth of 10 cm in water along central axis for three field sizes.

Variations in out-of-field photon spectra

The photon energy spectra were determined for each of the three field sizes at several distances from the central axis for three different depths in water: 1.6cm, 5cm, and 20cm. As the distance away from the central axis increased, the photon energy spectra became progressively softer. In general, the photon spectrum out-of-field would be composed of a

dominant low-energy component due to patient scatter and a high-energy component due to head leakage. While the spectra changed minimally with off-axis distance within the treatment field, the low-energy scatter component became more pronounced at increasing distances outside of the treatment field. Furthermore, for out-of-field locations, changes in depth induced a more pronounced difference in the spectra than increased distance off-axis. This is depicted in Figures 3.4 and 3.5: in Figure 3.4 as a function of distance from the central axis for a 10cm x 10cm field size and in Figure 3.5 as a function of field size for an out of field measurement location. For contrast, the photon energy spectrum at d_{max} on the central axis is also included.

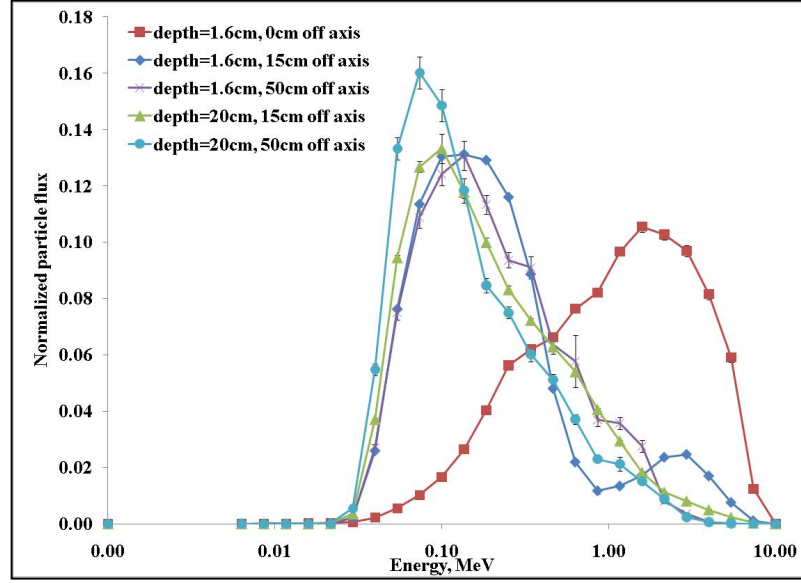


Figure 3.4: Variations in out-of-field photon energy spectra as a function of distance from the central axis for 10cm x 10cm field.

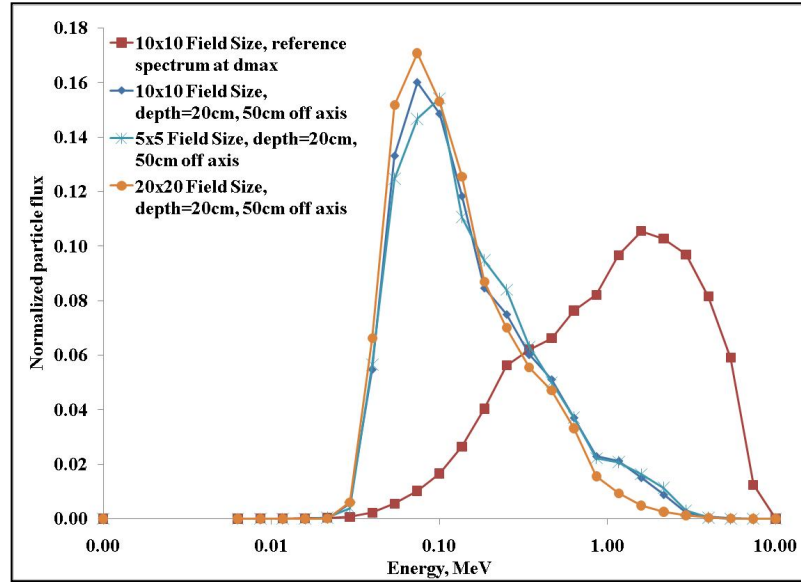


Figure 3.5: Variations in out-of-field photon energy spectra for three different field sizes.

Variations in spectra for IMRT field

A single IMRT field was simulated and the resulting photon energy spectra were calculated at several locations with varying depth and distance from central axis. Two of these spectra are shown in Figure 3.6 along with the spectra for the corresponding locations for a 10cm x 10cm open field. At a depth of d_{max} on central axis, the IMRT photon energy spectrum was harder than the open 10cm x 10cm field energy distribution. This trend is less pronounced for out of field positions, where the spectra are very similar. The energy spectra for the IMRT field and the 10cm x 10cm open field at a distance 10 cm from central axis were nearly identical. The out of field spectra show contributions from low-energy phantom scatter and relatively high-energy head leakage, consistent with other out-of-field spectra.

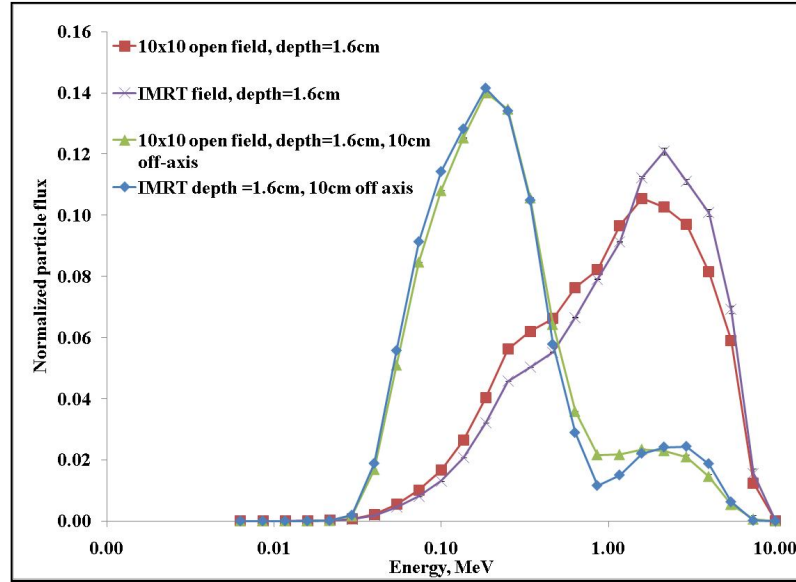


Figure 3.6: Variation in photon energy spectra for both an in-field and out-of-field measurement location for an IMRT field compared to 10x10 open field.

Variations in spectra in presence of heterogeneities

The results for the simulations which included two common heterogeneous materials (bone and lung) are shown in Figure 3.7 for a 10cm x 10cm field at varying depths in water. The reference spectrum in homogeneous media (water) is also plotted in Figure 3.7 for comparison. There is little difference in the spectra below the heterogeneous materials compared to the reference spectrum in homogeneous material, illustrating that the composition of the tissue has a minimal impact on the photon energy spectra. These results are consistent with the out of field spectra; the presence of a heterogeneous material does not further perturb the photon spectra for out of field measurement locations. For a 6MV photon beam, beam hardening is relatively minimal, even for a large amount of bone tissue. Furthermore, the energy spectrum through 9cm of lung material has been shown to not be substantially different from the photon energy spectrum in water.

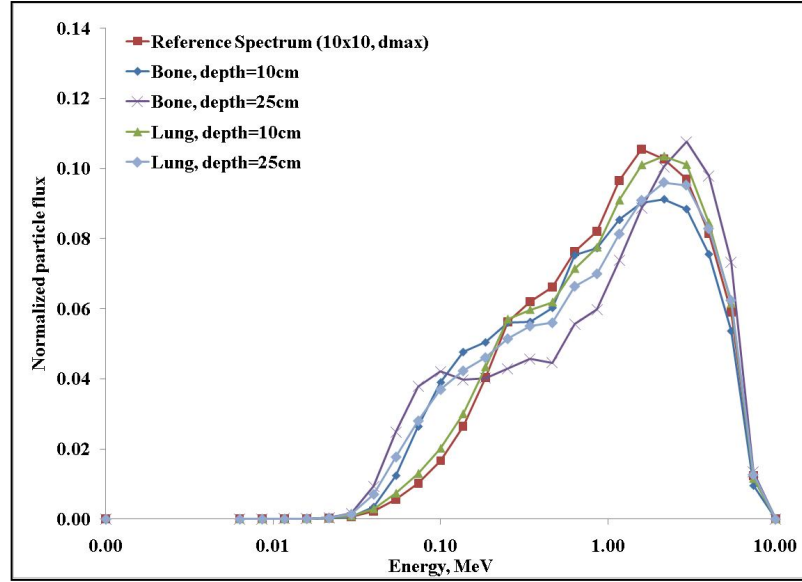


Figure 3.7: Variation in photon energy spectra with depth along central axis due to presence of bone tissue and lung tissue.

Impact of Spectral Variations on Energy Response according to Cavity Theory

The non-reference condition energy correction factor based on the impact of the interaction coefficients (K_{PE}) was calculated as described above using Burlin cavity theory for each calculated photon energy spectra. The parameter d was calculated as a function of incident photon energy and is shown in Figure 3.8. Using tabulated stopping power data, the calculated parameter d , and the simulated photon energy spectra for each of the various tally positions, K_{PE} was determined for the different measurement positions and treatment parameters.

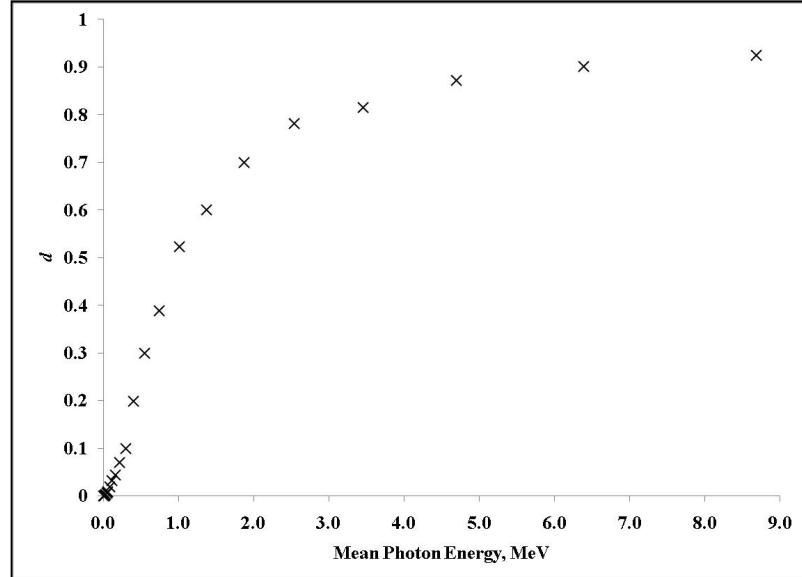


Figure 3.8: Variation of parameter d as a function of incident photon energy (mean bin energy, MeV)

Table 3.1 summarizes the mean photon energy and the calculated values of K_{PE} for selected in-field positions with varying treatment parameters, including the addition of tissue heterogeneities and field modulation. The positions described in the table were all measured along the central axis and, for heterogeneous cases, beneath the heterogeneous material. The energy correction factor, K_{PE} , varied by less than 1% over the range of irradiation conditions and energy spectra investigated in this study.

Table 3.1: Calculated KPE for in-field spectral variations (Monte Carlo) due to field size and depth

Condition, Field Size	Depth (cm)	Mean Photon Energy (MeV)	Energy Correction Factor (K_{PE})
Reference position: 10cm x 10cm	1.6	1.49	1.00
Reference field size, depth			
10cm x 10cm	5	1.41	0.99
10cm x 10cm	10	1.39	0.99
10cm x 10cm	25	1.53	1.00
In field, hard spectrum: 5cm x 5cm	10	1.70	1.01
In field, soft spectrum: 20cm x 20cm	10	1.06	0.99
Bone heterogeneity, 10cm x 10cm	10	1.35	0.99
Lung heterogeneity, 10cm x 10cm	10	1.50	0.99
IMRT Field	1.6	1.68	1.00
IMRT Field	5	1.54	1.00

Relative to the reference position there was little variation in the cavity-theory-based response of the TLD resulting from differences in the photon energy spectra, despite the visible variations in the photon energy spectra (e.g., Figure 3.7). At these locations, and all other in-field locations, the data showed similar results; the TLD response to the non-reference spectra was less than 1% different from that of the reference spectra as a result of differences in interaction coefficients.

The energy response of the TLD showed more variation for out-of-field measurement locations than for in-field measurement locations. The mean energy was substantially lower at these locations – in some cases less than a fifth of the mean energy at the reference position. The lower energy is associated with increased photoelectric interactions in the TLD at these positions, and, as a result, increased discrepancy between the dose measured by the TLD and the dose actually absorbed by the tissue. Table 3.2 summarizes the non-reference energy correction factor based on interaction coefficients (K_{PE}) for measurement positions that were made outside of the treatment field for varying treatment parameters. As can be seen in the table, the TLD may over-respond by as much as 7% based on cavity theory (corresponding to a K_{PE} of 0.93). These data displayed the greatest degree of variation both in the photon energy spectra and K_{PE} .

Table 3.2: Calculated KPE for spectral variations (determined via Monte Carlo) occurring at out-of-field locations

Condition, Field Size	Depth (cm)	Distance Off-Axis (cm)	Mean Photon Energy (MeV)	Energy Correction Factor (K_{PE})
Reference position, 10cm x 10cm	1.6	0	1.49	1.00
Near treatment field, 10cm x 10cm	5	15	0.31	0.96
Far from treatment field, 10cm x 10cm	20	50	0.22	0.94
Bone heterogeneity, 10cm x 10cm	20	50	0.22	0.94
Lung heterogeneity, 10cm x 10cm	20	50	0.24	0.95
Out of field, hard spectrum: 5cm x 5cm	20	50	0.23	0.95
Out of field, soft spectrum: 20cm x 20cm	20	50	0.17	0.93
IMRT Field	1.6	10	0.41	0.98
IMRT Field	5	15	0.34	0.97

The non-reference energy response correction factor based on cavity theory (K_{PE}) is shown in Figure 3.9 as a function of mean photon energy. This figure includes the three field sizes examined as well as the energy correction factors determined when heterogeneous materials were added to the phantom. The response follows the mean photon energy, with larger correction factors required as the photon energy decreases.

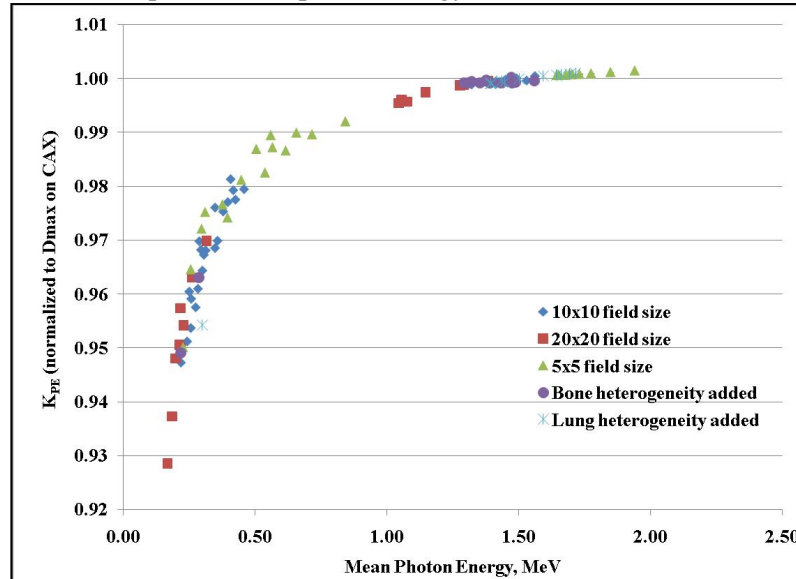


Figure 3.9: K_{PE} for various field sizes in water and presence of heterogeneities, as a function of mean photon energy.

Determination of Total Energy Correction Factor

To determine the total energy correction factor, including both interaction coefficient-based effects (cavity theory) (K_{PE}) and solid state and other secondary effects (K_{SE}), a series of measurements were performed using TLDs and an ionization chamber. A measured energy correction factor was determined using the ratio of the fully corrected ion chamber measured dose to the TLD measured dose. This measured correction factor for non-reference

measurement conditions (K_{NR} , defined previously in Equation 3.3) includes components of the difference in photoelectric interaction probability as well as all other secondary effects, and it is provided in Table 3.3 for several selected measurement locations with varying spectra. The value of K_{NR} for the reference position (10cm x 10cm, depth of 1.6cm, along central axis) is 1.00 by definition.

The results of our data showed that for mean photon energies of 500keV and greater, K_{SE} was nearly unity, and so for all in-field locations the non-reference energy correction factor (K_{NR}) was virtually unity. For those measurement positions where the photon energy spectra were lower in energy (out-of-field locations), the values of K_{SE} deviated from unity. For energy spectra with a mean energy of less than 500 keV, measured data showed that the TLDs over-responded by an average of 3.5% more than that predicted by the theoretical calculations using cavity theory. A graphical representation of the agreement between K_{NR} and K_{PE} is provided in Figure 3.10. This additional over-response is not due to the increased photoelectric effect due to higher atomic number, but rather due to solid-state effects such as charge density effects or other secondary effects.

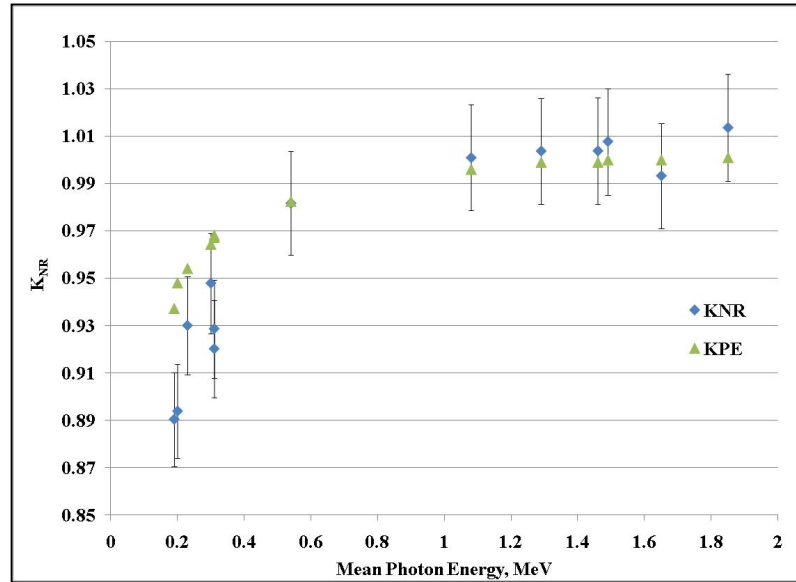


Figure 3.10: Comparison of theoretical energy response (K_{PE}) and total measured response

In general, about one third of the energy response was due to solid state-effects, while two thirds of the energy response was due to differences in interaction coefficients as described by cavity theory. Overall, the total energy correction is unity within the treatment field, but increased to approximately 12% for the softest spectra outside of the treatment field. The total uncertainty in the ion chamber measurements of absorbed dose, based on the uncertainty in each correction factor is estimated to be less than 2%. The total uncertainty in the TLD measurements based on the RPC TLD protocol is estimated to be less than 3%.

3.4 Discussion

Variations in the photon energy spectra as a function of field size, depth in water, the presence of heterogeneity, field modulation, and measurement location were quantified for 6MV photon fields. The impact of these variations on dose measurement using a common energy-dependent dosimeter (TLD) was determined based on cavity theory, and were also measured to account for solid state effects.

The non-reference energy correction factor was determined for several measurement positions with varying treatment parameters, representing a clinically useful range of field sizes and treatment techniques including conventional RT and IMRT. This factor, K_{NR} , varied from 0.88 to 1.01 among the situations examined as part of this work. Within the treatment field, over all field sizes and depths examined, the response of the TLD varied by less than 1% relative to the reference point (d_{max} on the central axis from a 10cm x 10cm field) because of variations in the photon energy spectrum. The presence of heterogeneities in the field did not greatly impact the photon energy distribution along the central axis, nor did field modulation, and corrections to the measured dose would be less than 1% for these situations. It may be possible that more highly-modulated IMRT fields could induce a notable energy-response by the TLD, and further analysis of more complex IMRT plans and field arrangements could be performed to further explore these initial findings. However, based on the extensive range of conditions explored in this work, in-field dose measurement from 6MV photon fields using TLD do not require an additional non-reference energy correction factor.

Calculated dose to water has been approximated with kerma, which is a valid assumption under conditions of electronic equilibrium; however this condition is not met at the surface of the phantom or in the field penumbra. This may be a relevant concern as TLD are often placed on the patient surface as a method of estimating dose to the patient. Our methodology may have increased uncertainty in these situations. Simulations performed at the surface of the phantom for a 10cm x 10cm field size along central axis show that there is little variation in the photon energy spectrum from the spectrum at the reference position (shown in Figure 3.2). Furthermore, there is little variation in the value of the ratio of stopping powers (S/ρ) between water and LiF over the relevant energy range. These two relationships indicate that neither photons nor electrons should affect the response of the dosimeter at the surface relative to the response at d_{max} . Therefore, despite the increased uncertainty in the surface location, we believe K_{NR} to be nearly identical to the value at d_{max} . For surface measurements made out of field, a bath of contaminating electrons results in an elevated dose at the surface relative to the dose at depth, potentially by up to a factor of six⁴². Without adequate buildup material, dose to the TLD is not likely to be representative of dose to the patient. For these locations, the TLD should be covered with buildup material (such as bolus), to bring the TLD to an effective depth of d_{max} . Measurements conducted at depth of d_{max} for locations outside of the treatment field would then use the appropriate non-reference energy correction factor as described in Table 3.3.

Table 3.3: Total Energy Correction Factor (KNR) for selected locations with varying mean photon energy

Field Size (cm x cm)	Depth (cm)	Distance Off-Axis (cm)	Mean Photon Energy (MeV)	K_{PE}	K_{SE}	Total Energy Correction Factor (K_{NR})
20cm x 20cm	20	30	0.19	0.94	0.95	0.89
20cm x 20cm	5	20	0.20	0.95	0.94	0.89
20cm x 20cm	20	20	0.23	0.95	0.97	0.93
10cm x 10cm	5	30	0.30	0.96	0.98	0.95
10cm x 10cm	5	15	0.31	0.96	0.97	0.93
10cm x 10cm	20	15	0.31	0.97	0.95	0.92
5cm x 5cm	5	15	0.54	0.98	1.00	0.98
20cm x 20cm	25	0	1.08	1.00	1.00	1.00
20cm x 20cm	1.6	0	1.29	1.00	1.00	1.00
10cm x 10cm	20	0	1.46	1.00	1.00	1.00
5cm x 5cm	1.6	0	1.65	1.00	0.99	0.99
5cm x 5cm	20	0	1.85	1.00	1.01	1.01

For locations outside of the treatment field, energy correction factors varied more extensively. The results showed that TLD over-responded by up to 12% when used to measure dose outside of the treatment field relative to within the treatment field. The majority of this over-response was due to the atomic number of TLD altering the photon and electron interaction coefficients relative to water. The magnitude of this energy response may be relevant to TLD-based measurements of out-of-field dose.

Due to the theoretical basis and assumptions used to derive the cavity theory (Equation 3.10), it is necessary to test the validity of the results obtained with its use. This was done by determining K_{PE} for monoenergetic photons following the procedure outlined above and normalized relative to ^{60}Co . The calculated energy correction factors were then compared with those in the literature, which had been determined either through measurement or Monte Carlo for monoenergetic photon beams⁵³⁻⁵⁵. This comparison is shown in Figure 3.11 and shows very good agreement, indicating that the theoretical approach we have taken is sound. The only discrepancy is at very low energies (below those energies relevant to this study), where self-attenuation of the TLD is known to reduce its sensitivity.

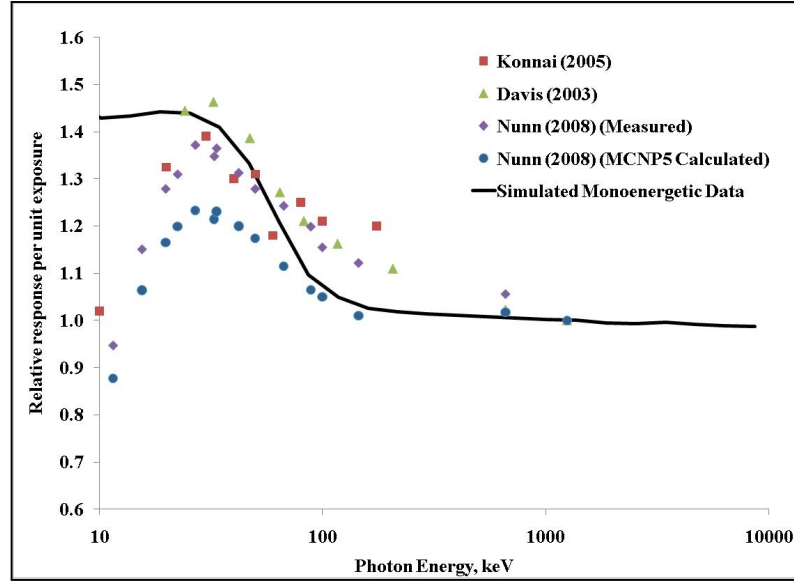


Figure 3.11: Literature comparison of TLD response to photon energy spectra

The second component (K_{SE}) due to secondary effects, which is not predicted by cavity theory, was demonstrated in the measured data to be relevant at photon energies less than 500keV. According to the data, the magnitude of this additional over-response can range between 2% and 5% with an average value of 3.5% for photon energies between 10keV and 500keV. The magnitude of this effect is comparable to that described in the literature, which has suggested an over-response of less than 10% at comparable or even lower photon energies⁵⁶.

This study has resolved the total energy response factor (K_{NR}) into its two components; the first of which has been calculated using fundamental cavity theory, and the second was examined through the measured data. The total energy response correction factor (K_{NR}) that was determined in this study accounts for deviations in the photon energy spectra from the reference point of calibration for measurement locations that do not coincide with the point of calibration. This factor does not replace the TLD energy correction factor discussed in the introduction but rather should be applied multiplicatively to it depending on the measurement conditions. A revised expression for determining absorbed dose from TLD measurements is provided in Equation 3.15, where K_{NR} is the energy correction factor dependent on the measurement conditions and location.

$$D = T \times S \times K_L \times K_F \times K_E \times K_{NR} \quad (3.15)$$

This energy response correction factor will correct for variations in the photon energy spectra when measurements are taken under non-calibration conditions, such as out-of-field measurements.

3.5 Conclusion

Currently, TLD are used to measure or verify the absorbed dose for many applications in therapeutic physics, including measurement of numerous points within a wide range of treatment fields as well as outside of the treatment field. The energy correction factor determined in this work should be applied multiplicatively to thermoluminescent signal to account for varying detector responses with different photon spectra. In general, it is

acceptable to ignore variations in the photon spectrum within the treatment field because there is a negligible impact on the measured dose. However, outside the treatment field, the spectra are much softer, and a correction factor is generally appropriate. The value of this factor has been shown to range from 0.88 to 0.99 depending on the specific irradiation conditions.

Chapter 4: Characterization of energy response of $\text{Al}_2\text{O}_3\text{:C}$ optically stimulated luminescent dosimeters (OSLD) using cavity theory

Chapter 4 was accepted for publication in the journal of Radiation Protection Dosimetry in May 2012. [doi: 10.1093/rpd/ncs086] Written permission has been obtained from the journal for use of these materials in this dissertation.

4.1 Introduction

Optically stimulated luminescent dosimeters (OSLDs) have historically been used as personal dosimeters; however, these dosimeters have recently gained popularity in medical applications for monitoring and tracking patient dose. OSLDs are well suited to dose measurements in medical settings owing to their small size, high sensitivity, and ease of readability⁵⁷⁻⁶¹.

A common material for OSLDs is carbon-doped aluminum oxide ($\text{Al}_2\text{O}_3\text{:C}$). This crystal possesses inherent properties of both thermoluminescence and optically stimulated luminescence – that is, both heat and light can be used to release electrons “trapped” in energy states between the conduction band and valence band⁶¹. However, the use of optical stimulation allows the dosimeters to be read at room temperature without the practical and technical difficulties associated with heating⁶¹. Also, dose information in $\text{Al}_2\text{O}_3\text{:C}$ is not lost after the initial read; OSLDs can be read multiple times with minimal signal loss. These advantages, as well as the relatively low cost of OSLDs make this type of dosimeter an attractive option for many applications.

To achieve accurate dosimetry, an energy correction specific to the irradiation energy is generally necessary. The energy correction factor depends on the irradiation photon energy spectrum and is derived from the relative response of the dosimeter to a standard photon source. This correction is often assumed to be constant for the nominal irradiation energy, despite evidence that this may introduce additional uncertainties⁶². While the correction factor can be directly measured or calculated with Monte Carlo simulations, these approaches can be challenging and time consuming. In principle, correction factors can also be calculated with cavity theory, which has been used in the literature to determine the energy dependence of other solid state detectors⁶²⁻⁶⁷. Burlin cavity theory is most appropriate for “medium-sized” cavities, where the total dose is due to contributions from both photon and electron interactions inside the cavity^{7; 64}. Cavities of varying physical size can thereby be well approximated using this theory. This calculation-based approach may provide a useful alternative method for determining energy correction factors without requiring detailed measurements or simulations.

Recent studies in the literature have evaluated the energy dependence of $\text{Al}_2\text{O}_3\text{:C}$ for discrete photon energies and beams^{58; 60; 68-70}. Also, the response of $\text{Al}_2\text{O}_3\text{:C}$ as a thermoluminescent dosimeter has been evaluated for a range of photon energies^{71; 72}. To our knowledge, the response of $\text{Al}_2\text{O}_3\text{:C}$ as a continuous function of photon energy has not previously been described using cavity theory. The objective of this work, therefore, was to establish an expression for the energy response of $\text{Al}_2\text{O}_3\text{:C}$ OSLD using Burlin cavity theory, which could be applied to any arbitrary photon spectrum. The energy response determined via cavity theory was evaluated through a comparison to measured values for a range of irradiation conditions using a typical medical radiotherapy photon beam. Furthermore, we

completed a comparison to measured values reported in the literature for a range of common polyenergetic beams.

4.2 Materials and Methods

The OSLDs evaluated in this study are Landauer nanoDots (Landauer, Inc., Glenwood, IL), which are thin discs of diameter 4 mm and thickness 0.3 mm. The sensitive material is housed in a light-tight and tissue-equivalent plastic casing. The thickness of the casing is small (<1 mm) on both sides of the disc and was not considered in the energy response calculations because the composition is very close to that of the surrounding medium (water). These dots are commercially available and are currently the standard dosimeter for the remote dosimetry program of the Radiological Physics Center (RPC, MD Anderson Cancer Center, Houston, TX). The dosimeters were read using an InLight Microstar OSL reader (Landauer, Inc., Glenwood, IL) which was operated in continuous wave mode for a 7 second read time.

Calculation of dose to OSLDs using Burlin cavity theory

The OSLDs represent a cavity placed in a medium (water) as a means of measurement of absorbed dose. Thus, cavity theory can be used to theoretically determine the energy dependence of the dosimeter, given the energy spectra of the photon beam incident on the OSLD. Cavity theory depends on the geometry of the cavity, particularly the mean path length through the cavity. The nanoDots used in this study are not spherical (as most readily described by cavity theory) but are instead a thin disk. Therefore, the cavity volume was approximated in three different ways to determine the dependence of the cavity theory on the consideration of the size and geometry of the detector. The first approach (Model 1) estimated the OSLD disc as a sphere with a diameter equal to the thickness of the disc (0.3 mm); the second approach (Model 2) estimated a sphere with a volume equivalent to that of the disc; the third approach (Model 3) estimated a sphere with a radius equal to the radius of the disc (2 mm). The radius, volume, and mean chord length of each model of approximation are provided in Table 4.1.

Table 4.1: Dimensions of the three models for approximating OSLD cavity size and geometry

	Model 1	Model 2	Model 3
Sphere Radius	0.015 cm	0.097 cm	0.2 cm
Sphere Volume	$1.41 \times 10^{-5} \text{ cm}^3$	0.0038 cm^3	0.034 cm^3
Mean Chord Length	0.02 cm	0.13 cm	0.27 cm

Burlin cavity theory consists of two components to account for both the dose that arises from secondary electrons crossing the cavity, as well as dose from secondary electrons that are created inside of the cavity. Although many modifications of Burlin theory have been proposed, Miljanic and Ranogajec-Komor found that the most general expression of Burlin cavity theory gives good agreement with experimental results⁶⁴; therefore, the general Burlin cavity theory (shown in Equation 4.1)^{7; 64} was used to calculate the dose to the OSLD:

$$\frac{D_{cav}}{D_{med}} = d \frac{\left(\frac{\bar{S}}{\rho} \right)_{cav}}{\left(\frac{\bar{S}}{\rho} \right)_{med}} + (1-d) \frac{\left(\frac{\mu_{en}}{\rho} \right)_{cav}}{\left(\frac{\mu_{en}}{\rho} \right)_{med}} \quad (4.1)$$

In this expression, D_{med} is the dose to the medium (water), D_{cav} is the dose to the cavity (OSLD), and the ratio of these two parameters describes the response of the OSLD relative to water. Also in Equation 4.1, (\bar{S}/ρ) and (μ_{en}/ρ) denote the ratios of the average mass stopping power and mass energy absorption coefficient (for the cavity and medium, respectively). The average mass stopping power included in this expression is the average stopping power for the spectrum of electrons generated from a monoenergetic photon. For $Al_2O_3:C$, the mass stopping power values were determined based on the weight fraction of the mass stopping powers of aluminum and oxygen. The fraction of carbon was not included in the stopping power determination on account of previous work by Mobit et al, which showed that the energy response of pure Al_2O_3 was not different from that of 1% carbon-doped Al_2O_3 ⁷³. Stopping power data was taken from Johns and Cunningham for each material ⁵⁰, and the mass energy absorption coefficient and range data was collected from data tables maintained by the National Institute of Standards and Technology (NIST) ^{74; 75}.

The parameter d in Equation 4.1 describes the average value of the relationship of electron fluence generated in the cavity wall to the initial equilibrium electron fluence, and its value depends on the size of the cavity as well as the energy of the incident photon spectra. The extreme values of 1 and 0 provide the traditional formalisms for small or large cavity theory ⁷. The parameter d was determined as a function of the incident photon energy for each dosimeter model (Table 4.1) using the expression below.

$$d \equiv \frac{\bar{\Phi}_w}{\Phi_w^e} = \frac{1 - e^{-\beta L}}{\beta L} \quad (4.2)$$

The parameter L is equal to the mean chord length, taken as four times the cavity volume divided by its surface area (Table 4.1). The parameter β , which describes the buildup and build-down of the electron fluence as a function of distance into the cavity, was determined using Equation 4.3, where t_{max} is the maximum depth of electron penetration, approximated using the continuous slowing down approximation range for the maximum electron energy in each discrete energy bin ⁷. A value of 0.04 was recommended by Janssens et al based on his model ⁷⁶ because it was found to be most consistent with experimental data at energies similar to those in the current study.

$$e^{-\beta t_{max}} = 0.04 \quad (4.3)$$

The dose to the OSLD (D_{cav}) can therefore be calculated as shown in Equation. 4.4.

$$D_{Al_2O_3:C} = D_{water} \times \left[d \frac{\left(\frac{\bar{S}}{\rho} \right)_{Al_2O_3:C}}{\left(\frac{\bar{S}}{\rho} \right)_{water}} + (1-d) \frac{\left(\frac{\mu_{en}}{\rho} \right)_{Al_2O_3:C}}{\left(\frac{\mu_{en}}{\rho} \right)_{water}} \right] \quad (4.4)$$

Determination of the energy response

At lower energies, $Al_2O_3:C$ will experience a greater number of photoelectric interactions than tissue, as described by differences in the mass-energy absorption coefficients of the two materials. There are also differences in stopping power that will impact the relative energy response of OSLD under conditions where secondary electron equilibrium does not exist.

The response of the OSLD (versus water) as a function of photon energy was determined as shown in Equation 4.5 for a comprehensive range of photon energies. Each of the components in Equation 4.5 is a function of photon energy, and the energy response depends only on d and tabulated data.

$$\begin{aligned}
 R_{Al_2O_3:C:Water}(E) &= \frac{D_{Al_2O_3:C}(E)}{D_{water}(E)} \\
 &= d(E) * \frac{\left(\frac{\bar{S}}{\rho}\right)_{Al_2O_3:C}(E)}{\left(\frac{\bar{S}}{\rho}\right)_{water}(E)} + (1 - d(E)) \frac{\left(\frac{\mu_{en}}{\rho}\right)_{Al_2O_3:C}(E)}{\left(\frac{\mu_{en}}{\rho}\right)_{water}(E)} \quad (4.5)
 \end{aligned}$$

Furthermore, the dependence of the energy response on the full photon energy spectrum was investigated. The response was determined for three arbitrary photon energy spectra using the complete spectral information, as well as using only the mean photon energy. The three investigated spectra include one that is relatively soft (low energy), one medium, and one relatively hard (higher energy). These three spectra were previously determined from simulations of spectra occurring in and around the primary photon beam from a Varian medical linear accelerator^{42; 43; 62}. For each of the three spectra, the absorbed dose to water was estimated as collision kerma in the medium (water) using the complete spectrum as shown in Equation 4.6.

$$D_w = \sum_E \Psi_E \left(\frac{\mu_{en}}{\rho} \right)_{water, E} \quad (4.6)$$

The water collision kerma is a good approximation for the quantity absorbed dose to water (Equation 4.6) when secondary electron equilibrium is present, as is the case for the specific condition used here: a water cavity contained in a water medium beyond the buildup region at the water surface.

In practice, it is necessary to identify the difference in dosimeter response for different photon spectra such that appropriate corrections can be made. Generally, standard dosimeters are irradiated using some reference energy (often ⁶⁰Co), but experimental measurements are made using some other photon energy. The difference in response between the experimental energy and the reference energy is defined here as the relative response (RR) (Equation 4.7). The dosimeter response could then be corrected by multiplying the measured dose by the inverse of the RR .

$$RR = \frac{R_{Al_2O_3:C:water} \Big|_{experimental}}{R_{Al_2O_3:C:water} \Big|_{reference}} \quad (4.7)$$

4.3 Results

Use of cavity theory to determine energy response

The response of aluminum oxide OSLDs was calculated using Burlin cavity theory for three cavity models (Table 4.1) that differed by the parameter d (Equation 4.2). Figure 4.1 shows the variation in d as a function of photon energy for the three models considered. Values of d close to unity imply a small cavity with dose deposition dominated by electrons crossing the cavity, while values close to 0 imply a large cavity where the dose is dominated by electrons generated from photon interactions within the cavity. The larger cavity model of the OSLD (Model 3) is associated with much smaller values of d , indicating a greater dominance of photon interactions to the dose. However, regardless of model, at low photon energies the deposited dose was dominated by electrons produced in the cavity (i.e., photon interactions) and dose therefore depends on the mass energy absorption coefficient.

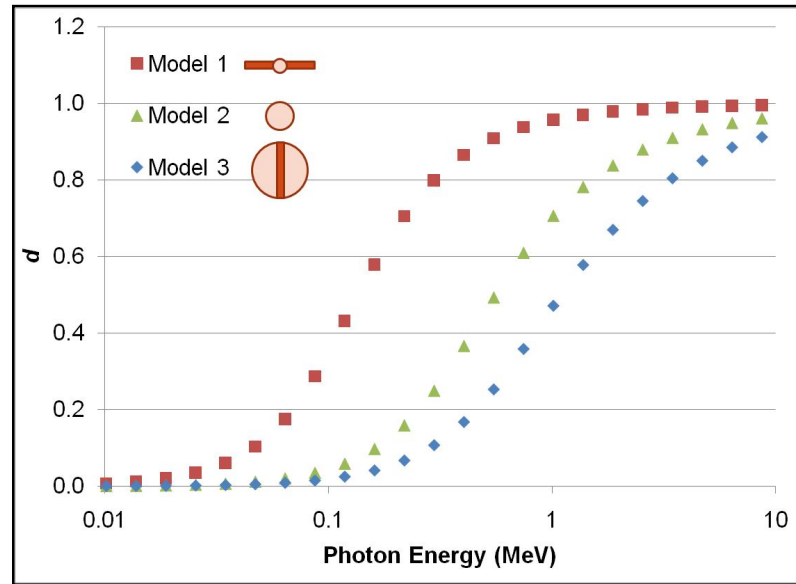


Figure 4.1: Variation of d as a function of photon energy for three approximations of the OSLD cavity size.

The energy response of OSLD was calculated as a function of photon energy for each of the OSLD cavity models. Despite the large difference in d as a function of the cavity size, there was little variation in the energy response. The response of $\text{Al}_2\text{O}_3\text{:C}$ in terms of the ratio of absorbed dose to the dosimeter versus absorbed dose to water as a function of photon energy is shown in Figure 4.2 for each of the three size models. At most, the three different models resulted in a difference in energy response of 12%, occurring for monoenergetic photon energies near 100 keV.

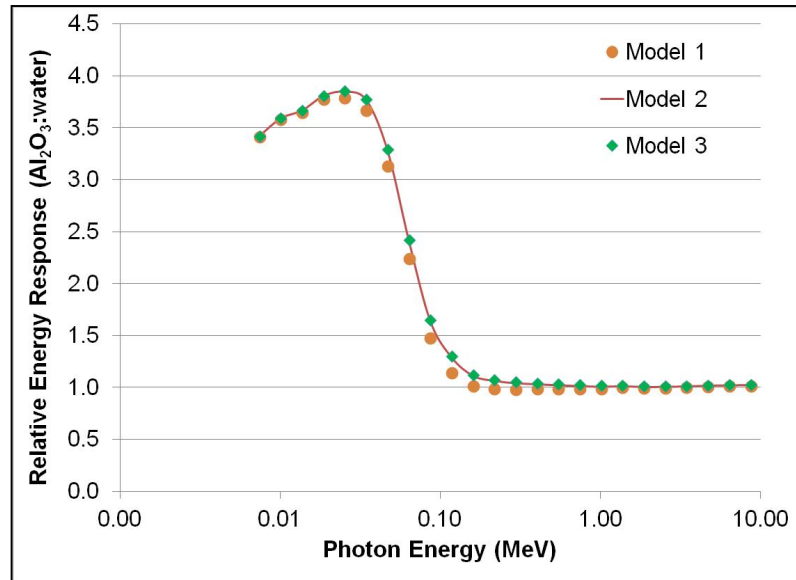


Figure 4.2: Relationship between dose to cavity and dose to medium calculated using Burlin cavity theory for several different sized cavities.

While the energy dependence of OSLD is close to unity for energies above 100 keV, the OSLD overresponds dramatically relative to water at energies below this. The response reaches a maximum in excess of a factor of 3.5 at energies around 20 keV. Model 2 (solid line) approximates the OSLD disc as a sphere of equivalent volume and was used for all remaining calculations.

Dependence of energy response on photon spectra

The relative response (RR) was determined for three photon spectra taken from Scarboro et al (2011). These three spectra have very similar mean photon energies but vary in the distribution of photon energies (Figure 4.3).

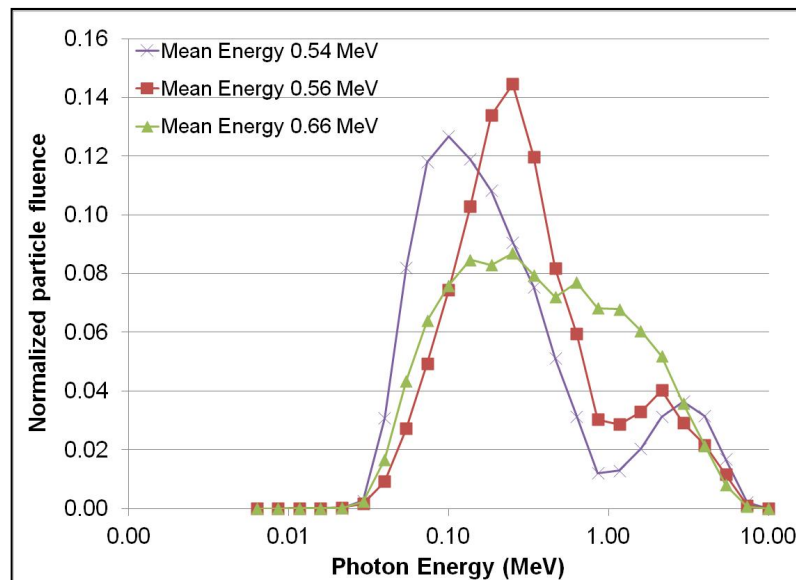


Figure 4.3: Three unique photon energy spectra with similar mean energies.

The impact of the photon spectra on the OSLD response was evaluated by comparing the relative response determined using the full photon spectra (Figure 4.3) versus that determined using only the mean photon energy. The mean photon energy was calculated using photon fluence. The relative response (Table 4.2) was the ratio of the absorbed dose to the OSLD material versus the absorbed dose to water of the arbitrary spectrum relative to a pure ^{60}Co photon source ($E = 1.25 \text{ MeV}$). When the relative response was calculated using the mean energy of the spectra, almost identical responses were found that were very close to unity. In contrast, when the spectra were considered, the relative response varied, and was up to 10% different than the relative response predicted with mean energy alone. Spectral information is more important for beams with a large component of photons with energies below 100 keV, such as those found in diagnostic imaging photon beams. However, this analysis indicates that full spectral consideration may be necessary to achieve accurate dosimetry OSLD, even at relatively high energies.

Table 4.2: Relative response (RR) (using a ^{60}Co source ($E = 1.25 \text{ MeV}$) as the standard energy) for three unique spectra calculated using both mean photon energy and full spectral information.

	Soft Spectrum	Medium Spectrum	Hard Spectrum
Mean Photon Energy (MeV)	0.54	0.56	0.66
$\text{RR}_{(\text{Al2O3:C to water})}$ (using complete spectra)	1.12	1.06	1.06
$\text{RR}_{(\text{Al2O3:C to water})}$ (using mean energy)	1.02	1.01	1.01

Comparison of calculated and measured energy response

Because of the theoretical basis of the energy response calculated in this work, it is appropriate to compare the results calculated using cavity theory with measured energy response factors. The calculated energy response was compared to the measured energy response for a subset of irradiation conditions in water from a typical medical radiotherapy photon beam. Radiation field size, depth in water, and distance from central axis were varied to create five unique irradiation conditions, and the photon spectra at these locations were previously simulated using a benchmarked Monte Carlo model of a Varian 6MV linear accelerator ⁶². The five spectra are shown in Figure 4.4, and are identified by radiation field size and mean photon energy. The mean energy ranged between 1.46 MeV and 0.19 MeV.

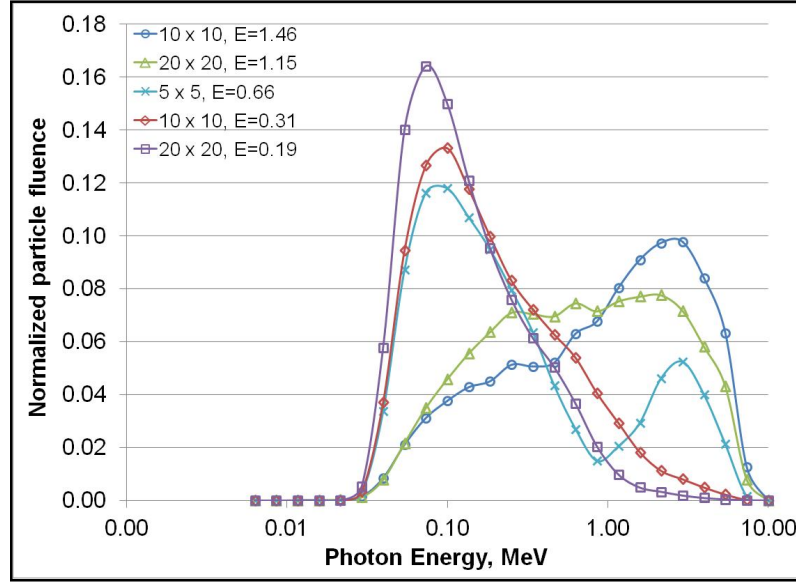


Figure 4.4: Monte Carlo simulated photon spectra for five measurement positions using a Varian 6MV photon beam.

We determined the energy response using Burlin cavity theory for each of these spectra, and then measured the energy response under identical conditions. All measurements were performed using a Varian Clinac 21EX accelerator (Varian Medical Systems, Palo Alto, CA) with a 6MV photon beam, calibrated using standard industry protocols⁷⁷. The measured relative response is defined as the ratio of the dosimeter signal per delivered dose of the experimental condition to the standard condition (signal per delivered dose using a ⁶⁰Co beamline), as defined in Equation 4.8.

$$RR_{measured} = \frac{\left(\frac{Signal}{Dose} \right)_{6MV}}{\left(\frac{Signal}{Dose} \right)_{^{60}Co}} \quad (4.8)$$

The calculated and measured relative response differed by less than 1.7% (root mean square error) for the range of energies examined (Table 4.3).

Table 4.3: Comparison of energy response relative to ^{60}Co ($E=1.25\text{MeV}$) for selected measurement positions in a 6MV therapy beam. Measured values were measured using a Varian 21EX accelerator, calculated values were determined using spectra generated using a benchmarked Monte Carlo model of a Varian 6MV accelerator.

Field Size (cm x cm)	Depth in water (cm)	Distance off central axis (cm)	Mean Photon Energy (MeV)	Calculated Response	Measured Response	Difference (%)
10 x 10	20	0	1.46	1.020	1.028	0.8
20 x 20	5	5	1.15	1.025	1.024	0.0
5 x 5	5	20	0.66	1.100	1.095	-0.4
10 x 10	20	15	0.31	1.196	1.171	-2.1
20 x 20	20	30	0.19	1.408	1.381	-2.0

Comparison to energy response reported in literature

The results calculated using cavity theory were also compared with measured energy response factors that appear in recent literature. The energy response has been evaluated for a range of specific photon beams, in particular kilovoltage beams including mammography, computed tomography (CT), and general radiography^{6; 68-70; 73}. Because of the need for spectral data to complete the analysis, our investigation focused on a comparison to measured energy response for kilovoltage beams by Reft⁶⁹. Spectra were generated using the SpekCalc program³⁷ to match the beam quality (using peak photon energy and first half-value layer) of the corresponding spectra used by Reft. Calculated energy responses were made with cavity theory using these spectra and values were compared to those reported by Reft (Table 4.4). The results showed good agreement, with average absolute differences within 6%.

Table 4.4: Comparison of calculated energy response relative to ^{60}Co ($E=1.25\text{MeV}$) determined using cavity theory for OSLD to measured values reported in the literature for photon beams of varying energies.

Beam Specifier	Mean Photon Energy ^a (keV)	Half-Value Layer ^a	Calculated response	Literature Reported Response ^b	Percent Difference
125 kVp	53.3	3.4 mm Al	3.27	3.40	-3.7%
150 kVp	67.2	0.42 mm Cu	2.59	2.92	-11.2%
200 kVp	81.3	0.82 mm Cu	2.10	2.11	-0.6%
250 kVp	109	1.92 mm Cu	1.52	1.64	-7.3%

^aSpekCalc, ³⁷; ^bReft (2009)

4.4 Discussion

The response of $\text{Al}_2\text{O}_3\text{:C}$ OSLDs is dependent on radiation energy and is dominated by differences in photon interactions, most notably photoelectric interactions, between the dosimeter and the medium. Burlin cavity theory was used to theoretically determine the response of Al_2O_3 as a function of photon energy. At low energies ($E < 100$ keV), the dosimeter can overrespond by a factor of 3.5 or more relative to ^{60}Co . This would mean that unless accounted for, the dosimeter reading would report a dose 3.5 times higher than the actual dose to water at that location. For higher photon energies ($E > 1$ MeV), the dosimeter has a response close to that of water. This is consistent with findings in the literature that report a difference in the energy response between 6 MV photon beams and ^{60}Co of 1% to 4.5%^{69; 73}, and less than 2% between 6 and 18 MV photons^{58; 69; 73}. However, measurement using OSLD in photon beams that include a considerable low-energy component will be affected by this exaggerated response and may need to be corrected.

The energy response was calculated for a sample of polyenergetic beams and compared to measured values (Table 4.3) as well as values reported in the literature (Table 4.4). For the Monte Carlo simulated spectra examined, our Burlin-cavity calculated energy responses showed good agreement with measured energy responses (1.7% root mean square error). A comparison with energy response values reported in the literature⁶⁹ had more varied agreement. The difference between the cavity theory response and measured energy response in the literature varied from less than 1% to 11%, with an average difference of 5.7%. While spectra were matched using half-value layer, mean energy, and filtration, there likely remain differences between the spectra used to complete the measurements and those generated using SpekCalc. The reduced agreement for the literature comparison is attributed to inherent differences between the SpekCalc and actual spectra. This difference also suggests that when relative response is calculated with Burlin cavity theory, as conducted here, a major source of uncertainty is the detailed knowledge of the underlying spectrum. If the spectrum is very well-known, better than 2% agreement is achievable (Table 4.3). However, uncertainty in the spectrum can readily reduce the agreement to ~10% (Table 4.4).

The calculated energy response based on mean spectral energy differs from the calculated energy response determined using an integration over the entire spectrum, which becomes important for polyenergetic beams. For example, for the three photon spectra of Figure 4.3, the relative energy response was 1.01–1.02 when based on mean energy, but was 1.06–1.12 when the entire spectrum was considered. This difference arises because using the mean photon energy may cause the overresponse of the low-energy component of the spectrum to be underestimated. For the spectra presented here, if the dose was corrected using a factor determined using only mean energy, the reported measured dose could be in error by up to 10%.

To further illustrate the importance of considering the complete photon energy spectrum, we have plotted the reported energy response for various photon beams against our Burlin cavity determined energy response (Figure 4.5). Although the line shows general agreement with the points, there are differences of up to 50%. These large differences are the result of the points being plotted at their mean energy and thereby underaccounting for the overresponse at low energy. When the full spectrum is considered, the cavity theory accurately predicts such relative responses (as shown in Table 4.3).

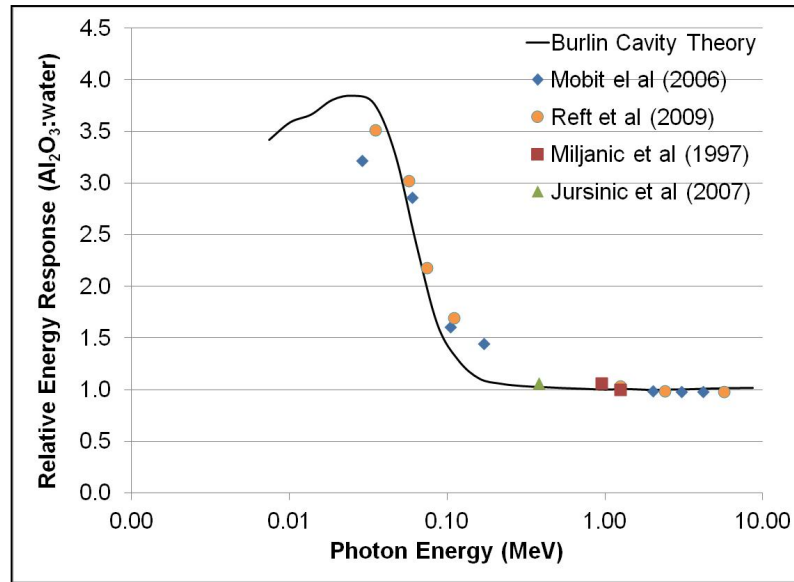


Figure 4.5: Aluminum oxide energy response, when compared based on mean energy and not the complete spectrum, shows substantial errors (up to 50%) in the estimated relative response.

The uncertainty in the cavity theory calculated response includes the uncertainty in the photon energy spectra (dominated by the systematic uncertainty in acquiring accurate spectral information for kV spectra), statistical uncertainty from Monte Carlo simulations, and the uncertainty in the tabulated data for the mass energy absorption coefficients and stopping powers. Spectral information below 10keV was not considered on account of the increased uncertainty in tabulated stopping power data at low energies. The estimated uncertainty in the stopping power is typically on the order of 2-3% for low-Z materials down to 10keV, but on the order of 10% for 1keV⁷⁵. The comparison with measured energy response supports the accuracy of our application of cavity theory to $\text{Al}_2\text{O}_3\text{:C}$ dosimeters for a variety of photon spectra found in a medical setting, including modalities appearing in radiation therapy and diagnostic imaging. Cavity theory calculations are a viable alternative or supplement to measurements or Monte Carlo simulations, however, this analysis has highlighted the importance of accurate spectral information.

OSLDs are often used instead of TLDs due to several substantial advantages. However, because the mass-energy absorption coefficients of Al_2O_3 are greater than that of LiF ⁷⁴, it would be expected that OSLDs would have a disadvantage in the form of a larger energy response. That is, the discrepancy between the dosimeter and water would be magnified for Al_2O_3 compared with LiF . In Figure 4.6, the relative response of LiF TLDs is shown⁶² with the relative response of Al_2O_3 OSLDs, both calculated using Burlin cavity theory.

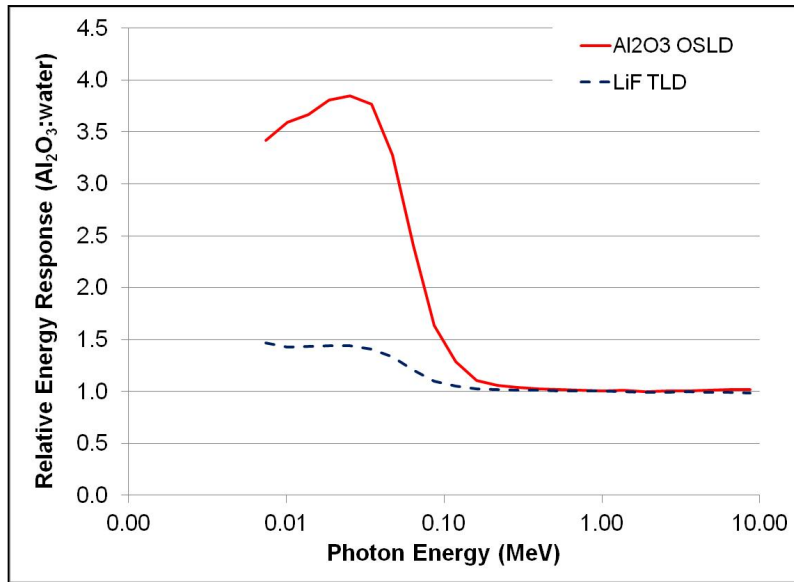


Figure 4.6: Energy response of two common doseimeters: LiF TLD and Al2O3:C OSLD, calculated using Burlin cavity theory.

For low photon energies, LiF may overrespond by about 50% relative to water; for these same energies, Al₂O₃ may overrespond by a factor of 3.5 or more. For higher energies, the response of the dosemeter relative to water is very similar (within a few percent); however, the low-energy scatter component of a photon beam with a high mean energy could nevertheless substantially impact the response of Al₂O₃.

The sensitivity of Burlin cavity-predicted energy response values were only minimally affected by the size of the cavity – the different models had very different values for the parameter d , but the energy response for a monoenergetic photon beam varied by less than 12%. The reason for this was because d decreases with decreasing energy, and is less than 0.2 for photon energies less than 100 keV for each of the three models, which is the energy where the divergence of the mean collisional stopping power and mass energy absorption coefficients begins to occur (Figure 7). At higher energies, the models are different (different values of d), but the ratios of coefficients are the same, so no differences manifest in the energy response. At low energies, the relative coefficients are different, but the models all approach $d=0$, so again, no differences manifest in the energy response.

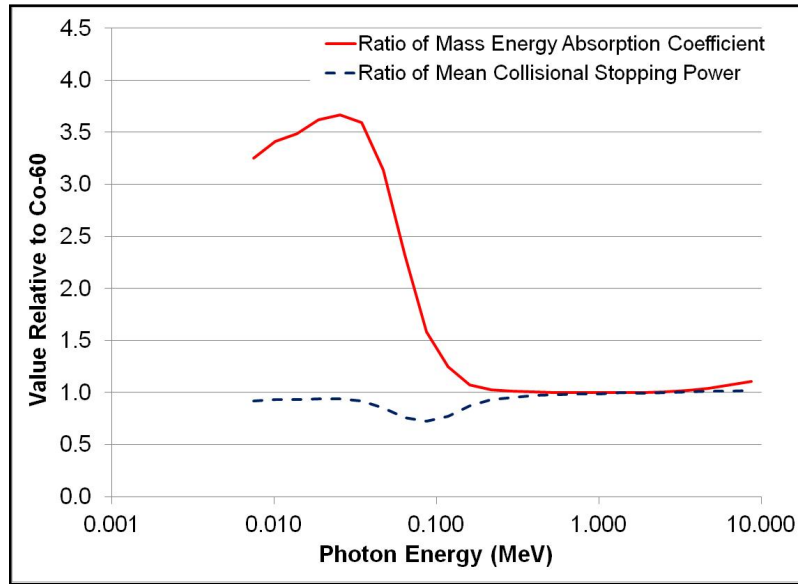


Figure 4.7: The ratio (Al_2O_3 :water) of mean electron collisional stopping power and mass energy absorption coefficient as a function of photon energy.

While Burlin cavity theory offers sufficient estimation of the energy response, there are several limitations to this approach. Our calculations considered only the dosimeter material, and did not include an approximation of the plastic cassette surrounding the dosimeter and the associated dosimetric coefficients. This cassette is very small (<1 mm thickness) and is a tissue-equivalent plastic. Because simulations were performed in water and full scatter conditions, the presence of a water-equivalent cassette will not alter the dosimeter response. The calculation of energy response using cavity theory also does not consider any angular dependence, which has been shown to have an increasing effect as energy decreases^{6; 78}.

4.5 Conclusions

$\text{Al}_2\text{O}_3\text{:C}$ is a common material for use in OSLD, and the use of these dosimeters is becoming increasingly prevalent in medical environments. This material has a known energy dependence, and in this work we determined the energy dependence using general Burlin cavity theory. The approach described here is suitable for determining the energy response of OSLD to any arbitrary spectra without the need for measurement or Monte Carlo calculations, which has not been previously offered in the literature. This approach was found, through a comparison to the responses reported in the literature, to be accurate within 2% on average when reliable spectral data is available. The results of this work have therefore indicated that cavity theory can be used to predict the energy response of OSLD with comparable accuracy to high precision measurements or Monte Carlo simulations.

For low-energy photons ($E < 100$ keV), OSLDs have a substantial overresponse – as much as a factor of 3.5 for some energies. If not accounted for, this overresponse could introduce substantial inaccuracies into dose measurement using OSLDs. If calculated with cavity theory, it is necessary to determine such a correction factor using the entire photon energy spectrum rather than the mean photon energy.

Chapter 5: Energy response of optically stimulated luminescent dosimeters for non-reference measurement locations in a 6MV photon beam

Chapter 3 was published in the journal of Physics, Medicine, and Biology in April 2012 [Phys. Med. Biol. 57 (2012) 2505-2515]. Written permission has been obtained from the journal for use of these materials in this dissertation.

5.1 Introduction

Measurement of radiation dose is important for machine calibration, quality assurance, and patient-specific measurements. Optically stimulated luminescent dosimeters (OSLDs) have become increasingly popular in clinical settings as they are suitable for both machine output verification and patient-specific or *in vivo* measurements. Moreover, they have a number of potential advantages over other dosimeters. For example, they are sensitive to a wide dose range (10 μ Gy to 100 Gy), they can be read multiple times with minimal signal loss, and they are small, robust, and reusable^{58; 59; 61; 79}. Correspondingly, OSLD nanoDots (Landauer, Inc., Glenwood, IL) have replaced TLD in the remote output verification service of the Radiological Physics Center (RPC)^{10; 80}.

Carbon-doped aluminum oxide ($\text{Al}_2\text{O}_3\text{:C}$) is the most commonly used OSLD material in the medical environment. The underlying process by which energy is deposited and trapped in the crystal structure of $\text{Al}_2\text{O}_3\text{:C}$ is similar to that of thermoluminescent materials; the difference is that, after excitation, the crystal is stimulated using visible light as opposed to heat⁶¹.

The response of $\text{Al}_2\text{O}_3\text{:C}$ is complex in that it is dependent on several factors including dose delivered, total accumulated dose, time since irradiation, and photon energy^{58; 69; 78; 79; 81; 82}. The focus of this work is the energy response of OSLD. An energy correction factor is necessary to account for the change in OSLD response due to differences in the photon and electron interactions between the $\text{Al}_2\text{O}_3\text{:C}$ dosimeter material and the medium (for this work, water) in cases where the energy spectrum is different during measurement than it is during calibration of the OSLD. The variation in this factor is dominated by differences in photoelectric interactions and thus has a strong dependence on the effective atomic number of the material. Aluminum oxide has an effective atomic number of 11.28⁵⁹, which is greater than that of both water (~7.22) and LiF TLD (~8.3), indicating that the energy dependence will be greater than that for LiF TLDs.

Although the energy correction factor is typically determined empirically, it can also be estimated using cavity theory. Burlin cavity theory is particularly well suited for OSLDs, where the dose to the cavity is due to both electrons crossing the cavity and secondary electrons created within the cavity^{2; 7; 64}.

For cases where dosimeter calibration is performed at some reference energy (e.g., ^{60}Co), a standard energy correction factor (k_E) has been defined to convert the response of OSLD from a reference beam (e.g., ^{60}Co) to a different energy (e.g., 6 MV)⁴¹. For experimental measurements that take place at the same nominal photon energy as calibration (i.e., determined on the central axis at a depth of the maximum dose for a $10 \times 10 \text{ cm}^2$ field), variations in the photon and electron spectra are generally ignored, and no energy correction factor is used. However, studies have shown that the energy spectrum does change as one

departs from the central axis, with different field sizes and depths, inside or outside the treatment field, and in the presence of tissue heterogeneity or field modulation^{27-29; 62; 83}. These variations in the energy spectra will impact the response of energy-dependent dosimeters, and could thereby result in an incorrect measure of dose unless the energy dependence is correctly taken into account. For example, while the mean energy of a 6 MV photon beam has been found to be 1.5 MeV at d_{\max} under reference conditions, outside the treatment field the mean energy can be as low as 0.22 MeV. This difference corresponded to more than a 10% difference in dosimeter response for LiF TLD (Scarboro et al, 2011). Even greater effects would be expected for OSLDs given the larger magnitude of the difference in effective atomic number.

The energy dependence of OSLDs has been reported for many energies and beams^{58; 60; 68-70}, and has been shown to be large (up to a factor of 4) for low energies^{68; 69}. However, studies to date have only examined the energy corrections between different nominal beam energies, generally only on central axis and under reference conditions. To our knowledge, no study has evaluated the difference in energy response introduced by variations in the spectrum at non-reference conditions (i.e., measurements not conducted at d_{\max}). The objective of this study was to quantify the impact of variations in a 6MV photon beam on the response of OSLDs by determining the energy correction factors for a range of clinically relevant spectra associated with a nominal 6MV photon beam.

5.2 Materials and Methods

The OSLDs used in this study were Landauer nanoDots (Landauer, Inc., Glenwood, IL), each consisting of a thin $\text{Al}_2\text{O}_3:\text{C}$ crystal disc with a 4 mm diameter and 0.3 mm thickness encased in a plastic cassette. The plastic cassette is light tight and has a small thickness (<1mm) and was not considered in the calculated energy response. The total dosimeter has dimension 10 x 10 x 2 mm³.

Calculation of the non-reference energy correction factor

A theoretical energy correction factor can be calculated from the relative response of OSLDs to water, $R_{\text{Al}_2\text{O}_3:\text{C}:\text{water}}$, (Equation 5.1) using Burlin cavity theory. This response accounts for differences in the photon and electron interaction coefficients between the dosimeter ($\text{Al}_2\text{O}_3:\text{C}$) and the surrounding medium (water).

$$R_{\text{Al}_2\text{O}_3:\text{C}:\text{water}}(E) = \frac{D_{\text{Al}_2\text{O}_3:\text{C}}(E)}{D_{\text{water}}(E)} = d(E) \times \left(\frac{\bar{S}}{\rho} \right)_{\text{Al}_2\text{O}_3:\text{C}}(E) + [1 - d(E)] \times \left(\frac{\mu_{\text{en}}}{\rho} \right)_{\text{Al}_2\text{O}_3:\text{C}}(E) \quad (5.1)$$

In Equation 5.1, the quantities (\bar{S}/ρ) and (μ_{en}/ρ) indicate the ratios of the average collisional stopping powers⁵⁰ and mass energy absorption coefficients⁷⁴ for the cavity and medium respectively. For $\text{Al}_2\text{O}_3:\text{C}$, the stopping power values were determined on the basis of the weight fraction of the stopping powers of aluminum and oxygen. The parameter d in Equation 5.1 is a function of both the size of the cavity and the incident photon spectra (shown in Figure 5.1), and it describes the electron fluence generated in the cavity wall relative to the initial equilibrium electron fluence. Values of d were determined as a function of photon energy and assuming the $\text{Al}_2\text{O}_3:\text{C}$ disc was a sphere of the same volume (0.0038 cm³).

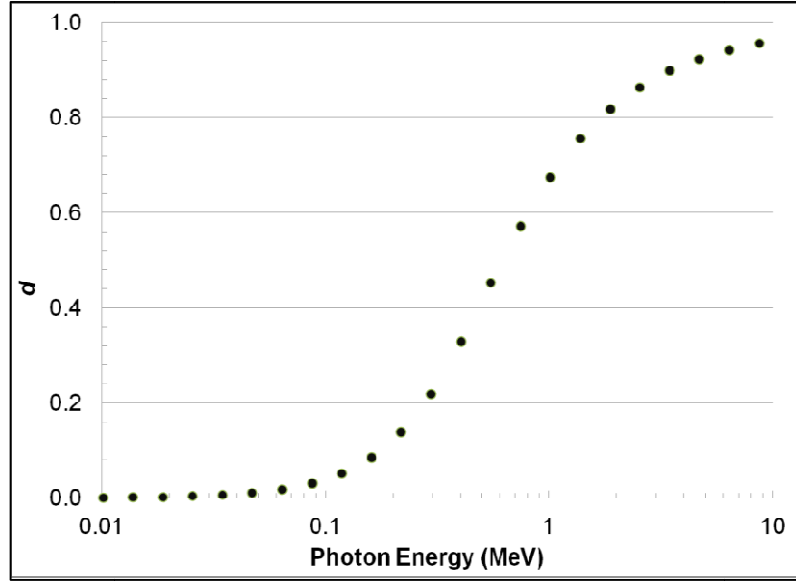


Figure 5.1: Variation of d as a function of (monoenergetic) photon energy.

Based on Equation 5.1, the theoretical impact of spectral variations at non-reference positions on OSLD dose measurements can be determined in Equation 5.2, based on the correction factor: k_{NR} . Equation 5.2 defines the non-reference energy response factor as a function of photon fluence, such that the factor can be determined for an energy-binned photon spectrum.

$$\begin{aligned}
 k_{NR} &= \frac{R_{6MV,reference}}{R_{6MV,non-reference}} \\
 &= \frac{(D_{Al_2O_3:C})_{6MV,reference}}{(D_{Al_2O_3:C})_{6MV,non-reference}} \\
 &= \frac{\sum_i \left[\frac{\varphi_i E_i \left(\frac{\mu_{en}}{\rho} \right)_{water,i} \times (R_{Al_2O_3:water})_i}{\sum_i \varphi_i E_i \left(\frac{\mu_{en}}{\rho} \right)_{water,i}} \right]_{6MV,reference}}{\sum_i \left[\frac{\varphi_i E_i \left(\frac{\mu_{en}}{\rho} \right)_{water,i} \times (R_{Al_2O_3:water})_i}{\sum_i \varphi_i E_i \left(\frac{\mu_{en}}{\rho} \right)_{water,i}} \right]_{6MV,non-reference}} \quad (5.2)
 \end{aligned}$$

In Equation 5.2, φ is the photon fluence, E is the photon energy, and dose is estimated by kerma. A dose measured at an arbitrary position away from the standard reference position should be multiplied by the non-reference energy response factor to correct for the differences in response due to variations in the photon and electron energy spectra.

We determined k_{NR} for a 6 MV beam using Burlin cavity theory for a range of locations within the treatment field (to a depth of 25 cm in water) and outside the treatment field (up to 50 cm from central axis). Each of the selected positions was associated with a unique photon energy spectrum previously determined using a benchmarked Monte Carlo model of a Varian

6 MV linear accelerator^{42-44; 62}. Spectra were generated for symmetric open fields ($5 \times 5 \text{ cm}^2$, $10 \times 10 \text{ cm}^2$, and $20 \times 20 \text{ cm}^2$) open fields in the presence of heterogeneities (bone and lung), and for a modulated beam. To estimate the spectral variations caused by bone or lung tissue, 9cm of the heterogeneous material was added above the position of interest (SSD remained unchanged). The modulated beam simulations were conducted by partitioning a $10 \times 10 \text{ cm}^2$ field into five separate but uniform beamlets ($2 \text{ cm} \times 10 \text{ cm}$). Additional information on the simulation details can be found in a previous publication⁶².

The uncertainty in the calculated k_{NR} values was dominated by statistical uncertainty in the Monte Carlo calculated photon spectra and was approximately 2%.

Measurement of the non-reference energy correction factor

The energy response and corresponding non-reference energy correction factors were determined using a second approach: direct measurement using an ion chamber and OSLD. All measurements were performed using a Varian Clinac 21EX accelerator (Varian Medical Systems, Palo Alto, CA) with a 6 MV photon beam, calibrated using the TG-51 protocol⁷⁷. The measurements were performed in a $48 \times 48 \times 41 \text{ cm}^3$ water phantom (Blue Phantom, Scanditronix Wellhofer, Uppsala, Sweden) at 100 cm SSD. Fifteen measurement locations (corresponding to positions simulated using the Monte Carlo model) were selected that included in-field and out-of-field locations for $10 \times 10 \text{ cm}^2$, $5 \times 5 \text{ cm}^2$, and $20 \times 20 \text{ cm}^2$ open fields as well as an intensity modulated radiation therapy (IMRT) field. The IMRT field was created to duplicate the simulated field – 5 uniform beamlets of $2 \text{ cm} \times 10 \text{ cm}$. The depth in the water phantom was also varied; doses were measured at depths of 1.6, 5, and 20 cm and at varying distances from central axis. At each location in the water phantom, dose was measured using both OSLDs and a PTW model TN30013 Farmer-type 0.6 cm^3 ionization chamber (PTW Associates, Freiburg, Germany).

The dose at each measurement point location was determined using the AAPM TG-21 protocol⁴⁸ to allow a more detailed calculation of dose than TG-51. The correction factors used for each individual measurement location were based on the photon spectrum occurring at that location (as calculated by Monte Carlo simulations), such that the energy response inherent to the ion chamber was accounted for in the determination of the dose. The details of these factors have been discussed previously⁶². The dose to water was determined using the following expression (Equation 3).

$$D_{med} = \overline{M}_{raw} P_{TP} P_{elec} P_{pol} N_{gas} \left(\frac{L}{\rho} \right)_{gas}^{med} P_{ion} P_{repl} P_{wall} \quad (5.3)$$

Using a custom built solid water holder (Figure 5.2), nanoDots were irradiated at the same locations and under the same conditions as the ion chamber measurements. All measurements were made with the nanoDot disc perpendicular to the primary beam axis. Two OSLD were irradiated at each measurement location, and each dosimeter was read three times for a total of six readings at each location. The dosimeters were read using an InLight Microstar OSL reader (Landauer, Inc., Glenwood, IL) which was operated in continuous wave mode for a 7 second read time. All OSLD were calibrated and read by the RPC using their standard protocol, and the signal was converted to dose according to Equation 5.4, where the average signal (\overline{M}_{corr}) from three readings of the dosimeter (each individually corrected for depletion), is further corrected by the dosimeter's individual sensitivity ($k_{s,i}$), system sensitivity ($C_{D,w}$), fading (k_F), linearity (k_L), and reference energy (k_E), corrections.

$$D_w = \overline{M}_{corr} \times C_{D,w} \times k_{s,i} \times k_F \times k_L \times k_E \quad (5.4)$$

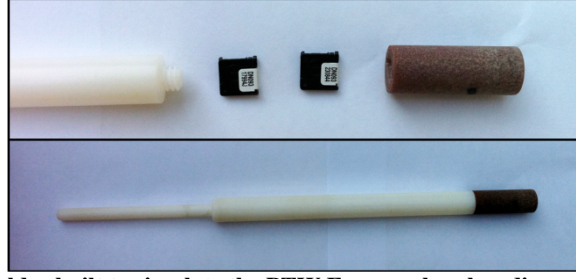


Figure 5.2 Custom OSLD holder built to simulate the PTW Farmer chamber dimensions. The holder is constructed of solid water and holds two OSLD nanoDots. Shown disassembled (above) and assembled (below).

Using the fully corrected ion chamber-determined dose and OSLD-determined dose, the measured non-reference energy correction factor (k_{NR}) was determined using Equation 5.5. k_{NR} values were normalized to unity at the reference position (100 cm SSD, $10 \times 10 \text{ cm}^2$, d_{max} , central axis).

$$k_{NR} = \frac{D_{IonChamber}}{D_{OSLD}} \quad (5.5)$$

The estimated uncertainty of the k_{NR} determination measurements is approximately 2.0% for in-field locations and 2.6% for out-of-field locations. These uncertainties arise from a 1.7% uncertainty in the OSLD dose reading and OSLD correction factors used by the RPC, and 1-2% uncertainty in the ion chamber readings and TG-21 parameters (depending on measurement location).

5.3 Results

Energy correction factors determined using Burlin Cavity Theory

The values of the theoretical calculated energy correction factor for OSLD using Burlin cavity theory ranged from 0.69 to 1.00 and are shown in Figure 5.3 as a function of the mean spectral energy (as defined by the Monte Carlo simulations) at the dosimeter location.

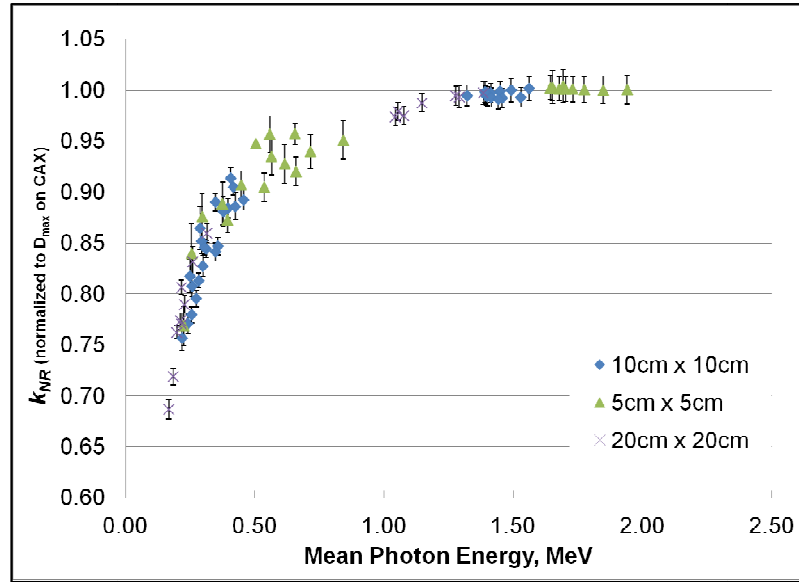


Figure 5.3 Non-reference energy correction factor (k_{NR}) calculated using Burlin cavity theory as a function of mean spectral energy. The error bars represent the one-sigma uncertainty.

For in-field measurement positions, we found small variations in the theoretical k_{NR} value for the spectra investigated relative to the response at the reference position (Table 5.1). The energy response was less than 1% different for all in-field locations for both the $10 \times 10 \text{ cm}^2$ and $5 \times 5 \text{ cm}^2$ field sizes. However, for the $20 \times 20 \text{ cm}^2$ field size, the energy spectra were notably softer (particularly with depth), and k_{NR} for some in-field positions varied by as much as 3% from the reference correction factor. That is, the dosimeters over-responded by as much as 3% (correction factor of 0.97).

The addition of field modulation caused a slight hardening of the photon spectra for in-field measurement positions; the mean photon energy was increased relative to the standard $10 \times 10 \text{ cm}^2$ field (Table 5.1). However, there was also a large contribution of lower-energy scatter to the IMRT spectra such that the associated theoretical k_{NR} for positions within the field was negligibly impacted.

Table 5.1. Calculated energy response factor (k_{NR}) values for spectral variations (determined via Monte Carlo simulations) occurring at selected in-field locations for a 6-MV photon beam.

Field size (cm \times cm)	Heterogeneity	Depth (cm)	Distance off-axis (cm)	Mean Photon Energy (MeV)	k_{NR}
10 \times 10	--	1.6	0	1.49	1.00
10 \times 10	--	20	0	1.46	0.99
10 \times 10	Bone	20	0	1.49	0.99
10 \times 10	Lung	20	0	1.39	0.99
10 \times 10	--	20	5	1.44	0.99
10 \times 10	Bone	20	5	1.48	0.99
10 \times 10	Lung	20	5	1.39	0.99
5 \times 5	--	20	0	1.85	1.00
20 \times 20	--	1.6	0	1.29	0.99
20 \times 20	--	20	0	1.03	0.97
20 \times 20	--	5	5	1.15	0.99
20 \times 20	--	20	5	1.04	0.97
IMRT Field	--	1.6	0	1.68	1.00
IMRT Field	--	5	0	1.54	1.00
IMRT Field	--	10	0	1.52	1.00
IMRT Field	--	20	0	1.59	0.99
IMRT Field	--	20	5	1.61	0.99

The calculated energy response showed considerably more variation for out-of-field locations (Table 5.2), where the spectra contained more low-energy photons. For these out-of-field positions, k_{NR} values ranged from 0.69 to 0.95 (ie., the OSLD over-responded by 5 to 31%). Although the correction factor generally increases with decreasing mean spectral energy, there is some dependence on the specifics of the unique spectra. For example, two different spectra for a 5 \times 5 cm² field had the same mean photon energy (0.66 MeV), but required different energy correction factors (0.92 vs. 0.95). These differences arise because of the strongly non-linear relationship between energy and the extent of OSLD over-response, especially for low-energy photons. Spectra that have a large low-energy component will have a larger correction factor.

Table 5.2. Calculated energy response factor (k_{NR}) values for spectral variations (determined via Monte Carlo simulations) occurring at selected out-of-field locations for a 6-MV photon beam.

Field size (cm \times cm)	Heterogeneity	Depth (cm)	Distance off-axis (cm)	Mean Photon Energy (MeV)	k_{NR}
10 \times 10	--	1.6	20	0.46	0.89
10 \times 10	--	5	15	0.31	0.84
10 \times 10	--	20	15	0.31	0.85
10 \times 10	--	20	20	0.28	0.81
10 \times 10	Bone	20	20	0.29	0.82
10 \times 10	Lung	20	20	0.30	0.83
10 \times 10	--	20	40	0.24	0.77
5 \times 5	--	1.6	20	0.84	0.95
5 \times 5	--	5	20	0.66	0.92
5 \times 5	--	20	15	0.40	0.87
20 \times 20	--	20	20	0.23	0.79
20 \times 20	--	20	30	0.19	0.72
20 \times 20	--	20	50	0.17	0.69
IMRT Field	--	1.6	20	0.58	0.92
IMRT Field	--	5	15	0.34	0.86
IMRT Field	--	20	15	0.32	0.85
IMRT Field	--	20	40	0.26	0.78

For both in-field and out-of-field locations, the presence of heterogeneities did not substantially perturb the photon energy spectra, and thus did not impact the value of k_{NR} . Despite differences in the mean photon energy as a result the addition of heterogeneous materials, the overall spectra remained fairly consistent (see Figure 7 in Chapter 3). By calculating k_{NR} for spectra perturbed by large amounts of bone or lung tissue (9cm), the values provided are conservative – normal amounts of heterogeneities in the field would likely have an even smaller impact.

Comparison of calculated and measured energy correction factors

A comparison of k_{NR} at 15 unique locations, determined using Burlin cavity theory and measurements, are shown in Figure 5.4.

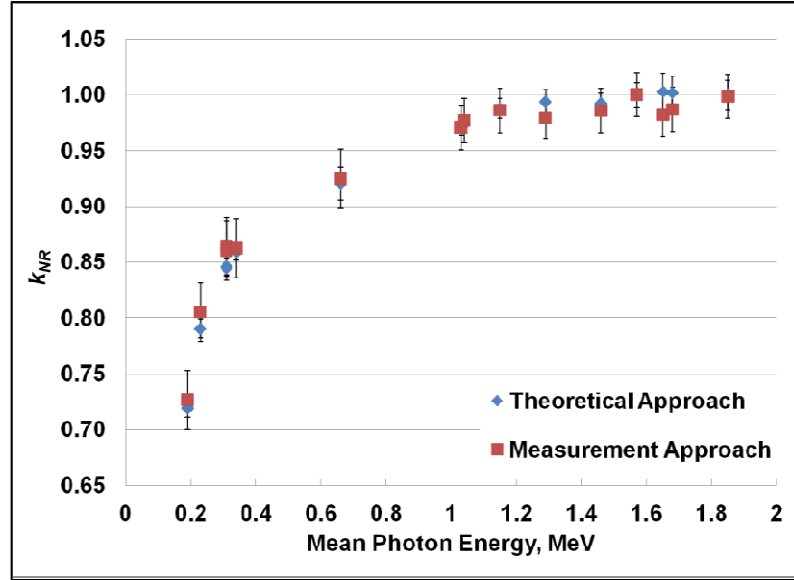


Figure 5.4: Comparison of theoretical and measured energy response factor (k_{NR}) for 15 unique positions in 6MV photon beam.

On average, the measured k_{NR} and the calculated k_{NR} differed by 1%. Although the measured correction factor was typically slightly smaller than that calculated with cavity theory at the higher mean photon energies, the relationship reversed itself at the lower energies. However, the differences never exceeded the uncertainty in the measurements and theoretical response.

5.4 Discussion

OSLD are useful for determining dose in radiotherapy beams. These dosimeters are small and can be easily positioned to collect dose information for measurement conditions that do not coincide with the reference location. Standard energy correction factors only correct for the OSLD energy dependence based on the nominal photon energy (the photon spectrum that occurs at the reference position where calibration has taken place: on central axis at d_{max} in a $10 \times 10 \text{ cm}^2$ field at 100 cm SSD). However, this work has found that an additional energy correction factor may be necessary to account for differences in the spectrum at non-reference locations. For the field sizes and treatment parameters considered in this work, k_{NR} ranged from 0.69 to 1.00 (Table 5.1, Table 5.2). It is interesting to note that the non-reference correction factors determined in this work associated with a 6 MV beam can be much larger than the typical k_E values used for the differences between nominal beam energies. That is, the energy correction factor to convert between ^{60}Co and 6 MV or 18 MV (generally 1-5%, depending on the unique characteristics of the batch) can be much smaller than the energy correction factors necessary to convert between different measurement locations in a single 6 MV beam ($k_{NR}=0.84$ for $10 \times 10 \text{ cm}^2$ field, 5 cm depth, 15 cm off-axis). This highlights the importance of considering the measurement conditions when determining the energy correction factor, rather than simply the nominal beam energy to measure the dose (particularly at these out-of-field locations) with high accuracy.

We found that for most in-field locations, OSLDs over-respond by less than 1% relative to the reference location, requiring an energy correction factor between 0.99 and 1.00. The uncertainty in OSL dosimetry is generally larger than 1%, so the added uncertainty introduced by neglecting k_{NR} under these circumstances is relatively minor. Therefore for such situations,

k_{NR} should not be included. However, for large field sizes at large off-axis distances within the field borders or at deep depths, the spectra are relatively soft, the energy correction factor can exceed 3%. Accounting for this k_{NR} may be necessary depending on the desired precision of the dose measurement, but neglecting it could require the uncertainty in the OSLD reported dose to be increased.

For out-of-field measurement locations, the OSLD response showed greater variation. The correction factors for out-of-field positions ranged from 0.69 to 0.95, implying that out-of-field measurements would be inaccurate by at least 5% or more if energy effects are not accounted for completely. The low-energy spectra that often occur at out-of-field locations could cause OSLDs to overrespond by more than 30% relative to the reference position. Out-of-field dosimetry generally requires less accuracy than in-field dosimetry. However, the correction factors presented here are sizable. In practice, an appropriate k_{NR} can be estimated from the tabular data presented in this work. Failure to account for k_{NR} in out-of-field OSLD dosimetry would result in a substantially overestimated dose. Such inaccurate out-of-field doses could negatively impact fetal dose or pacemaker patient management, or skew estimated risks of secondary cancers, especially if the off axis distances are large.

Although mean spectral energy is convenient for tabulating the energy correction factor, the non-reference energy correction factor is dependent on the specifics of the spectrum for an arbitrary location. Unfortunately, complete spectral data are generally unavailable for arbitrary measurement locations away from the beam reference position. Thus, although a non-reference energy correction factor is still needed for such measurement locations when using OSLDs, without complete spectral information there may be residual uncertainty in the value of the energy correction factor. For example, consideration of the complete spectra changed the non-reference energy response factor by as much as 3% for the same mean energy. While this difference is not negligible, it is clearly less than the uncertainty introduced if a non-reference energy factor is not used for out-of-field measurement locations. As an additional consideration, linear accelerators from different manufacturers can have different spectra for the same nominal energy⁸⁴. Consequently the energy correction factors generated for a Varian beamline may be slightly different for a Siemens or Elekta accelerator. Further study is warranted to determine such corrected factors, but the presented data is preferable to no correction factor at all.

We have determined the non-reference energy correction factor (k_{NR}) using a theoretical approach using fundamental Burlin cavity theory and found it to be in good agreement with the measured energy correction factor. The calculated correction factor considered only the active dosimeter and did not include the plastic cassette, which is very small (<1 mm thickness) and is a tissue-equivalent plastic. Furthermore, the disc was approximated as a sphere of equivalent volume, which could introduce some uncertainty into the cavity theory calculations. The calculated correction factor accounts for deviations in the photon energy spectra from the reference point of calibration for measurement locations that do not coincide with the point of calibration. This factor does not replace the standard OSLD energy correction factor (k_E) that accounts for differences between nominal beam energies, although in some cases, k_{NR} will be larger than k_E . Rather, k_{NR} should be an additional multiplicative correction factor incorporated into the OSLD dose calculation formalism to account for the non-reference measurement conditions when necessary.

5.5 Conclusions

Optically stimulated luminescent dosimeters are becoming an increasingly popular option to measure or verify the absorbed dose in radiotherapy, and they are useful for measuring dose both inside and outside the treatment field. However, OSLDs are not as accurate when they are used to measure dose at locations that do not coincide with the reference position because the energy spectrum is not constant at all locations. In this work we have determined non-reference energy correction factors that should be applied multiplicatively to the OSLD signal to account for varying detector responses at different measurement locations. Within the treatment field, accounting for this non-reference energy correction may only be occasionally necessary, as most locations resulted in less than 1% perturbation of the dose; however, the dose perturbation may exceed 3%, so caution should be used. Outside the treatment field, the OSLDs over-responded by up to 31%, and often large energy correction factors would be necessary for accurate work. Although the complete spectrum is needed to determine this correction factor for any arbitrary position, in this work we have determined the range of energy correction values for several out-of-field spectra. Despite the inherent uncertainty in calculating correction factors without complete spectra, this uncertainty is less than that introduced by not using a non-reference energy correction factor.

Chapter 6: Characterization of the nanoDot OSL dosimeter for use in CT point dosimetry

6.1 Introduction

Imaging with computed tomography (CT) is performed with ever-increasing frequency, with up to 80 million scans being performed each year in the US alone⁸⁵. Furthermore, CT scans account for almost 50% of the collective population radiation dose from diagnostic procedures³⁰. Despite the numerous benefits offered by this modality, CT studies are not without risk; radiation exposure carries the risk of both acute and long-term effects for sensitive organs, especially among children where the risk can be three times that for adults⁸⁶⁻⁹⁰.

Conventional dose estimations in CT typically rely on measurements using acrylic cylindrical phantoms (Computed Tomography Dose Index, or CTDI phantoms). While such measurements provide estimates of scanner output, they cannot offer reliable estimates of actual patient dose^{31; 91}. Recent overdoses during special CT procedures have highlighted the need for timely, accurate, and reliable patient specific dosimetry⁹²⁻⁹⁴. In fact, some state governments in the US have turned to legislative mandates requiring CT doses to be recorded and verified for all patient exams⁹⁵. Furthermore, there is a growing interest in acquiring better estimates of patient dose from routine CT exams and to also track patient radiation doses. The need for improved CT dosimetry is also relevant to on-going studies seeking to quantify the risk of latent health effects from low radiation doses from CT scans⁹⁶. These studies must overcome the difficult task of determining the actual dose associated with a given CT scan. Recently, AAPM Task Group 204 reported that, depending on the size of the patient and the size of the phantom being used, CTDI_{vol} could provide a significant *underestimate* of patient dose for very small patients (up to 2.5 times underestimate) and could provide an *overestimate* of patient dose for very large patients. In addition, Zhang et al used Monte Carlo simulations to demonstrate that CTDI_{vol} is also an *overestimate* of patient dose in neuroperfusion exams where no (or

limited) table motion is employed. Furthermore, AAPM Task Group 111 has proposed a new dose metric for CT that relies on point dosimeters⁹⁷. Clearly, there is a need to improve upon CTDI_{vol} measurements, both for phantom measurements and when providing patient dose estimates.

Optically stimulated luminescent dosimeters (OSLDs) containing Al_2O_3 offer a potential solution for fast and accurate patient specific CT dosimetry. These dosimeters have rapidly gained popularity for use in measuring absorbed dose in medical settings, especially for radiation therapy applications. NanoDot OSLDs (Landauer, Inc., Glenwood, IL) are commercially available, small, robust, reusable, and have high sensitivity, making them a realistic choice for point measurements in diagnostic imaging. Similar to other luminescent dosimeters, the nanoDot acts as an integrating dosimeter and stores dose information until dosimeter read-out. During irradiation, electrons in the crystal structure of the dosimeter are elevated to a higher and meta-stable energy level. At a later time, the OSLD is read-out, or stimulated with a light-emitting diode (LED), allowing the electrons to fall back to their original energy state, and emitting characteristic light proportional to the amount of absorbed radiation dose. Additionally, OSLD nanoDots have been shown to have no impact on image quality⁹⁸, further indicating their potential for use as a patient dosimeter for CT scanning.

When using OSL technology, the measured output (M_{raw}) after irradiation must be corrected for signal depletion, (k_D) and individual element sensitivity ($k_{s,i}$) to provide an average corrected dosimeter signal (\bar{M}_{corr}), using for three readings of a single dosimeter.

$$\bar{M}_{\text{corr}} = \frac{\sum_j \left(M_{\text{raw},j} k_{d,j} \right)}{j} \times k_{s,i} \quad (6.1)$$

Additionally, the OSLD signal must be corrected for dose-linearity (k_L), fading (k_F), irradiation geometry, (k_G), dosimeter angle (k_θ), and energy dependence (k_E). Each of these factors may perturb the response of this dosimeter and thus require correction factors. Therefore, to obtain a dose estimate

from this dosimeter (denoted as D), the measured signal (\overline{M}_{corr}) will have to be corrected for these factors, as well as the system calibration factor (C_D) as shown in Equation 6.2.

$$D = \overline{M}_{corr} \times C_D \times k_L \times k_F \times k_G \times k_\theta \times k_E \quad (6.2)$$

Characterization of the nanoDot for use in radiotherapy dosimetry has been documented by several authors and the response of this dosimeter at radiotherapy doses (>500 mGy) and in megavoltage beams is well known^{4; 10; 58; 59; 79; 80; 99-101}. However, the substantially lower doses used in CT imaging, as well as the lower photon energy, may result in different characteristics of this dosimeter. Recent publications have provided some data on the use of OSLD in diagnostic settings and made note of their drawbacks,^{6; 102}; however, these previous efforts have not provided clear methods of overcoming these limitations in CT dosimetry.

One example of such a limitation is the angular dependence of the OSLD nanoDot, which has been considered by multiple studies in the literature. Jursinic reported no angular dependence for OSLD used in MV photon applications⁵⁸, yet Kerns et al found a non-trivial angular dependence for 6 and 18 MV photon beams (3% and 4%, respectively) but no angular dependence for a clinical proton beam⁷⁸. Al-Senan and Hatab reported angular effects of up to 70% in mammography, up to 42% for general radiography, and up to 10% in CT applications⁶. While these investigations have highlighted the potential need to apply correction for angular dependence, especially at low energies, the study conditions used to determine this response were inconsistent, and it is unclear how the various results should be applied to clinical measurements in diagnostic imaging environments.

The overresponse of Al_2O_3 —the active component of the nanoDot OSLD—to low energy photons (with respect to water or tissue) has been well documented^{4; 6; 58; 101; 103}. Given the relatively large

effective atomic number of the dosimeter compared with that of water, there is an increased incidence of photoelectric interactions in the dosimeter, leading to a dosimetric over-response relative to the surrounding medium (whether water or tissue). Several investigators have noted this over-response and explored energy effects using both measurements and Monte Carlo simulations^{69; 82; 103}. Despite this, there remains little guidance on appropriate corrections for energy response when using this dosimeter in the clinic. Al-Senan and Hatab provide correction factors as a function of measured half-value layers for general radiography⁶, however these factors were determined without the presence of backscatter material and do not represent a clinically relevant measurement condition for CT. In a study of energy dependence by Reft⁶⁹, the dosimeter response was documented for three nominal energies; however, they give little guidance about how to apply this data. No study in the literature addresses the variations in energy response as a function of scan parameters, and no study addresses the dependence of the energy correction factor on the calibration energy and procedure used.

Therefore, further characterization is needed before this dosimeter can be successfully used in CT dosimetry, either with phantoms or patients, especially with regard to the angular dependence and energy dependence of the nanoDot. While the energy dependence is arguably the principal cause for concern, using these dosimeters in a diagnostic environment warrants a full investigation of all factors that might impact the accuracy of dose calculation. The purpose of this work was to investigate the characteristics of the nanoDot dosimeter that are relevant for accurate point dose measurement in a CT environment. In particular, we examined the signal depletion, signal fading, dose linearity, angular dependence, and energy dependence at common CT energies of 80, 120, and 140 kVp. We also determined the impact on dosimeter response of variations in the CT spectrum as a function of position in a phantom, size of phantom, and scan extent.

6.2 Methods and Materials

The OSLDs evaluated in this study are Landauer nanoDots (Landauer, Inc., Glenwood, IL). These aluminum oxide–based dosimeters ($\text{Al}_2\text{O}_3\text{:C}$) are thin discs of diameter 4 mm and thickness 0.3 mm. The active dosimeter volume is enclosed in a plastic cassette measuring 10 mm x 10 mm x 2 mm (shown in Figure 6.1). The nanoDots are commercially available and are used in the remote dosimetry program of the Radiological Physics Center (The U.T. MD Anderson Cancer Center, Houston, TX)¹⁰⁴. The RPC uses these dosimeters for verification of megavoltage beam calibration, and has performed extensive characterization of the nanoDot in a therapy environment¹⁰⁴.

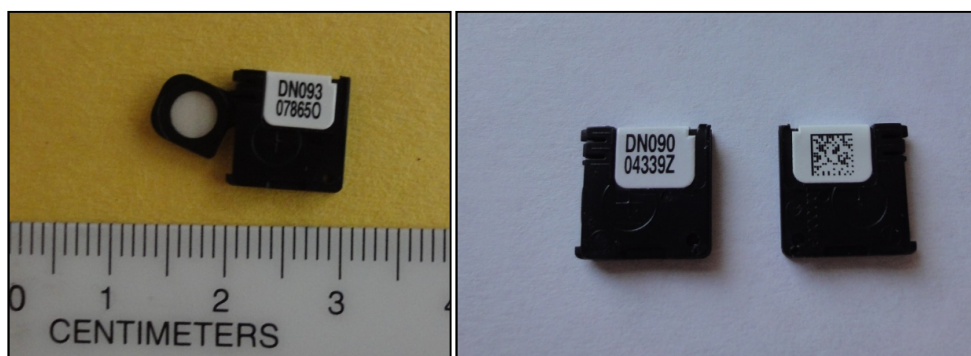


Figure 6.1: OSLD nanoDot: (left) active volume visible when open; (right) front and back of closed dosimeter

All dosimeters used in this study were read using a single InLight Microstar OSL reader (Landauer, Inc., Glenwood, IL) which was operated in continuous wave mode for a 7-second read time. The microStar reader has two readout modes that are automatically selected depending on the dose received by the dosimeter. Based on a short pre-stimulation light, the reader selects either a strong beam (low doses) or weak beam (high doses). For the purposes of this study, all dosimeters were irradiated to low doses (low doses were considered to be less than 200mGy for the purposes of this characterization), and the reader threshold for the readout LED beam was adjusted such that the low-dose (strong LED beam) readout method was used for all readings. The light emitted by the nanoDot is detected by the photomultiplier tube within the reader, and the dosimeter light output is measured in counts.

By exposing the dosimeters to a strong light source (with minimal UV content) the vast majority of electrons in dosimetric traps are cleared, and the dosimeter is effectively “reset”. This cannot be done indefinitely; it is recommended that a fresh dosimeter be used after a cumulative dose of 10-15 Gy is reached⁵⁸. All dosimeters used in this study had cumulative doses much lower than 10Gy, and were annealed using optical bleaching for 24 hours prior to each irradiation. Each dosimeter used was assigned a unique element sensitivity factor that was determined during batch commissioning, where each dosimeter was irradiated to a known dose (250mGy) using ⁶⁰Co. This factor ($k_{s,i}$) represents the relative sensitivity of that individual element to the average sensitivity of the batch.

Experimental CT irradiations were performed on a 64-slice CT scanner (Discovery CT750 HD, GE Healthcare; Milwaukee, WI). The microStar reader was calibrated using dosimeters irradiated to a known dose in air using a 120-kVp CT beam. These dosimeters (standards) were irradiated at the same time as each session of experimental measurements, such that each reading session had a unique calibration factor. The known dose in air was measured using a 0.6-cm³ NIST-traceable farmer-type ion chamber (RadCal Model 10x5) irradiated under identical conditions. The chamber reading (q) was adjusted using the calibration coefficient (N_k) and was also corrected for temperature and pressure effects (P_{TP}) and the electrometer factor (P_{elec}), as directed by AAPM Task Group 111⁹⁷ (Equation 6.3).

$$D_{air} = K_{air} = qP_{TP}P_{elec}N_k \quad (6.3)$$

Basic characterization of the nanoDot was performed using both low-energy and low-dose irradiations. For some parameters, increased precision in the small delivered doses was necessary; to achieve this, these irradiations were performed using an ADCL-maintained ⁶⁰Co beamline. The uncertainty between the predicted and delivered dose was less than 1% for ⁶⁰Co irradiations, which allowed a more accurate characterization of the dose-linearity response, dosimeter reproducibility, and

signal depletion. For these characteristics, the increased energy of the ^{60}Co beamline (1.25MeV) relative to the energy range of CT scans was not relevant. Other parameters, including energy and angular dependence, were determined solely using CT scans.

Basic characterization of the nanoDot

i. Signal depletion

The nanoDot signal is partially depleted during the readout process. This signal depletion was determined for nanoDots for a range of initial doses. The initial doses ranged from 17 mGy (corresponding to approximately 95,000 counts) to 180 mGy (corresponding to approximately 925,000 counts). Eight nanoDots were irradiated using a ^{60}Co beamline, using a standard and identical setup. For these irradiations, two dosimeters were simultaneously irradiated in a small acrylic block (Figure 6.2).



Figure 6.2: Acrylic block used to hold two OSLD nanoDots during ^{60}Co irradiations.

The block was set to a distance of 80 cm from the ^{60}Co source, and the delivered dose was determined based on a decay-correction of the dose rate of the source. Each dosimeter was read 30 sequential times. Signal depletion was measured as the percentage of initial signal for each reading and was recorded for each of the 30 readings. The average depletion as a function of reading number was determined.

ii. Reproducibility

Twenty randomly selected dosimeters were irradiated under identical conditions (using acrylic block shown in Figure 6.2) to ~90mGy in a ^{60}Co beamline. Dosimeters were irradiated two at a time in a custom-built OSLD holder fit into the center chamber of a 10cm diameter CTDI acrylic phantom (Figure 6.3).

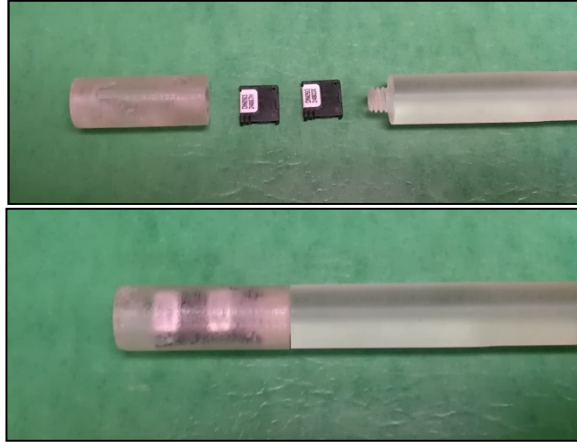


Figure 6.3: Custom OSLD nanoDot acrylic holder used for CT measurements. Shown open (top) and closed (bottom).

Each individual dosimeter was read out three successive times, and each reading was corrected for signal depletion. The average of three readings was corrected for element sensitivity ($k_{s,i}$) and represented the dosimeter signal. The reproducibility of the system (dosimeter and reader) was stated as the mean coefficient of variation of the number of signal counts (standard deviation divided by the mean) for the set of 20 dosimeters. This experiment was repeated (set of dots identically irradiated to a dose of ~50mGy) in a 120kVp CT beam to determine the average signal counts and the coefficient of variation for a lower energy spectrum.

iii. Signal fading

The signal stored in the dosimeter can fade with time as trapped electrons are spontaneously released. This signal fade is particularly large immediately after irradiation. Both Reft and Jursinic et al. showed fading of 40% or more within the 10 minutes following irradiation of 1000 mGy with 6 MV photons^{58; 69}. After the first 10 minutes, the signal fade for high-dose irradiations is small (<2% of signal within 1 month³), but it has not previously been well characterized for low-energy and low-dose

irradiations. Therefore, we irradiated 40 nanoDots in a 120-kVp CT beam under identical conditions (using custom acrylic holder shown in Figure 6.3 placed in center chamber of 10cm diameter CTDI phantom) to a dose of approximately 50mGy and read them out at specific time points between 30 minutes and 18 days post-irradiation.

iv. Dose-response linearity

OSLDs exhibit a supralinear dose response, particularly at larger doses. Therefore, to determine if there is any supralinearity in the response at doses relevant to CT dosimetry, the linearity of the nanoDot was evaluated for doses from 13.6 to 149.6 mGy. Low-dose irradiations were performed in a ^{60}Co beam under standard conditions (and using acrylic phantom shown in Figure 6.2) such that the uncertainty between the predicted and delivered dose was less than 1%. The relationship between the dosimeter signal and the delivered dose was determined, and a linear regression of these data was evaluated to determine whether a nonlinearity correction was needed.

Dependence on Irradiation Geometry

Previous studies have suggested that the OSLD nanoDot signal may be dependent on the incident angle of irradiation^{6; 78}. Because CT employs a rotating x-ray tube, there may be a loss of signal resulting from the x-ray beam incidence on the sides (edges) of the nanoDot relative to a beam that is only perpendicularly incident (towards the ‘flat’ side of the dosimeter) (illustrated in Figure 6.4).

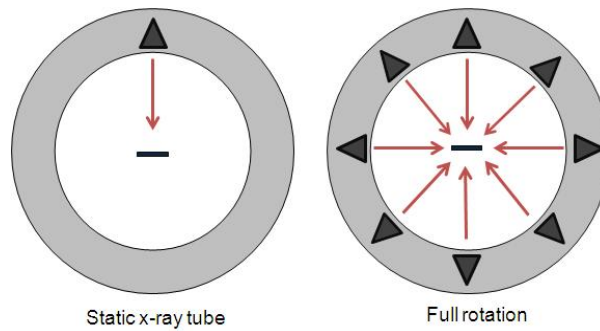


Figure 6.4: Experimental set-up for determining effect of rotating beam irradiation compared to a static beam.

First, to determine the behavior of the nanoDot in a rotating environment versus a static environment, we compared the OSLD response for rotational irradiations (as for CT) versus planar irradiations (as for scout views, or planar x-ray systems that could be used for dosimeter calibration). In this case, the position of the dosimeter itself was kept constant, as shown in Figure 6.4. OSLD were irradiated under each set of conditions, and the signal from each was normalized to an ion chamber response under identical conditions. These measurements were performed under three different conditions: in air, on the top surface of a 16 cm diameter acrylic CTDI head phantom, and inside of a phantom (the center of a 16 cm diameter acrylic CTDI phantom), to investigate the impact of different scatter conditions (from different potential clinical uses and calibrations) on the angular response.

Angular Dependence

For clinical CT dosimetry with the nanoDot, the angle of the dosimeter relative to the CT bore may not always be constant. For patient dosimetry measurements, the dosimeter may be placed on a body contour such that the dosimeter will be tilted relative to the CT bore (the top of the head would be an extreme example of such an orientation). This is a different issue than in the paragraph above, and requires separate evaluation. Most often, the OSLD would be placed such that the active volume is perpendicular (or near-perpendicular) to the incident radiation (as indicated by a dosimeter angle of 0° in Figure 6.5, far left). However, the dosimeter could also be positioned such that the active volume is “edge-on” to the x-ray tube, at a 90° position (Figure 6.5, far right), or at some angle in between. Six

OSLD were irradiated at each of 0, 45, and 90 degrees, and the signal from each was normalized to an ion chamber response under identical scan conditions (the ion chamber was not tilted). Measurements were conducted both in air and inside of the phantom to determine the impact of different scatter environments. For in air measurements, the dosimeters were placed on a thin piece of masking tape which was secured on either side of the CT bore with the dosimeters at the appropriate angle relative to the CT beam. Measurements inside of the phantom were made using a custom-built acrylic OSLD holder which fit inside of the 16cm CTDI phantom. The holder could be tilted such that the dosimeters were at the appropriate angle relative to the x-ray tube.

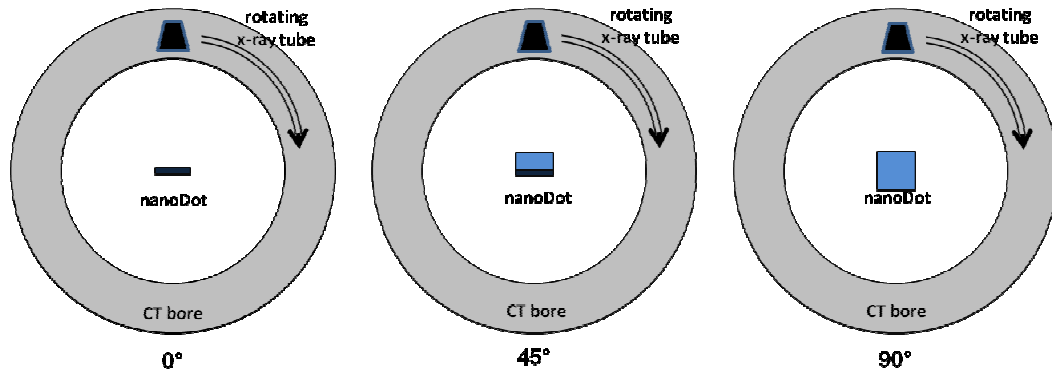


Figure 6.5: Experimental set up for determining OSLD signal dependence on angle of dosimeter relative to CT gantry.

Energy dependence

An energy correction factor (k_E) is necessary in cases where the energy spectrum used to irradiate the nanoDots differs from the energy spectrum used to calibrate the dosimeter (in this set of experiments, a 120kVp CT scan with the dosimeter placed in air at isocenter was used as the reference/calibration condition) and establish the system calibration factor (C_D). Fundamentally, the energy correction factor is equal to the ratio of the dosimeter signal per delivered dose under reference conditions (for determining the system calibration) to the experimental conditions, as shown in Equation 6.4, where D denotes dose and M denotes dosimeter signal⁴¹.

$$k_E = \frac{D_{exp} M_{ref}}{M_{exp} D_{ref}} \quad (6.4)$$

This factor accounts for differences in the photon and electron interactions between the $Al_2O_3:C$ dosimeter material and the measurement medium for the two energy spectra. The energy response is dominated by differences in photoelectric interactions and thus has a strong dependence on the effective atomic number of the material versus medium. k_E can be determined empirically or by using cavity theory¹⁰³, where the dose to the cavity is due to both electrons crossing the cavity and secondary electrons created within the cavity^{2; 7; 64}. When using this approach, the calculated dose to the dosimeter ($D_{Al_2O_3:C}$) represents the dosimeter signal, which is determined through the application of cavity theory. Thus, the energy correction factor can be defined as follows (Eq. 6.5):

$$k_E = \frac{\left(\frac{D_{Al_2O_3:C}}{D_{medium}} \right)_{ReferenceEnergy}}{\left(\frac{D_{Al_2O_3:C}}{D_{medium}} \right)_{ExperimentalEnergy}} \quad (6.5)$$

To determine k_E using cavity theory, detailed knowledge of the experimental and reference energy spectra are needed. While differences in the nominal energy of the calibration and experimental spectra (e.g., 120 kVp calibration vs. 80 kVp experimental measurements) are the primary source of energy effects, variations in scan and phantom parameters may also change the energy spectrum and therefore the dosimeter response. These variations depend on phantom (or patient) size and scan extent (which can significantly affect the local scatter conditions and therefore the resulting spectrum incident on the dosimeter) as well as dosimeter position (which can affect the degree of beam hardening of the incident spectrum), which will also have an effect on the spectrum incident on the

detector. For all helical scans, a pitch of unity was used. To understand the range of variations relevant to clinical scan techniques, we examined a range of CT energy spectra. A benchmarked Monte Carlo model of a GE scanner³⁹ was used to simulate the photon energy spectrum as a function of nominal energy (kVp), phantom size (body or head CTDI phantom), depth in phantom (surface, periphery, or center), and scan extent. In total, 28 unique spectra were simulated, including an in-air spectrum representing the calibration conditions (120 kVp in air at isocenter, not shown in Table 6.1). The scan parameters for each of the conditions simulated are given in Table 6.1 in order of increasing mean spectral energy.

Table 6.1: Scan parameters, CTDI phantom, position in phantom, and mean spectral energy for conditions simulated using benchmarked MCNP model of GE VCT scanner. Center and peripheral positions in phantom correspond to center and peripheral (1cm depth) chambers in the CTDI phantoms.

kVp	CTDI Phantom Size	Position in Phantom	Scan Type	Scan Extent (mm)	Mean Spectral Energy (keV)
80	16cm	Center	Helical	150	43.80
80	16cm	Center	Axial	40	45.35
80	16cm	Peripheral	Helical	150	45.88
80	16cm	Peripheral	Axial	40	46.78
80	16cm	Surface	Helical	150	47.89
80	16cm	Surface	Axial	40	48.61
120	32cm	Center	Helical	150	51.66
120	32cm	Center	Axial	40	54.69
140	32cm	Center	Helical	150	54.98
120	16cm	Center	Axial	40	55.31
140	16cm	Center	Helical	150	55.43
120	32cm	Peripheral	Helical	150	57.79
120	16cm	Peripheral	Axial	40	57.90
140	16cm	Center	Axial	40	58.05
140	32cm	Center	Axial	40	58.65
120	32cm	Periphery	Axial	40	59.53
140	16cm	Peripheral	Helical	150	59.57
120	32cm	Surface	Helical	150	60.72
120	16cm	Surface	Axial	40	60.75
140	16cm	Peripheral	Axial	40	61.52
120	32cm	Surface	Axial	40	62.15
140	32cm	Peripheral	Helical	150	62.72
140	16cm	Surface	Helical	150	63.19
140	16cm	Surface	Axial	40	64.85
140	32cm	Peripheral	Axial	40	65.02
140	32cm	Surface	Helical	150	66.35
140	32cm	Surface	Axial	40	68.28

Using the simulated spectra, the dose to medium (air) was determined using a kerma approximation, as shown in Equation 6.6. In this expression, the energy fluence, Ψ_E , was calculated per discrete energy bin, the mass energy absorption coefficients ($\frac{\mu_{en}}{\rho}$) were collected from data tables maintained by NIST⁷⁴. The sum of the dose over all energies represents the total dose to air.

$$D_{air} = \sum_E \Psi_E \left(\frac{\mu_{en}}{\rho} \right)_{air, E} \quad (6.6)$$

Standard Burlin cavity theory was applied to calculate the corresponding dose to aluminum oxide (Eq. 6.7).

$$D_{Al_2O_3:C} = D_{air} \cdot \left[d(E) * \frac{\left(\frac{\bar{S}}{\rho} \right)_{Al_2O_3:C} (E)}{\left(\frac{\bar{S}}{\rho} \right)_{air} (E)} + (1 - d(E)) \frac{\left(\frac{\mu_{en}}{\rho} \right)_{Al_2O_3:C} (E)}{\left(\frac{\mu_{en}}{\rho} \right)_{air} (E)} \right] \quad (6.7)$$

The parameter $d(E)$ represents the ratio of the electron fluence generated in the cavity wall versus the initial equilibrium fluence; this parameter is a function of cavity size and incident photon energy. Details regarding the calculation of the parameter d have been described in a previous publication¹⁰³. Values for the mass stopping power ($\frac{\bar{S}}{\rho}$) and mass energy absorption coefficients ($\frac{\mu_{en}}{\rho}$) for the respective materials were obtained from standard literature sources^{50; 74; 75}. The dose to both air and aluminum oxide were determined for both experimental spectra and the calibration spectra such that a theoretical energy correction factor (k_E) was determined for all experimental spectra simulated.

To verify the calculated energy correction factors, we also measured energy correction factors for a subset of the simulated experimental conditions. All measurements were conducted using standard

acrylic CTDI phantoms using both nanoDots and a farmer-type ion chamber. The dose to the ion chamber was defined as per TG-111⁹⁷ using Equation 6.8, where q denotes the chamber signal, P_{TP} is the temperature and pressure correction factor, P_{elec} is the electrometer calibration factor, and N_k is the chamber calibration factor, defined on the chamber's calibration report.

$$D_{water} = K_{air} \left(\frac{\mu_{en}}{\rho} \right)_{air}^{water} = q P_{TP} P_{elec} N_k \left(\frac{\mu_{en}}{\rho} \right)_{air}^{water} \quad (6.8)$$

The measured energy correction factor was the ratio of the signal of the OSLD to the measured ion chamber dose for the reference or calibration condition (120 kVp in air) relative to the experimental condition as shown in Equation 6.9.

$$k_{E,measured} = \frac{\left(\frac{D_{OSLD}}{D_{IonChamber}} \right)_{ReferenceEnergy}}{\left(\frac{D_{OSLD}}{D_{IonChamber}} \right)_{ExperimentalEnergy}} \quad (6.9)$$

6.3 Results

Basic characterization

i. Signal Depletion

On average, the nanoDot signal was depleted by 1.6% per readout when the strong LED (low-dose) beam was used for a 7-second readout. Figure 6.6 displays the average depletion per reading for the eight nanoDots, with an exponential curve fit to the data ($R^2 = 0.995$). There was no relationship between the depletion and the dose delivered to the OSLD (even for doses below 17mGy) as long as the dose level remained below the threshold for the strong LED (low-dose) beam setting.

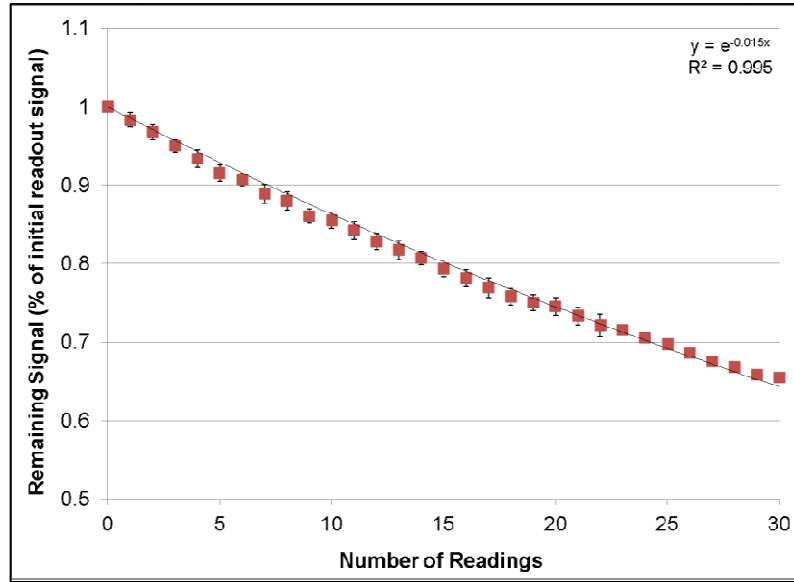


Figure 6.6: Signal depletion over sequential readings of OSLD nanoDots

Signal depletion is a reader-specific characteristic and is also specific to the strength of the LED used. As a result, depletion should be characterized for the reader and for the appropriate dose scale (strong vs. weak LED beam) before performing CT dosimetry. Generally, a depletion correction factor, k_D , which is a function of the number of readings and equal to the inverse of the exponential fit to the data, is applied to the raw OSLD signal counts.

i. Reproducibility

Based on the reproducibility study of 20 nanoDots, the average coefficient of variation (CoV) of the dosimeters was 0.7% for CT irradiations (~50mGy) and 0.8% for ^{60}Co irradiations (~90mGy) (Table 6.2). These values were compared to the average CoV for dosimeters irradiated to a high dose (1000 mGy) using ^{60}Co as part of the RPC remote verification program (representing a fully commissioned batch of over 10,000 OSLD nanoDots) and found to have good agreement (0.8% CoV) (Table 6.2). The maximum CoV was also reported for each condition; this parameter represents the greatest deviation between three readings on the same dosimeter. Signal counts were between 400,000 and 500,000 counts for all dosimeters included in this study.

Table 6.2: Average signal counts, average, and maximum coefficient of variation (CoV) for low-dose irradiations using both CT and ^{60}Co and high-dose irradiations using ^{60}Co

	CT irradiations	^{60}Co irradiations	^{60}Co irradiations
Beam Energy	120kVp (in air)	1.25MeV (in acrylic)	1.25MeV (in acrylic)
Dose Delivered	50mGy	90mGy	1000 mGy
Average CoV	0.7%	0.8%	0.8%
Maximum CoV	1.7%	2.0%	2.0%

ii. Signal Fading

The investigation of the fading of the dosimeter signal indicated a stable signal 30 minutes to 2 weeks after irradiation. Figure 6.7 shows the dosimeter response as a function of time since irradiation for dosimeters irradiated using a 120 kVp CT beam.

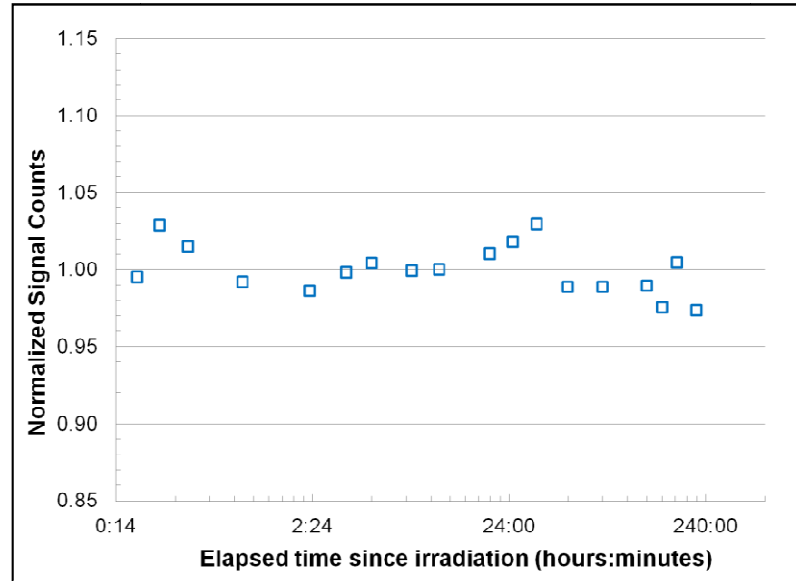


Figure 6.7: Signal fading as a function of elapsed time since irradiation

The stability of the signal for reading times greater than 30 minutes following irradiation is consistent with that in other studies^{58; 69}. When fit with a linear curve, the slope of the line was not significantly different from zero, and therefore, signal fading does not require a correction (k_F) for low-energy, low-dose irradiations within this time period. Because fading is a known phenomenon,

neglecting the effects of fading (or assuming a correction factor of unity) adds some small uncertainty to the final dose calculations, but this uncertainty was estimated to be 1% at the two-sigma level for the time window described, based on the uncertainty in the slope of a linear fit to the data.

iii. Dose Linearity

The dose-linearity of the OSLD nanoDot was determined for a range of diagnostic doses (~13mGy~180mGy). The reading per dose is shown in Figure 6.8a, and dose per reading as a function of delivered dose is shown in Figure 6.8b. The relationship between reading (counts output from the reader) and dose is linear (Figure 6.8a), and neither figure suggests any deviation from a linear dose response. When fit with a linear slope, the slope of dose per reading as a function of dose (Figure 6.8b) is not significantly different from zero, indicating a linear dose response.

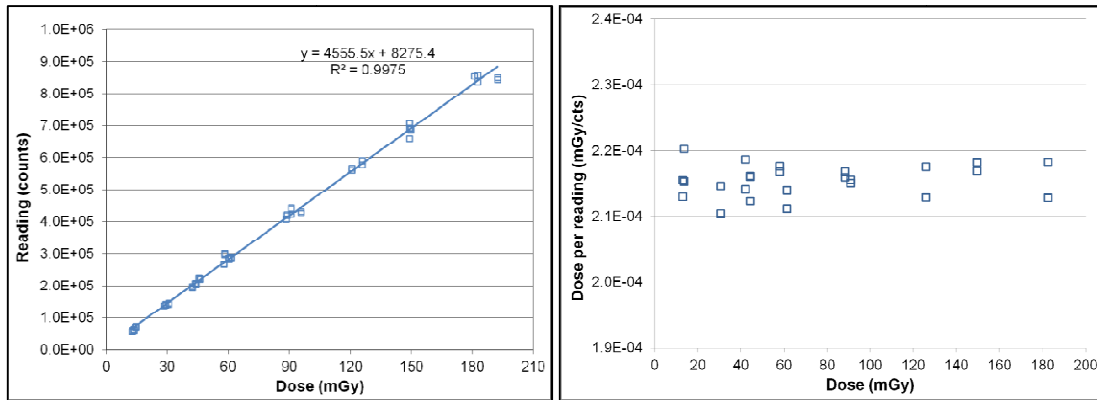


Figure 6.8: Dose-linearity response over a range of low doses. (a) OSLD reading as a function of delivered dose with linear fit to data. (b) Dose per reading as a function of delivered dose

Given the linear dose-response, a dose-linearity correction is not required. Therefore, k_L is equal to unity for applications within this dose range, with an uncertainty of less than 0.8% based on the upper and lower 95th percentile of the slope.

Dependence on Irradiation Geometry

The relative response of the dosimeter using a rotational irradiation versus a static irradiation (Figure 6.4), both in air, inside of the phantom, and on the phantom surface (representing the most clinically relevant condition) are given in Table 6.3.

Table 6.3: Ratio of full rotation OSLD signal to static beam OSLD signal (see Figure 6.4) under various conditions for three nominal CT energies.

Measurement Condition			
kVp	In air	On phantom surface	In center chamber of phantom
80	0.98	0.97	0.99
120	0.98	0.99	0.97
140	0.98	0.95	0.97

The results of these measurements indicate that dosimeters irradiated using a rotating CT beam have a slightly lower signal than those irradiated with a static beam perpendicular to the dosimeter. These results indicate that dosimeters which are irradiated in a rotational environment but have a calibration factor defined using a static beam should be corrected for to compensate for lost signal. This effect is independent of energy, and an irradiation geometry correction factor (k_G) of 1.03 (based on the average under-response of the dosimeter in rotational irradiations) is recommended if the calibration dosimeters are irradiated in a planar fashion instead of a rotational CT environment. Propagation of uncertainties in the measurement using both OSLD and the ion chamber was performed to estimate the total uncertainty of k_G , which was determined to be less than 1%.

Angular Dependence

The variation of signal based on the orientation of the dosimeter relative to the CT bore (Figure 6.5) was described as angular dependence (all these tests were performed under rotating conditions). The normalized OSLD signal for dosimeters placed at non-normal angles is shown in Table 6.4 for the four conditions considered.

Table 6.4: Relative OSLD signal for dosimeters oriented at 0°, 45°, and 90° relative to the signal at 0° (see Figure 6.5) for two nominal energies and two irradiation conditions (in air and in the center of the 16cm diameter CTDI phantom).

Dosimeter Angle	80 kVp		120 kVp	
	In air	In center of phantom	In air	In center of phantom
0	1.00	1.00	1.00	1.00
45	0.98	1.02	0.98	0.98
90	0.84	1.00	0.89	1.00

For dosimeters placed in full scatter conditions (in the center chamber of the phantom) there is no significant angular dependence of the OSLD signal. However, when dosimeters are in air (no scatter medium present), there is a marked decrease in signal when the dosimeter is placed at a 90° angle to the CT bore, or is “edge-on” to the rotating tube. This effect is more pronounced for lower energies, showing a 16% loss in signal relative to the signal for a normally irradiated dosimeter at 80 kVp. For angles less than 90°, such as the 45° dosimeter angle, the angular dependence is within the measurement uncertainty, estimated to be 2%.

Energy dependence

The simulated photon energy spectra for CT scanning parameters including three nominal energies (80, 120, and 140 kVp), two phantom sizes (32cm diameter and 16cm diameter CTDI acrylic phantoms) and on the surface, periphery, and at depth for both short and long scan extents were calculated. In total, 28 spectra were simulated, including the spectrum corresponding to dosimeter calibration conditions (120 kVp in air). A subset of 120 kVp spectra is shown in Figure 6.9.

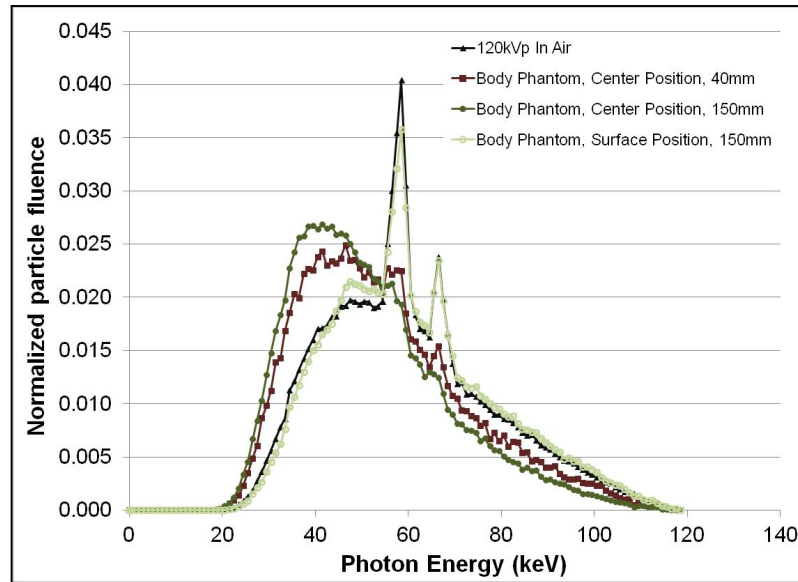


Figure 6.9: Monte Carlo simulated spectra for a 120 kVp beam, standard acrylic 32cm CTDI phantom and two scan extents: a single axial rotation using a 40 mm beam width and a 15 cm helical scan extent (also using a 40 mm beam width).

Differences in spectra were quantified on the basis of difference in the energy response of the nanoDot, calculated using Burlin cavity theory. The range of k_E relative to the reference spectra was 0.80 to 1.15 for all spectra simulated (Figure 6.10).

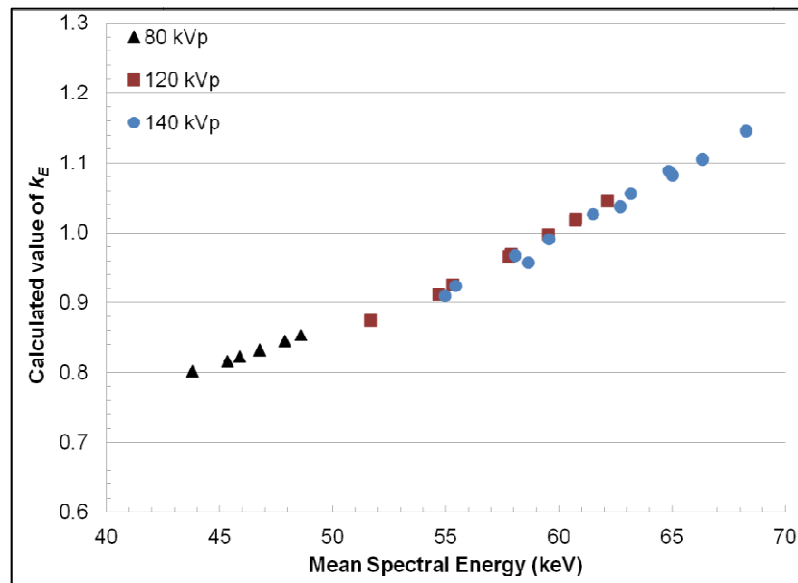


Figure 6.10: Value of energy correction factor (k_E) for all simulated scan conditions as a function of mean spectral energy.

The energy correction factor (k_E) determined using Burlin cavity theory was compared to that determined using direct measurement (using Equation 6.8) for a subset of 11 scan conditions. The average percentage difference between the measured and calculated values of k_E was 4% (absolute value). Dosimeter positions on the phantom surface generally had the worst agreement between measured and calculated energy correction factor; of the subset of conditions investigated in this study, dosimeter placement on the large phantom surface showed a difference of 6.9% between measured k_E and cavity-theory calculated k_E . A closer look at this result in particular implies that the actual spectrum is softer than the simulated spectra. As a result, the measured value of k_E is less than unity, indicating a larger low-energy component (likely scatter) while the calculated value is greater than unity, indicating that the spectra is slightly harder relative to the 120kVp calibration spectrum. The results of this comparison, as well as value of the energy correction factors for this subset of conditions used to verify the cavity theory approach, are provided in Table 6.5.

Table 6.5: Comparison of measured and calculated energy correction factors for a range of clinical CT scanning parameters. Peripheral position denotes chamber located at 1cm depth from phantom surface. Mean spectral energy is defined at the dosimeter position.

CTDI Phantom Size	Position in Phantom	kVp	Scan Extent (mm)	Mean Spectral Energy (keV)	Calculated k_E	Measured k_E	Difference (%)
16cm	Center	80	40	45.35	0.82	0.85	3.2
16cm	Surface	80	150	47.89	0.85	0.86	0.8
32cm	Center	120	150	51.66	0.88	0.92	4.0
32cm	Center	120	40	54.69	0.91	0.95	4.0
16cm	Center	120	40	55.31	0.93	0.97	4.3
16cm	Center	140	40	58.05	0.97	1.03	5.9
32cm	Center	140	40	58.65	0.96	1.01	4.9
32cm	Periphery	120	40	59.53	1.00	1.00	0.0
32cm	Surface	120	150	60.72	1.02	0.95	6.9
16cm	Surface	140	150	63.19	1.06	1.02	3.9
16cm	Surface	140	40	64.85	1.09	1.02	6.8

For the conditions investigated, the calculated energy correction factor ranged from 0.82 to 1.09 relative to a 120 kVp beam in air. Nominal kVp had the largest influence on k_E , followed by the position in the phantom (center position vs. surface position). Changing the phantom size alone (kVp, scan extent, and dosimeter position remaining the same) impacted the magnitude of the correction

factor by 1%- 5%. When dosimeters were positioned in the center or periphery of the phantom, the larger phantom (32cm) required a smaller correction factor (approximately 5% less) relative to the same position in the 16cm diameter phantom. The opposite was true for dosimeters placed on the phantom surface; however, the difference between k_E as a function of phantom size for surface measurement positions was less than 2.5%. Differences in scan extent (single axial rotation vs. 15 cm scan length) represented a smaller effect (1%–4%) on the energy correction factor. The two-sigma uncertainty in k_E was estimated to be less than 5% across the conditions investigated. This investigation was intended to illustrate the range of correction factors that exist for clinically relevant conditions, all relative to a standard CT calibration. It was also important to verify the cavity theory calculation of the energy correction factors.

6.4 Discussion

The basic characteristics of the Landauer OSLD nanoDot and microStar reader were investigated to determine their accuracy for point dosimetry in a CT environment. Although the dosimeter behaved differently than in high-energy and high-dose applications, the results of this investigation support the use of the OSLD nanoDot for CT dosimetry. The reproducibility of this dosimeter was 0.67%, which is comparable that found in other published results for high-dose uses. The dosimeter reproducibility did not appear be dependent on beam-energy or dose; comparable uncertainty was demonstrated for irradiations using either a ^{60}Co beam (1.25MeV) or a 120 kVp CT beam.

The nanoDot dosimeter signal is proportional to the concentration of the filled electron traps at the time of readout and to the power of the light beam used during readout. For dosimeters read using the low-powered light (for high doses), the depletion is small (0.2%–0.3% for a 7-second read) and can generally be neglected. This is not the case for low-dose irradiations employing the strong LED light where we found an average of 1.6% loss of signal per read. Signal depletion can vary between OSLD readers, since the power of the light may vary between readers. It will also vary with read-time; the

reader used for this study used a read time of 7 seconds. Thus, we recommend that this factor be characterized for each reader before CT dosimetry is performed and then applied to each raw signal reading.

Immediately after irradiation, electrons trapped in shallow traps are spontaneously released, causing an overresponse of the dosimeter signal. To avoid this, previous studies have suggested waiting at least 10 minutes following irradiation to allow signal stabilization^{58; 100}. After 10 minutes, the signal is reported to be relatively stable, with only small changes for longer periods of time. This is consistent with the results of the fading investigation reported in Figure 6.7. Signal fading does not appear to be dependent on beam-energy or dose for diagnostic range conditions, as negligible fading was observed in conditions. No correction factor is necessary for CT dosimetry during the time period of 30 minutes to 2 weeks between irradiation and readout. However, careful consideration is necessary if nanoDots are intended to be used as a long-term dosimetric record. To reevaluate a dose at a much later time (longer than 2 weeks) if the dosimeters needed to be stored before reading, a fading correction must be applied to compensate for liberated electrons.

The dose linearity is in agreement with similar studies reported by Al-Senan and Hatab for low-energy photons (mammography, general radiography, and CT)⁶ and is also consistent with studies by Jursinic and Reft, who observed a linear response up to 200 mGy or higher doses^{58; 69}. For doses larger than this, there may be an increase in dosimeter sensitivity, and a dose-linearity correction factor may be needed to adjust for the overresponse. This phenomenon has been observed for doses exceeding 1000mGy, but is a small correction even at relatively high doses (<2%). Even for special CT procedures, such as CT perfusion or angiography studies, it is unlikely that the dose will exceed 1000 mGy, and as a result, no dose-linearity correction factor is recommended for general CT dosimetry.

There are conflicting results on the matter of angular dependence in recent literature. In CT dosimetry, there are two issues that must be considered (irradiation geometry and angular dependence) when using the OSLD nanoDot. Thus far, there is little clarification of these subtleties in the literature. First, differences in the irradiation geometry of experimental dots (exposed to a rotating beam) versus calibration dots (exposed to a static beam) must be considered. This consistent 3% effect was noted regardless of the amount of scatter or nominal energy. Thus, a correction factor is required if there are differences in the irradiation geometry of the calibration dosimeters (e.g., static) and the experimental dosimeters (e.g., rotational), denoted k_G . If all nanoDots are irradiated under the same condition (e.g., both static, or both rotating), no correction is needed.

The angular dependence of the dosimeter relates to the actual physical angle of the dosimeter relative to the CT beam. For measurements performed in air, a loss in signal was noted for dosimeters positioned 90° to the CT beam, or “edge-on.” This effect was magnified for lower energies (16% loss for 80 kVp, 11% loss for 120 kVp). Dosimeter angles less than 90° did not show the same magnitude of effect; the signal loss was within the measurement uncertainty for more shallow angles. Similarly, the angular dependence was not greater than measurement uncertainty for measurements performed in full scatter conditions (in-phantom). Clinical measurements would most likely be performed with the dosimeter placed on the phantom or patient surface. The surface condition represents an “intermediate” scatter condition between that seen in air and in full scatter conditions. Unfortunately, it is difficult to duplicate the surface scatter condition while varying the dosimeter angle such that a directly corresponding measurement can be performed, meaning isolating for the angular dependence under such a condition is exceptionally challenging. Nevertheless, clinical recommendations can be made based on the results presented in Table 6.4. An angular dependence correction (k_θ) is not necessary for dosimeter angles positioned in the CT bore at angles less than 45°, for measurements made in air, inside of the phantom, or on the surface. Dosimeters that are placed with an “edge-on” incidence to the x-ray tube (or 90°) on the surface of a phantom will likely show a decreased signal,

which could be estimated by interpolating the values in Table 6.4. While a fully edge-on measurement on the surface is unlikely, it is prudent to add a correction factor to compensate for signal loss and also recognize that such a measurement will have larger uncertainty.

Variations in the photon energy spectra between the calibration condition and the measurement conditions may impact the response, and, depending on the accuracy desired, an energy correction factor can be applied. The energy response was calculated using cavity theory for a range of clinically relevant CT scanning parameters (Figure 6.10). Measured energy correction factors were compared to the cavity theory values for a subset of conditions in order to validate the calculated values and found to agree within 4% on average (Table 6.5). The agreement between measured and calculated k_E was worst for surface conditions; however, even the largest difference was less than 10%. This comparison was performed to serve as a validation of the cavity theory approach to estimating a correction factor for low-energy CT spectra. For calibration performed using a 120 kVp CT beam in air, the spectral variations manifested a difference in dosimeter response of up to 18% for an 80 kVp beam at the center of a 16 cm acrylic phantom. It is important to reiterate that the factors provided in this work validate the cavity theory approach and highlight the range of variation in the energy correction factor for a particular calibration energy and condition. However, these factors were determined for the spectra generated in an acrylic medium. It is possible that the spectra in tissue may be different than the spectra simulated in acrylic. Now that the calculational approach used here has been verified against measurement (Table 6.5), additional work can be done to determine the differences in photon energy spectra for water or tissue as opposed to acrylic.

6.5 Conclusion

The results of this work indicate that the nanoDot dosimeter is suitable for performing CT dosimetry, both as a tool used in machine output verification and as a possible patient dosimeter. The dosimeter response was found to be independent of dose-linearity effects for the range of doses

expected in CT dosimetry, and no fading correction is necessary for dosimeters read out between 30 minutes and 2 weeks following irradiation (although issues such as long-term fading and accumulated dose to the dosimeter require consideration if dots are reused or stored for long periods of time as a dosimetric record). Given the high-powered light required to read out CT doses, the dosimeter signal is depleted during readout and a reader-specific correction factor is recommended. Angular dependence and energy dependence represent the largest perturbing factors on the dosimeter response in CT environment, and may require corrections based on specific measurement and calibration conditions. Overall, when these corrections can be reliably applied, the nanoDot dosimeter is suitable for performing CT dosimetry and is a good option for performing point measurements both in phantom and for patients.

Chapter 7: Establishing standard calibration protocols for OSLD nanoDots in computed tomography dosimetry

7.1 Introduction

Recent literature has indicated an increase in the use of optically stimulated luminescence dosimeters (OSLD) for dose measurement in medical applications, including diagnostic imaging. The OSLD nanoDot, an aluminum oxide based dosimeter, commercially available from Landauer, Inc (Glenwood, IL), has gained popularity due to its small size, sensitivity to a wide dose range, and non-destructive readout method. Aluminum-oxide based dosimeters have been shown not to impact image quality⁹⁸, indicating that the nanoDot has potential to be used for patient dosimetry. Additionally, this dosimeter has proven useful for the measurement of organ doses using phantoms and the verification of machine output in therapy environments^{10; 58; 60; 78-80; 99; 101; 103}, and may also be useful for these applications in a diagnostic environment.

There is particular interest in using the nanoDot for computed tomography (CT) point dosimetry, and while there are some studies which have used OSLD in this capacity^{70; 105; 106}, there are very few studies addressing the dosimeter characterization in a CT environment^{6; 102}, and none which describe standard and appropriate calibration procedures for OSLD dosimetry in a CT environment. Furthermore, the calibration uncertainty has not yet been quantified.

The general formalism for calculating dose using this dosimeter is shown in Equation 7.1, where the absorbed dose, D , at the location of the OSLD is equal to product of the average corrected signal reading (M), the calibration coefficient (C_D), and any additional necessary correction factors (k_i).

$$D = \overline{M}_{corr} \times C_D \times \prod k_i \quad (7.1)$$

To determine the average corrected signal, \overline{M}_{corr} , the raw OSLD reading, (M_{raw}) must first be corrected for signal depletion ($k_{d,i}$) and unique element sensitivity ($k_{s,i}$), two parameters that are determined during dosimeter batch commissioning (discussed in Chapter 6). The average corrected signal (Equation 7.2) is the mean value of three depletion-corrected readings of the dosimeter.

$$\overline{M}_{corr} = \frac{\sum_j (M_{raw,j} k_{d,j})}{j} \times k_{s,i} \quad (7.2)$$

Additional correction factors (k_i in Equation 7.1) to the OSLD signal may be necessary depending on the calibration technique and reader settings selected, and these factors include dose-linearity (k_L), signal fading (k_F), irradiation geometry (k_G), angular dependence (k_θ), and energy dependence (k_E). Some of these factors are specific to the manner in which the calibration is performed, and some of them are defined for the entire dosimeter and reader system. Each of these factors have been previously characterized for the nanoDot in a CT environment (Chapter 6).

The calibration procedure determines the value of C_D , and thereby establishes the relationship between the OSLD signal and dose. Currently, the only established calibration procedure is that provided by the vendor, through pre-irradiated dosimeters which are provided with the OSLD reader^{6; 102}. A set of 15 dosimeters are irradiated to five known dose levels (three dosimeters at each dose), and a calibration coefficient as a function of dose is determined for all future reading sessions. This is not an ideal calibration for several reasons. Irradiation of calibration dosimeters is left solely to the vendor. Additionally, by performing only one calibration, instability or fluctuations in the OSLD reader are ignored, and drift in the reader over time is not accounted for. Variations in OSLD sensitivity between batches are neglected.

Furthermore, the vendor-supplied calibration method for measurements in a diagnostic imaging environment is not CT-specific, but defines the response of the dosimeter relative to an 80kVp beam.

One of the main challenges in performing dosimetry using OSLD in diagnostic imaging is the dosimeter's overresponse to low energy photons^{58; 69; 82; 103}. Calibrating the dosimeter with a higher or lower energy than that being used for experimental measurements could introduce large errors into dose measurement unless appropriate energy correction factors (k_E) are used. As a result, the choice of calibration energy and associated energy correction factors are crucial to accurate dosimetry. A standard energy correction factor is provided by the vendor to adjust the response to ~120kVp; however, the spectra in CT can vary drastically, and as shown by previous work (Chapter 6)¹⁰³, the dosimeter response to low-energy photons varies greatly between the energies of 80-140kVp. A conceptually and dosimetrically superior approach to OSLD calibration for CT measurements involves irradiating calibration dosimeters under standard conditions with each set of experimental measurements.

OSLD nanoDots are well suited to CT dosimetry, however to achieve accurate dose measures, careful attention must be paid to the calibration conditions and associated correction factors. The purpose of this investigation was to present two calibration protocols as alternatives to the vendor-supplied calibration that can be used for CT dosimetry, and to quantify the calibration uncertainty of each protocol. In addition to the vendor calibration procedure, we have considered calibration using a 120kVp CT beam and ion chamber, and calibration using a ⁶⁰Co beamline (appropriate for diagnostic procedures conducted at radiotherapy facilities where the delivery of highly accurate doses are possible compared to diagnostic doses). Finally, phantom measurements were completed using the OSLD nanoDot and each of the three proposed calibration protocols (vendor-supplied, CT free-in-air calibration, and ⁶⁰Co source calibration) and the measured doses were compared with that determined using a calibrated small-volume (0.6cm³) ion chamber.

7.2 Calibration Formalism

Dosimeters

The calibration approaches presented in this work were developed for the nanoDot OSL dosimeters and the InLight microStar OSL reader (Landauer, Inc., Glenwood, IL). The commercially available OSLD nanoDot is an aluminum oxide based dosimeter ($\text{Al}_2\text{O}_3\text{:C}$) enclosed in a light-tight plastic cassette measuring $10\text{ mm} \times 10\text{ mm} \times 2\text{ mm}$. The active dosimeter volume is a thin disc of diameter 4mm and thickness 0.3mm.

The nanoDot dosimeters were read using an inLight microStar OSL reader, operated in continuous mode for a 7-second read time, using the strong LED setting (appropriate for low doses). For this read time and LED intensity, the depletion was approximately 1.6% per reading (Chapter 6), and this correction was applied to all subsequent readings. In general practice, the calibration approaches and correction factors developed herein do not depend on reader specifications such as read time with the exception of signal depletion, which should be characterized for the read time used. Signal depletion need only be determined once for the reading scale used.

To determine absolute dose in CT measurements, we used a RadCal (Monrovia, CA) 10x5-0.6 CT ion chamber. This chamber is a small volume ion chamber with an active volume of 0.6cm^3 . The chamber was previously calibrated in a 120kVp beam by an accredited dose calibration lab (ADCL). The ion chamber was used in conjunction with a RadCal 9010 series electrometer, operated in auto-exposure mode. To convert the measured exposure readings to absorbed dose using the ion chamber, we used the American Association of Physicists in Medicine (AAPM) task group (TG) report 111 protocol (Equation 7.3) using the chamber reading (q), the calibration coefficient (N_k), and appropriate corrections for temperature and pressure effects (P_{TP}) and the electrometer factor (P_{elec}). The ratio of mass energy absorption coefficients was also applied to define the dose to the medium of choice; for this work the medium selected was water.

$$D_{water} = K_{air} \left(\frac{\bar{\mu}_{en}}{\rho} \right)_{air}^{water} = q P_{TP} P_{elec} N_k \left(\frac{\bar{\mu}_{en}}{\rho} \right)_{air}^{water} \quad (7.3)$$

Calibration Protocols

OSLD calibration establishes the relationship between dosimeter signal and dose using “standards” (i.e. OSLD irradiated to a known dose). For each of the three calibration procedures investigated, the OSLD calibration coefficient was defined as the ratio of the known dose (to water) to the OSLD signal, measured in counts, as shown in Equation 7.4.

$$C_D = \frac{\text{Delivered Dose (mGy)}}{\text{OSLD signal (counts)}} \quad (7.4)$$

Water was selected as the reference medium for defining the standard dosimeters using both the CT-based calibration and the ^{60}Co -based calibration. As a result, the absorbed dose calculated using the dosimeters and these protocols is dose to water, regardless of the actual measurement medium.

1. Vendor Calibration Protocol

The first calibration protocol investigated was based on pre-irradiated dosimeters provided by the dosimeter vendor. In this protocol, calibration dosimeters are supplied to provide a calibration coefficient for the reader for a range of clinical uses. These dosimeters are irradiated by the manufacturer on a PMMA phantom using 80kVp x-rays (2.9mmAl HVL) to known delivered dose levels of approximately 0, 3, and 20mGy. The two-sigma uncertainty on the dose delivered to the dosimeters is reported to be $\pm 5\%$ ¹⁰⁷.

In this work, three calibration dosimeters at each dose level of 3mGy and 20mGy were read three times each, and the average of the depletion corrected signal was used to establish the calibration factor, as shown in Equation 7.5.

$$C_{D, Vendor} = \frac{Delivered\ Dose\ (mGy)}{OSLD\ signal\ (counts)} \quad (7.5)$$

An adjustment for the differences in sensitivity in the vendor-supplied dosimeters and the experimental dosimeters was also made, despite the fact that this is not clearly advised in the vendor calibration procedures. The calibration dosimeters had an inherent sensitivity of 0.85 while the experimental dots had an inherent sensitivity of 0.93. A uniform factor of 1.094 was applied to the calibration factor to account for this difference.

2. Free-in-air CT Calibration Protocol

A CT-based calibration protocol relates the dose measured using a calibrated ion chamber to the OSLD signal for dosimeters irradiated under identical conditions using a CT scanner as the radiation source.

In this work, the ion chamber and OSLD standards were irradiated free-in-air using a 120kVp CT beam (Discovery CT750 HD, GE Healthcare; Milwaukee, WI). All calibration measurements were performed with a rotating CT tube using the medium filter and 64 x 0.625 mm detector configuration to provide a ~40mm beam width at isocenter. No table motion was allowed during irradiation. Two nanoDots were positioned at machine isocenter using a piece of tape suspended through the CT bore (although any minimally attenuating support system would work). The OSLD were located at the machine isocenter using laser alignment lights, and the 40mm beam width completely covered both dosimeters (Figure 7.1a). A single axial rotation was used to deliver 140mA with a 1-second rotation time. This procedure was repeated two times, such that six total dosimeters were irradiated in the same fashion. Each of the six OSLDs was read three times, and the average (depletion-corrected) signal was used to describe the dosimeter signal.

A previously calibrated ion chamber (NIST-traceable) was used to measure dose under identical conditions and scanning technique. The ion chamber was positioned on an empty cardboard box and aligned with the active volume intersecting the machine isocenter using laser alignment lights and with the entirety of the chamber's active volume covered by the 40mm beam (Figure 7.1b). This procedure was repeated two additional times to acquire three readings using the ion chamber.

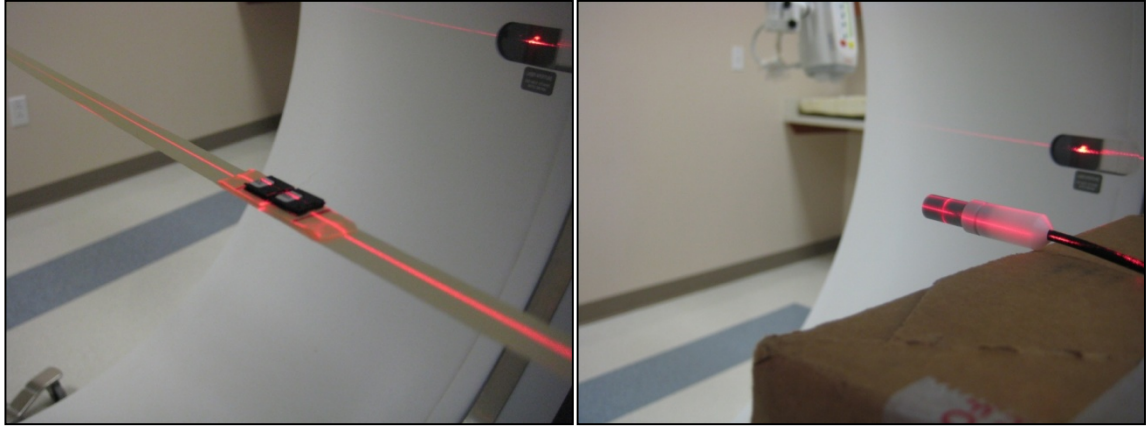


Figure 7.1: (a) OSLD setup for free-in-air CT calibration; (b) ion chamber setup using empty cardboard box for free-in-air calibration

The delivered dose (to water) was defined using the average of the ion chamber measurements (described in Equation 7.3). The calibration coefficient for the in-air CT calibration protocol was defined using Equation 7.6:

$$C_{D,CT} = \frac{\text{Delivered Dose}(mGy)}{\text{OSLD signal}(counts)} \quad (7.6)$$

3. Calibration using ^{60}Co beam

The third calibration protocol used a ^{60}Co beamline (1.25MeV) to determine dose (although a 6 MV beam could also be used), and followed the general procedure used for OSLD calibration by the Radiological Physics Center (RPC, MD Anderson, Houston, Texas) for radiotherapy environments. This procedure relies on megavoltage equipment, and would be most applicable to radiotherapy

environments. The advantage of this protocol is the very high accuracy of the delivered dose to the calibration (standard) OSLDs.

In this work, irradiations were performed using a Theratron 780C cobalt unit (AECL/Theratronics International Ltd., Kanata, Ontario, Canada), which is maintained by an ADCL at The MD Anderson Cancer Center (Houston, TX). Two dosimeters were simultaneously irradiated in a Lucite block (mini-phantom, Figure 7.2) at a distance of 80cm from the cobalt source.



Figure 7.2: Acrylic mini-phantom used for irradiating OSLD standards in ^{60}Co Calibration Protocol

The mini-phantom held the dosimeters at a depth of 0.75cm in Lucite, such that the top of the mini-phantom was actually located 79.25cm from the source. An in-air jig (Figure 7.3) was used to support the mini-phantom and to minimize set-up uncertainties for standard irradiation. For all irradiations, a 10cm \times 10cm field size was used. The dose delivered to the dosimeters was determined based on a decay-correction of the dose rate of the source. For this ^{60}Co unit, the source was installed on September 18, 2005, and the dose rate was determined to be 1479mGy/min on October 15, 2005 using the TG-51 calibration protocol⁷⁷ calculations and an inverse square correction to the appropriate depth. The unit uses a solid state timer, and the time was set such that the dose delivered to the

dosimeters was 45mGy. A constant backscatter factor of 1.035 was applied to the delivered dose to account for the differences in the scatter conditions of the mini-phantom and a full scatter medium. This factor is specific to the energy of the ^{60}Co beam.



Figure 7.3: (a) ^{60}Co unit used for standard irradiations; (b) in-air jig to hold acrylic mini-phantom for ^{60}Co irradiations

Four dosimeters were irradiated using the ^{60}Co unit. Each of the four dosimeters was read three times, and the average (depletion-corrected) signal was used to describe the dosimeter signal. This OSLD signal was compared to the delivered dose with the cobalt beam using the timer setting and the calculated dose rate. The calibration coefficient for the ^{60}Co calibration protocol was defined using Equation 7.7:

$$C_{D, {}^{60}\text{Co}} = \frac{\text{Delivered Dose (mGy)}}{\text{OSLD signal (counts)}} \quad (7.7)$$

Correction factors (k_i)

Because the conditions of these calibration irradiations will not be identical to the conditions of the irradiation of experimental OSLD, correction factors will be necessary to determine the delivered dose accurately. For example, if the standards (OSLD used for dose calibration) are not irradiated with

a photon beam of identical energy characteristics to the experimental OSLD, an energy correction factor (k_E) is necessary to correct for differences in the energy response. The magnitude of this correction may be large if the standards are irradiated in a megavoltage beam, but there may still be a sizeable correction even between a 120 kVp scan in air and an arbitrary scan on a patient (due to changes in the spectrum associated with the different scatter conditions). Similarly, if the standards are irradiated en-face with a static beam but the experimental dosimeters are irradiated with a rotating beam (CT), there is a difference in irradiation geometry (angular effects) that necessitates a geometry correction (k_G). The necessary correction factors for each of the above calibration protocols are described below in the context of validation measurements.

Validation Measurements

A set of measurements was performed to compare the results of the three calibration protocols with the dose measured using a RadCal 10 x 5 CT ion chamber. All measurements were performed using a 64-slice CT scanner (Discovery CT750 HD, GE Healthcare, Milwaukee, WI) and standard acrylic CT Dose Index (CTDI) phantoms each 15cm in length. The large CTDI phantom measured 32cm in diameter; the small phantom measured 16cm in diameter. The OSLD were placed in the center, the periphery, and on the surface of the large CTDI phantom and in the center and on the surface of the small CTDI phantom. For each measurement location, two OSLD were irradiated, and the irradiation was repeated three times for a total of six dosimeters. The irradiation was then repeated with an ion chamber in the same location as the OSLD. The OSLD were read three times and the average (depletion corrected) value was used as the corrected OSLD signal. This same signal was converted to dose using the three different calibration protocols described above, so any differences in OSLD dose for a given measurement condition reflect differences in the calibration protocol.

The scanning techniques used to compare the calibration protocols were selected to represent a range of energy spectra and measurement positions. Eleven unique measurement conditions were

used for this comparison; the scanning parameters and dosimeter position for these eleven cases are shown in Table 7.1. All scans used a 40mm beam width and either axial or helical scans, depending on scan extent (as shown in Table 7.1). Exposures ranged from 200mAs to 900mAs with either 1 or 2 second rotations times, such that the dose delivered to an ion chamber at the same position was between 25-40mGy, within the appropriate range for the OSLD low-dose scale on the microStar reader. Each of these conditions was also simulated using a previously benchmarked Monte Carlo model of a GE VCT CT scanner³⁹; the mean spectral energy at the position of the dosimeter was determined using the simulated photon energy spectra for each set of scanning conditions (Table 7.1).

Table 7.1: Measurement conditions for calibration protocol validation measurements

Measurement Number	CTDI Phantom	Position	kVp	Scan Extent (mm)	Scan Type	Mean Spectral Energy (keV)
1	16cm	Center	80	40	Axial	45.4
2	16cm	Surface	80	150	Helical	47.9
3	32cm	Center	120	150	Helical	51.7
4	32cm	Center	120	40	Axial	54.7
5	16cm	Center	120	40	Axial	55.3
6	16cm	Center	140	40	Axial	58.1
7	32cm	Center	140	40	Axial	58.7
8	32cm	Periphery	120	40	Axial	59.5
9	32cm	Surface	120	150	Helical	60.7
10	16cm	Surface	140	150	Helical	63.2
11	16cm	Surface	140	40	Axial	64.9

The dose to the OSLD was determined using the general formalism (Equation 7.8) with the appropriate correction factors applied for each calibration protocol. For CT dosimetry, the value of k_L , k_F , and k_θ are unity, as long as the dosimeter is not irradiated in an “edge-on” fashion (see Chapter 6 for further information).

$$D = \overline{M}_{corr} \times C_D \times k_L \times k_F \times k_G \times k_\theta \times k_E \quad (7.8)$$

For the vendor-recommended calibration procedure, the dose was determined using the manufacturer-suggested approach, as shown in Equation 7.9, where \overline{M}_{corr} was determined as specified in Equation 7.2, with $k_{s,i}$ equal to unity..

$$D_{Vendor} = \overline{M}_{corr} \times C_{D,Vendor} \times k_{E,Vendor} \quad (7.9)$$

The value of $k_{E, Vendor}$ is specified to be 1.19 for CT measurements (E~120kVp). In this work, $k_{E, Vendor}$ was applied to CT measurements made at 80kVp, 120kVp and 140kVp, as recommended.

The dose to the OSLD for dosimeters following the in-air CT calibration protocol was calculated using Equation 7.10.

$$D_{CT} = \overline{M}_{corr} \times C_{D,CT} \times k_{E,CT} \quad (7.10)$$

The calibration coefficient was determined as in Equation 7.6. Values for $k_{E,CT}$ were determined using the simulated photon energy spectra and Burlin cavity theory, as described in Chapter 6. The calculated values of this factor for the eleven selected cases for both the free-in-air CT calibration and the ^{60}Co calibration are provided in Table 7.2.

Table 7.2: Energy correction factor values for two different calibration protocols

Measurement Position	kVp	Mean Spectral Energy (keV)	$k_{E,CT}$	$k_{E,Co-60}$
1	80	45.4	0.82	0.29
2	80	47.9	0.85	0.30
3	120	51.7	0.88	0.31
4	120	54.7	0.91	0.33
5	120	55.3	0.93	0.33
6	140	58.1	0.97	0.35
7	140	58.7	0.96	0.34
8	120	59.5	1.00	0.36
9	120	60.7	1.02	0.36
10	140	63.2	1.06	0.38
11	140	64.9	1.09	0.39

This factor, k_E , serves to correct the dosimeter response for the over response to low-energy photons relative to the calibration energy. Values less than unity indicate that the experimental measurement conditions included more low-energy photons than the calibration condition.

The dose to the OSLD for dosimeters following the ^{60}Co calibration protocol was determined using Equation 7.10, where the calibration coefficient is described in Equation 7.8 and the energy correction factor is shown Table 7.2.

$$D_{^{60}\text{Co}} = \overline{M}_{corr} \times C_{D,^{60}\text{Co}} \times k_G \times k_{E,^{60}\text{Co}} \quad (7.10)$$

For measurements using the ^{60}Co calibration protocol, an additional correction factor, k_G , was necessary to account for the differences in irradiation geometry between the calibration conditions and the measurement conditions. The calibration coefficient was determined by irradiation performed in a planar fashion (i.e. the active volume of the dosimeter was perpendicular to the beam for the entire irradiation) while the CT dosimeters were irradiated in a rotating fashion. Based on previous data

(provided in Chapter 6), this difference in irradiation geometry impacts the dosimeter signal by approximately 3%, and as a result, the value of k_G is 1.03.

Uncertainty Analysis

The factors k_L , k_F , k_G , k_θ , and k_E have been determined experimentally, and are each fully described in Chapter 6. Because these factors are experimentally determined, they each carry an associated random uncertainty. In this work, the total uncertainty of the determined dose is calculated based on the underlying assumptions that each factor is normally distributed and is independent of the other factors.

The uncertainty of the dose measured by the OSLD is determined and reported as relative uncertainty – or the standard deviation divided by the expected value. The uncertainty in the corrected OSLD reading depends on the relative uncertainty in the depletion-corrected OSLD reading as well as the relative uncertainty in the element sensitivity factor, and was determined using Equation 7.11.

$$\frac{\sigma_{\overline{M}_{corr}}}{\overline{M}_{corr}} = \sqrt{\left(\frac{\sigma_{M_{raw}}}{M_{raw}}\right)^2 + \left(\frac{\sigma_{k_{s,i}}}{k_{s,i}}\right)^2} \quad (7.11)$$

Next, the relative uncertainty in the calibration coefficient is a function of the corrected OSLD reading for the dosimeters used as standards and the uncertainty in the delivered dose (Equation 7.12)

$$\frac{\sigma_{C_D}}{C_D} = \sqrt{\left(\frac{\sigma_{D_S}}{D_S}\right)^2 + \left(\frac{\sigma_{\overline{M}_{corr}}}{\overline{M}_{corr}}\right)^2} \quad (7.12)$$

The relative uncertainty in D_{OSLD} can be derived in terms of the individual variances and partial differentials of dose when Equation 7.1 is treated as the product of independent variables required to calculate dose in each protocol (Equations 7.13 and 7.14 respectively)

$$\frac{\sigma_{D,Co-60}}{D_{Co-60}} = \sqrt{\left(\frac{\sigma_{\overline{M}_{corr}}}{\overline{M}_{corr}}\right)^2 + \left(\frac{\sigma_{C_D}}{C_D}\right)^2 + \left(\frac{\sigma_{k_F}}{k_F}\right)^2 + \left(\frac{\sigma_{k_L}}{k_L}\right)^2 + \left(\frac{\sigma_{k_G}}{k_G}\right)^2 + \left(\frac{\sigma_{k_\theta}}{k_\theta}\right)^2 + \left(\frac{\sigma_{k_E}}{k_E}\right)^2} \quad (7.13)$$

$$\frac{\sigma_{D,CT}}{D_{CT}} = \sqrt{\left(\frac{\sigma_{\overline{M}_{corr}}}{\overline{M}_{corr}}\right)^2 + \left(\frac{\sigma_{C_D}}{C_D}\right)^2 + \left(\frac{\sigma_{k_F}}{k_F}\right)^2 + \left(\frac{\sigma_{k_L}}{k_L}\right)^2 + \left(\frac{\sigma_{k_\theta}}{k_\theta}\right)^2 + \left(\frac{\sigma_{k_E}}{k_E}\right)^2} \quad (7.14)$$

The relative uncertainty in the dose determined using the vendor calibration protocol was described using equation 7.15. The sources of uncertainty in this method include the uncertainty in the dose delivered to the calibration (standard) dosimeters and the uncertainty in the CT correction factor. The uncertainty in the vendor recommended CT energy correction factor was determined using the actual measured energy correction factors. For the subset of 11 measurement conditions investigated, the average relative uncertainty was 12.4%

$$\frac{\sigma_{D,Vendor}}{D_{Vendor}} = \sqrt{\left(\frac{\sigma_{\overline{M}_{corr}}}{\overline{M}_{corr}}\right)^2 + \left(\frac{\sigma_{C_D}}{C_D}\right)^2 + \left(\frac{\sigma_{k_{Vendor}}}{k_{Vendor}}\right)^2} \quad (7.15)$$

7.3 Results and Discussion

Comparison of Calibration Methods

For a range of measurement conditions – varying measurement position, phantom size, kVp, and scan extent, the dose to the OSLD was determined using each of three calibration protocols. The dose to the OSLD was then compared to the dose measured using a CT ion chamber (which was normalized to unity) and plotted as a function of the mean photon energy for the scan parameters selected (Figure 7.5).

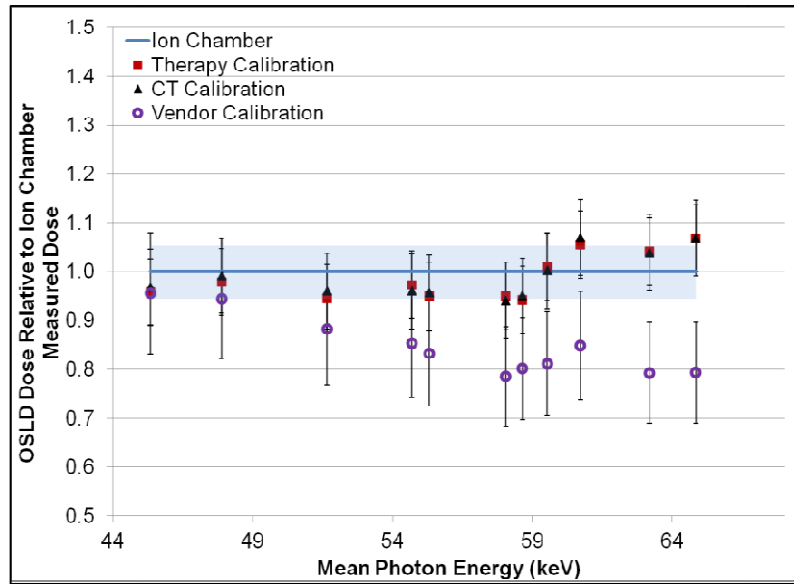


Figure 7.5: Comparison of three OSLD calibration protocols to ion chamber measured dose. Error bars on each dataset represent the total uncertainty for that calibration protocol.

The error bars in Figure 7.5 represent the relative uncertainty for each method, as calculated in Equations 7.13 and 7.14. The uncertainty in the dose measured using the ion chamber was based on the reported uncertainty in the calibration report (5%) and was consistent with the reported variability in dosimetry measurements on modern multi-slice CT scanners in a previous study¹⁰⁸. A comparison of the measured doses is provided in Table 7.3, along with the percent difference from the ion chamber measured dose.

Table 7.3: Comparison of measured OSLD dose using three independent calibration protocols with ion chamber measured absolute dose for subset of 11 measurement conditions.

Measurement Condition	kVp	Mean Spectral Energy	Ion Chamber	Vendor Calibration		In-air CT Calibration		⁶⁰ Co Calibration	
		(keV)	Dose (mGy)	Dose (mGy)	% diff	Dose (mGy)	% diff	Dose (mGy)	% diff
1	80	45.4	31.8	30.4	4.4	30.8	3.2	30.5	4.2
2	80	47.9	28.1	26.6	5.6	27.9	0.8	27.5	2.1
3	120	51.7	29.8	26.3	11.7	28.6	4.0	28.2	5.4
4	120	54.7	28.7	24.5	14.6	27.5	4.0	27.9	2.7
5	120	55.3	34.1	28.4	16.7	32.6	4.3	32.3	5.1
6	140	58.1	33.7	26.5	21.5	31.7	5.9	32.0	5.0
7	140	58.7	34.2	27.4	19.9	32.5	4.9	32.2	5.9
8	120	59.5	36.3	29.4	18.9	36.4	0.2	36.6	0.9
9	120	60.7	27.1	23.0	15.2	29.0	6.9	28.6	5.5
10	140	63.2	34.1	27.1	20.7	35.4	3.9	35.5	4.1
11	140	64.9	32.1	25.5	20.7	34.3	6.8	34.3	6.9
Average					15.5		4.1		4.4

The results of the calibration protocol comparison indicate that similar results can be expected using either the CT-based or ⁶⁰Co-based calibration method. On average, the absolute difference between the dose determined using one of these two methods and that measured using a CT ion chamber was less than 5%. These methods rely on irradiation of standard dosimeters at the time (or on the same day) of experimental irradiations, and assume that all dosimeters used are from the same batch.

The vendor-recommended calibration shows good agreement with the ion chamber for very low experimental energies (80kVp), which are close to the energy of the beam used to irradiate the calibration dosimeters. As the CT energy increases, the agreement between the OSLD and the ion chamber becomes worse – exceeding 20% disagreement for some scan techniques. The vendor energy correction factor (1.19) is applied in order to account for the higher energy of the experimental conditions; however, a signal factor is not adequate for the range of energies seen in clinically relevant scans. The energy correction factor does not completely account for difference in response relative the

80kVp beam for spectra that have more high-energy photons (harder spectra). Furthermore, the harder spectra are generally found on the surface positions, which is also the most likely placement of the dosimeter for *in-vivo* measurements. For the subset of conditions examined in this study, the vendor-recommended calibration technique underestimated the dose by an average of 15.5%.

Both the CT-based calibration and the ^{60}Co -based calibration have been shown to be stronger alternatives to the vendor-recommended approach for calibrating the OSLD nanoDots. Each of these two methods provides a measure of dose well within 10% of a CT ion chamber for a range of scan conditions. For the subset of conditions examined, a very specific energy correction factor was applied to account for variations in the spectra between the calibration conditions and the experimental conditions. Such precise spectral information is rarely known for a particular measurement condition, and energy correction factors based on more general scan parameters (kVp, phantom size, scan extent, etc) are more useful for clinical application.

To examine the range of spectra that may occur based on scan parameters and measurement position, a total of 27 CT spectra were simulated using a benchmarked Monte Carlo model of a GT CT scanner. These spectra were generated for three nominal kVp (80, 120, and 140) and for two phantom sizes (equivalent to the body and head CTDI phantoms). Energy correction factors were determined for each specific measurement location and scan technique relative to the CT-based calibration energy spectrum and a ^{60}Co calibration energy spectrum.

Measurements performed on the surface tended to have harder spectra (or those with a higher energy component). While phantom size does impact the photon energy spectra, the variation in k_E as a result of changing phantom size was less than 5%. As a result, values for k_E are given as a function of nominal kVp and measurement position, which were the two factors that had the largest impact on spectral variations. Additional variations in scan technique were found to have only a small impact on

the value of k_E , changing it by less than a few percent. Recommended values for k_E for the CT-based calibration protocol are provided in Table 7.4 as a function of kVp and measurement position.

Table 7.4: Values of energy correction factor relative to the CT-based calibration protocol for a range of CT parameters

kVp	Surface	Periphery (1cm depth)	Center
80	0.85	0.83	0.81
120	1.03	0.98	0.90
140	1.10	1.03	0.94

For a calibration relative to ^{60}Co , the value of k_E is far from unity because of the large difference in energy between calibration and measurement. Table 7.5 contains the recommended values for k_E for the ^{60}Co based calibration protocol.

Table 7.5: Values of energy correction factor relative to the ^{60}Co based calibration protocol for a range of CT parameters

kVp	Surface	Periphery (1cm depth)	Center
80	0.30	0.30	0.29
120	0.37	0.35	0.33
140	0.39	0.37	0.34

The values provided in Tables 7.4 and 7.5 allow for appropriate energy correction using either of the two proposed calibration protocols. While additional variations in photon energy spectra are expected for a range of scan parameters or phantom (or patient sizes), those variations have not been found to change the value of k_E by more than $\pm 5\%$. In other words, an additional uncertainty of 5% may be added to account for additional spectral uncertainty; however, the provided values adequately account for the energy variations likely to be seen in clinical settings.

Because the spectra may vary for different scanner models and manufacturers, these values should not be universally applied. They are specific to the scanner, scan parameters, and calibration formalism that are described in this work.

Uncertainty Analysis

There are both random and systematic uncertainties associated with the determination of dose using this OSLD system. The uncertainties arise from measurement imprecision in the OSLD signal as well as uncertainties in the various correction factors applied to the signal. Specifically, there are uncertainties in the experimental determination of the factors accounting for signal fading, energy response, and angular response.

The relative uncertainty in the corrected OSLD signal was consistent regardless of the calibration protocol (1.3%) based on the relative uncertainty in the depletion-corrected raw OSLD reading (0.8%) and the relative uncertainty in the element specific sensitivity factor (1.0%). The determination of the calibration coefficient was dependent on the calibration protocol, and the uncertainty in this value was dominated by the uncertainty in the delivered dose to the standard dosimeters. The ^{60}Co -based calibration offers the lowest uncertainty in the delivered dose, and as a result the calibration coefficient using this protocol has a relative uncertainty of 1.6%. Finally, the total uncertainty in the dose determination using each protocol was calculated using Equations 7.13 and 7.14, respectively. The relative uncertainty in the corrected OSLD reading, the calibration coefficient, and the overall dose determination for the three calibration protocols is shown in Table 7.5.

Table 7.6: Relative uncertainties in corrected OSLD signal, calibration coefficient, and dose determination for each calibration protocol.

	Vendor Calibration	CT Free-In-Air Calibration	^{60}Co Calibration
Uncertainty in OSLD reading			
$\frac{\sigma_{\bar{M}_{corr}}}{\bar{M}_{corr}}$	$\pm 1.3\%$	$\pm 1.3\%$	$\pm 1.3\%$
Uncertainty in calibration coefficient			
$\frac{\sigma_{C_D}}{C_D}$	$\pm 5.2\%$	$\pm 5.3\%$	$\pm 1.6\%$
Total uncertainty in calculated dose			
$\frac{\sigma_D}{D}$	$\pm 13.7\%$	$\pm 7.7\%$	$\pm 6.9\%$

The calibration protocol with the lowest overall uncertainty was the ^{60}Co based calibration, largely due to the high level of accuracy in the dose delivered to standard dosimeters. However, this protocol also requires use of a megavoltage accelerator. The CT-based calibration does not require additional equipment or radioactive sources; as a result it is likely the best calibration option for most diagnostic CT clinics. The relative uncertainty in dose measurement using properly calibrated OSLD is 7.7%, which compares favorably to the relative uncertainty achievable with a CT ion chamber under the same conditions (5%). The relative uncertainty on the vendor calibration protocol was the highest of the three examined. This is largely due to the uncertainty in dose delivered to standards, as well as uncertainty in the correction factor to account for energy or other effects.

7.4 Conclusion

In this work, two calibration protocols are presented which are stronger alternatives to the vendor-supplied calibration method for performing CT dosimetry using the OSLD nanoDot. The CT free-In-Air calibration requires a previously calibrated ion chamber, and OSLD standards to be irradiated with a consistent and reproducible scan technique. Energy correction factors are generally necessary using this calibration technique and a table of factors is provided for a range of CT energies, measurement positions, and measurement media using a GT scanner. There is little difference in the value of the energy correction factor as a function of media for this calibration protocol; calibration using ^{60}Co , a higher energy source, requires a larger correction factor which becomes more dependent on the measurement medium (acrylic versus water versus air). Using either the CT free-in-air or ^{60}Co -based calibration approaches, dosimetry with a relative uncertainty of less than $\pm 10\%$ is achievable in a CT environment.

Chapter 8: Summary and Conclusions

8.1 General Summary and Conclusions

The energy dependence of two commonly used dosimeters was characterized for non-reference measurement conditions in a radiotherapy environment. Monte Carlo simulations of the photon energy spectra were completed for a range of clinically relevant conditions, defined by adjusting the field size, the measurement position, field modulation, and by adding heterogeneous materials to the beam path. The impact of spectral variations was evaluated through a calculation of the energy correction factor, a term that is used in both TLD and OSLD dose determination to compensate for differences in response between the calibration spectrum and the measurement spectrum. A theoretical expression for the energy correction factor was derived from fundamental Burlin Cavity Theory, and using the calculated photon energy spectra, an energy correction factor was determined for each unique spectrum.

Measurement position was the largest cause of spectral perturbations in the 6MV beam. The addition of field modulation or heterogeneous material into the beam path did not manifest into large differences in the energy correction factor. As a result, out-of-field measurements generally needed a non-reference energy correction factor to compensate for the overresponse of the dosimeter. While larger uncertainty is generally expected for out of field measurements, failing to account for the softer energy spectra could impact clinical decisions or the outcomes of risk calculations based on inaccurate dosimetry.

Spectral variations impacted the TLD response such that an energy correction factor of up to 12% was needed for some out of field conditions. Spectral variations occurring within the field borders did not have as large of an impact on the energy correction factor – differences of up to 1% were seen for in-field measurements.

Spectral variations were expected to have a larger impact on OSLD response, largely due to the higher effective atomic number of Al_2O_3 relative to tissue. Both calculated energy correction factors

and measured energy correction factors confirmed this – differences of up to 30% were seen for out of field measurements, and in-field spectral variations impacted the dosimeter response by up to 3% depending on the measurement position.

One of the primary outcomes of this work was the development of a theoretically calculated energy correction factor using Burlin Cavity Theory. Good agreement was found between measured and calculated energy correction factors for both dosimeters; average differences of approximately 3.5% were found for both TLD and OSLD.

The OSLD nanoDot was characterized for use in CT dosimetry, and necessary correction factors were provided for this low-dose and low-energy environment. Low dose measurements require a stronger LED light for stimulation of the OSLD, and as a result signal depletion with each reading is larger. A depletion correction factor is necessary, and should be determined before experimental measurements begin. A study of the angular dependence of the nanoDot found that there is very little angular dependence ($<2\%$) for intermediate to full scatter conditions in a CT environment, with the exception of edge-on irradiations. If the dosimeter is positioned such that the entire irradiation is performed in an edge-on fashion, the response will be impacted, and a correction factor should be applied. Signal fading and dose linearity were determined not to impact dose determination, and correction factors of unity should be applied for most typical CT conditions.

Additionally, two new calibration procedures were presented for calibration of the nanoDot for performing CT point dosimetry. These two methods were compared to the vendor recommended calibration procedure and found to have a lower uncertainty over a range of scanning techniques. Using a CT free-in-air calibration procedure, OSLD nanoDots can be used to consistently measure CT dose with less than 10% uncertainty for a range of scanning techniques. Appropriate calibration techniques are crucial to using OSLD in a low-energy environment, and the work completed in this study provides a feasible and clinically relevant solution.

8.2 Evaluation of the Hypothesis

The first part of the hypothesis of this study was that the assumption of a single and constant photon energy spectrum introduces error of at least 5% into dose measurement using TLD and OSLD in typical radiotherapy photon beams. To evaluate this hypothesis, Specific Aims 1 and 2 were carried out through a complete investigation of the photon energy spectra in a radiotherapy environment, and an assessment of the energy correction factor for TLD and OSLD was done using both measurements and cavity theory. For in-field measurement conditions, the hypothesis was proven to be false. Errors of at least 5% were not found using either dosimeter for in-field measurement conditions, despite some perturbations to the photon energy spectra. For out-of-field measurement conditions, the hypothesis was proven to be true. TLD measurements required additional correction factors of up to 12% and OSLD required correction up to 30%.

The second component of the hypothesis of this study was that OSLD nanoDots can be used to measure dose with total uncertainty of less than 20% compared to ion chamber readings in a CT setting. This hypothesis was evaluated through completion of Specific Aims 3 and 4. A full characterization of the OSLD nanoDot was performed and a set of necessary correction factors was determined. Finally, two calibration protocols were presented; each of which achieved uncertainty of less than 10% for CT dosimetry when implemented appropriately. As a result, this component of the hypothesis was proven to be true.

8.3 Future Research and Applications

The consideration of variations in energy spectra in a radiotherapy environment were determined to impact dose calculation for measurement positions outside of the primary field. One of the major applications of out-of-field dosimetry is to provide data for late effects studies, where the risk of development of second malignancies is evaluated. As a future investigation, a re-evaluation of risk estimates based on updated dosimetry should be completed. Given that the dosimeter demonstrates an overresponse to lower photon energies, as those seen in out of field locations, it is expected that a re-

investigation may actually show lower risk of second malignancy compared to that previously determined in studies based on TLD or OSLD measurements. Another application of this result is in evaluation of fetal dose for pregnant women undergoing treatment. Often, treatment is limited based on dose to the fetus; more accurate dosimetry may allow treatment doses to be higher without actually exceeding dose limits to the fetus.

The applications of this work to CT dosimetry are potentially much more wide reaching. The next step in implementing the results of this work in a clinical setting would be through a study of measuring CT dose *in-vivo*. In particular, measurement of lens dose during routine brain studies would provide useful data on the feasibility of a large-scale patient monitoring program.

A comparison between the dose measured using OSLD and the dose indicators provided in CT dose reports at the scanner would be of great use to a clinical CT program. The dose indicators, usually $CTDI_{vol}$ and Dose Length Product (DLP) are based on measurements made in acrylic CTDI phantoms, and are generally poor indicators for the actual patient dose. Nevertheless, these indicators are widely used to monitor patient dose and set dose limits on high-dose procedures. If better dosimetry was available, a more thorough evaluation of the reliability of these indicators could be performed.

References

- ¹Akselrod, M.S. 2011. Fundamentals of Materials, Techniques, and Instrumentation for OSL and FNTD Dosimetry. In American Institute of Physics: Concepts and Trends in Medical Radiation Dosimetry.
- ²Knoll, G.F. 2000. Radiation Detection and Measurement Third Edition. John Wiley and Sons, Inc.
- ³Radiological Physics Center (www.rpc.mdanderson.org). Houston, TX.
- ⁴Yukihara, E.G., P.B.R. Gasparian, G.O. Sawakuchi, C. Ruan, S. Ahmad, C. Kalavagunta, W.J. Clouse, N. Sahoo, and U. Titt. 2010. Medical applications of optically stimulated luminescence dosimeters (OSLDs). *Radiation Measurements* 45(3&6):658-662.
- ⁵Yukihara, E.G., and et al. 2009. An optically stimulated luminescence system to measure dose profiles in x-ray computed tomography. *Phys. Med. Biol.* 54(20):6337.
- ⁶Al-Senan, R.M., and M.R. Hatab. 2011. Characteristics of an OSLD in the diagnostic energy range. *Med. Phys.* 38(7):4396-4405.
- ⁷Attix, F.H. 2004. Introduction to Radiological Physics and Radiation Dosimetry. WILEY-VCH Verlag GmbH & Co.
- ⁸Hosseini-Pooya, M., and M. Jafarizadeh. 2004. Effect of reader and oven annealing on the glow curve structure and fading of a LiF:Mg,Cu,P TL dosimeter. *Journal of Radiological Protection* 24(2):173.
- ⁹Landauer, I. 2010. MicroStar Dosimeter Specifications. www.osldosimetry.com.
- ¹⁰Homnick, J., G. Ibbott, A. Springer, and F. Aguirre. 2008. OSL Dosimeters can be used for Remote Dosimetry. *Int. J. Radiat. Oncol., Biol., Phys.* 72(1):S672-S673.
- ¹¹Toye, W., R. Das, T. Kron, R. Franich, P. Johnston, and G. Duchesne. 2009. An in vivo investigative protocol for HDR prostate brachytherapy using urethral and rectal thermoluminescence dosimetry. *Radiother. Oncol.* 91(2):243-248.

- ¹²Ito, S., B.C. Parker, R. Levine, M.E. Sanders, J. Fontenot, J. Gibbons, and K. Hogstrom. 2011. Verification of Calculated Skin Doses in Postmastectomy Helical Tomotherapy. *Int. J. Radiat. Oncol., Biol., Phys.* 81(2):584-591.
- ¹³Reynders, T., K. Tournel, P. De Coninck, S. Heymann, V. Vinh-Hung, H. Van Parijs, M.I. Duchateau, N. Linthout, T. Gevaert, D. Verellen, and G. Storme. 2009. Dosimetric assessment of static and helical Tomotherapy in the clinical implementation of breast cancer treatments. *Radiother. Oncol.* 93(1):71-79.
- ¹⁴Rong, Y., P. Yadav, J.S. Welsh, T. Fahner, and B. Paliwal. 2012. Postmastectomy radiotherapy with integrated scar boost using helical tomotherapy. *Medical Dosimetry*(0).
- ¹⁵Leal, M.A., C. Viegas, A. Viamonte, A. Campos, D. Braz, and P. Clivland. 2009. Thermoluminescent chip detector for in vivo dosimetry in pelvis and head and neck cancer treatment. *Applied Radiation and Isotopes* 68(4-5):795-798.
- ¹⁶Engstrom, P.E., P. Haraldsson, T. Landberg, H. Sand Hansen, S. Aage Engelholm, and H. Nystrom. 2005. In vivo dose verification of IMRT treated head and neck cancer patients. *Acta Oncologica* 44(6):572-578.
- ¹⁷Schiefer, H., A. Fogliata, G. Nicolini, L. Cozzi, W.W. Seelentag, E. Born, F. Hasenbalg, J. Roth, B. Schnekenburger, K. Munch-Berndl, V. Vallet, M. Pachoud, B. Reiner, G. Dipasquale, B. Krusche, and M.K. Fix. 2010. The Swiss IMRT dosimetry intercomparison using a thorax phantom. *Med. Phys.* 37(8):4424-4431.
- ¹⁸Blais, A.R., E. Lederer, M. Oliver, and K. Leszczynski. 2012. Static and rotational step-and-shoot IMRT treatment plans for the prostate: A risk comparison study. *Med. Phys.* 39(2):1069-1078.
- ¹⁹Surucu, M., M. Yeginer, G.O. Kavak, J. Fan, J.A. Radosevich, and B. Aydogan. 2011. Verification of dose distribution for volumetric modulated arc therapy total marrow irradiation in a humanlike phantom. *Med. Phys.* 39(1):281-288.

- ²⁰Kry, S.F., M. Salehpour, D.S. Followill, M. Stovall, D.A. Kuban, R.A. White, and I.I. Rosen. 2005. Out-of-field photon and neutron dose equivalents from step-and-shoot intensity-modulated radiation therapy. *Int. J. Radiat. Oncol., Biol., Phys.* 62(4):1204-1216.
- ²¹Kry, S.F., P. Michael, F. David, M. Firas, and S. Mohammad. 2007. The use of LiF (TLD-100) as an out-of-field dosimeter. 2007.
- ²²Taddei, P.J., R.M. Howell, S. Krishnan, S.B. Scarboro, D. Mirkovic, and W.D. Newhauser. 2010. Risk of second malignant neoplasm following proton versus intensity-modulated photon radiotherapies for hepatocellular carcinoma. *Phys. Med. Biol.* 55(23):7055.
- ²³Howell, R.M., S.B. Scarboro, P.J. Taddei, S. Krishnan, S.F. Kry, and W.D. Newhauser. 2010. Methodology for determining doses to in-field, out-of-field and partially in-field organs for late effects studies in photon radiotherapy. *Phys. Med. Biol.* 55(23):7009.
- ²⁴Kragl, G., F. Baier, S. Lutz, D. Albrich, M.r. Dalaryd, B. Kroupa, T. Wiezorek, T. Knoos, and D. Georg. 2011. Flattening filter free beams in SBRT and IMRT: Dosimetric assessment of peripheral doses. *Zeitschrift für Medizinische Physik* 21(2):91-101.
- ²⁵Meeks, S.L., A.C. Paulino, E.C. Pennington, J.H. Simon, M.W. Skwarchuk, and J.M. Buatti. 2002. In vivo determination of extra-target doses received from serial tomotherapy. *Radiother. Oncol.* 63(2):217-222.
- ²⁶Reft, C.S., R. Runkel-Muller, and L. Myriantopoulos. 2006. In vivo and phantom measurements of the secondary photon and neutron doses for prostate patients undergoing 18 MV IMRT. *Med. Phys.* 33(10):3734-3742.
- ²⁷Liu, H.H., Verhaegen, F. 2002. An Investigation of Energy Spectrum and Lineal Energy Variations in Mega-voltage Photon Beams used for Radiotherapy. *Radiat. Prot. Dosim.* 99(1-4):425-427.
- ²⁸Jang, S.Y., H.H. Liu, R. Mohan, and J.V. Siebers. 2007. Variations in energy spectra and water-to-material stopping-power ratios in three-dimensional conformal and intensity-modulated photon fields. *Med. Phys.* 34(4):1388-1397.

- ²⁹Ding, G.X. 2002. Energy spectra, angular spread, fluence profiles and dose distributions of 6 and 18 MV photon beams: results of Monte Carlo simulations for a Varian 2100EX accelerator. *Phys. Med. Biol.* 47(7):1025-1046.
- ³⁰2008. UNSCEAR Sources and Effects of Ionizing Radiation.
- ³¹McCrohan, J.L., J.F. Patterson, R.M. Gagne, and H.A. Goldstein. 1987. Average radiation doses in a standard head examination for 250 CT systems. *Radiology* 163(1):263-268.
- ³²Brenner, D. 2010. Should we be concerned about the rapid increase in CT usage? *Rev Environ Health* 25(1):63-68.
- ³³Waggener, R.G., M.M. Blough, J.A. Terry, D. Chen, N.E. Lee, S. Zhang, and W.D. McDavid. 1999. X-ray spectra estimation using attenuation measurements from 25 kVp to 18 MV. *Med. Phys.* 26(7):1269-1278.
- ³⁴Fewell, T.R., R.E. Shuping, and K.E. Healy. 1981. Handbook of Computed Tomography X-Ray Spectra. HHS Publication (FDA), US Government Printing Office, Washington DC.
- ³⁵Boone, J.M., and J.A. Seibert. 1997. An accurate method for computer-generating tungsten anode x-ray spectra from 30 to 140 kV. *Med. Phys.* 24(11):1661-1670.
- ³⁶Verhaegen, F., and J. Seuntjens. 2003. Monte Carlo modelling of external radiotherapy photon beams. *Phys. Med. Biol.* 48(21):R107.
- ³⁷Poludniowski, G., G. Landry, F. DeBlois, P.M. Evans, and F. Verhaegen. 2009. SpekCalc : a program to calculate photon spectra from tungsten anode x-ray tubes. *Phys. Med. Biol.* 54(19):N433.
- ³⁸Fewell, T.R., and R.E. Shuping. 1977. Photon energy distribution of some typical diagnostic x-ray beams. *Med. Phys.* 4(3):187-197.
- ³⁹Turner, A.C., D. Zhang, H.J. Kim, J.J. DeMarco, C.H. Cagnon, E. Angel, D.D. Cody, D.M. Stevens, A.N. Primak, C.H. McCollough, and M.F. McNitt-Gray. 2009. A method to generate equivalent energy spectra and filtration models based on measurement for multidetector CT Monte Carlo dosimetry simulations. *Med. Phys.* 36(6):2154-2164.

- ⁴⁰Zhang, D., C.H. Cagnon, J.P. Villablanca, C.H. McCollough, D.D. Cody, D.M. Stevens, M. Zankl, J.J. Demarco, A.C. Turner, M. Khatonabadi, and M.F. McNitt-Gray. 2012. Peak Skin and Eye Lens Radiation Dose From Brain Perfusion CT Based on Monte Carlo Simulation. *American Journal of Roentgenology* 198(2):412-417.
- ⁴¹Kirby, T.H., W.F. Hanson, and D.A. Johnston. 1992. Uncertainty analysis of absorbed dose calculations from thermoluminescence dosimeters. *Med. Phys.* 19(6):1427-1433.
- ⁴²Kry, S.F., U. Titt, F. Ponisch, D. Followill, O.N. Vassiliev, R.A. White, R. Mohan, and M. Salehpour. 2006. A Monte Carlo model for calculating out-of-field dose from a Varian 6 MV beam. *Med. Phys.* 33(11):4405-4413.
- ⁴³Ponisch, F., U. Titt, S.F. Kry, O.N. Vassiliev, and R. Mohan. 2006. MCNPX simulation of a multileaf collimator. *Med. Phys.* 33(2):402-404.
- ⁴⁴Kry, S.F., U. Titt, D. Followill, F. Ponisch, O.N. Vassiliev, R.A. White, M. Stovall, and M. Salehpour. 2007. A Monte Carlo model for out-of-field dose calculation from high-energy photon therapy. *Med. Phys.* 34(9):3489-3499.
- ⁴⁵Hendricks, J.S. 2004. MCNPX, Version 2.5. e, LA-UR-04-0569.
- ⁴⁶Kase, K., G. Svensson, A. Wolbarst, and M. Marks. 1983. Measurements of dose from secondary radiation outside a treatment field. *Int. J. Radiat. Oncol., Biol., Phys.* 9:7.
- ⁴⁷Shani, G. 2001. Radiation Dosimetry: Instrumentation and Methods, Second Edition. CRC Press.
- ⁴⁸Task Group 21, R.T.C., AAPM. 1983. A protocol for the determination of absorbed dose from high-energy photon and electron beams. *Med. Phys.* 10(6):741.
- ⁴⁹Taylor, R.C., W.F. Hanson, N. Wells, and G.S. Ibbott. 2006. Consistency of absorbed dose to water measurements using 21 ion-chamber models following the AAPM TG51 and TG21 calibration protocols. *Med. Phys.* 33(6):1818.
- ⁵⁰Johns, H.E., and J.R. Cunningham. 1983. The Physics of Radiology, Fourth Edition. Charles C. Thomas.

- ⁵¹Cunningham, J.R., Sontag, M. R. 1980. Displacement corrections used in absorbed dose determination. *Med. Phys.* 7(6):672.
- ⁵²Lempert, G.D., Nath,R., Schulz,R. J. 1983. Fraction of ionization from electrons arising in the wall of an ionization chamber. *Med. Phys.* 10(1):1.
- ⁵³Nunn, A.A., S.D. Davis, J.A. Micka, andL.A. DeWerd. 2008. LiF:Mg,Ti TLD response as a function of photon energy for moderately filtered x-ray spectra in the range of 20-250 kVp relative to Co-60. *Med. Phys.* 35(5):1859-1869.
- ⁵⁴Davis, S.D., C.K. Ross, P.N. Mobit, L. Van der Zwan, W.J. Chase, andK.R. Shortt. 2003. The response of LiF thermoluminescence dosimeters to photon beams in the energy range from 30 kV X rays to 60Co gamma rays. *Radiat. Prot. Dosim.* 106(1):33-43.
- ⁵⁵Konnai, A., N. Nariyama, S. Ohnishi, andN. Odano. 2005. Energy response of LiF and Mg₂SiO₄ TLDs to 10-150 keV monoenergetic photons. *Radiat. Prot. Dosim.* 115(1-4):334-336.
- ⁵⁶Horowitz, Y.S. 1984. Thermoluminescence and Thermoluminescent Dosimetry CRC Press I, editor, Boca Raton, FL.
- ⁵⁷McKeever, S.W.S., M.S. Akselrod, L.E. Colyott, N. Agersnap Larsen, J.C. Polf, andV. Whitley. 1999. Characterisation of Al₂O₃ for Use in Thermally and Optically Stimulated Luminescence Dosimetry. *Radiat. Prot. Dosim.* 84(1-4):163-166.
- ⁵⁸Jursinic, P.A. 2007. Characterization of optically stimulated luminescent dosimeters, OSLDs, for clinical dosimetric measurements. *Med. Phys.* 34(12):4594-4604.
- ⁵⁹Yukihara, E.G., andS.W.S. McKeever. 2008. Optically stimulated luminescence (OSL) dosimetry in medicine. *Phys. Med. Biol.* 53(20):R351.
- ⁶⁰Yukihara, E.G., G. Mardirossian, M. Mirzasadeghi, S. Guduru, andS. Ahmad. 2008. Evaluation of Al₂O₃:C optically stimulated luminescence (OSL) dosimeters for passive dosimetry of high-energy photon and electron beams in radiotherapy. *Med. Phys.* 35(1):260-269.
- ⁶¹Yukihara, E.G., andS.W.S. McKeever. 2011. Optically Stimulated Luminescence: Fundamentals and Applications. Wiley.

- ⁶²Scarboro, S.B., D.S. Followill, R.M. Howell, and S.F. Kry. 2011. Variations in photon energy spectra of a 6 MV beam and their impact on TLD response. *Med. Phys.* 38(5):2619-2628.
- ⁶³Ogunleye, O.T., F.H. Attix, and B.R. Paliwal. 1980. Comparison of Burlin cavity theory with LiF TLD measurements for cobalt-60 gamma rays. *Phys. Med. Biol.* 25(2):203.
- ⁶⁴Miljanic, S., and M. Ranogajec-Komor. 1997. Application of cavity theory to the response of various TLDs to Co-60 gammas degraded in water. *Phys. Med. Biol.* 42(7):1335.
- ⁶⁵Mobit, P. 2002. The Use of Monte Carlo Simulations for Accurate Dose Determination with Thermoluminescent Dosimeter in Radiation Therapy Beams. *Radiat. Prot. Dosim.* 101(1-4):383-386.
- ⁶⁶Beddar, A. 2005. Monte Carlo calculations of the absorbed dose and energy dependence of plastic scintillators. *Med. Phys.* 32(5):1265.
- ⁶⁷Eklund, K., and A. Anders. 2010. Modeling silicon diode dose response factors for small photon fields. *Phys. Med. Biol.* 55(24):7411.
- ⁶⁸Aznar, M.C., J. Medin, B. Hemdal, A. Thilander Klang, L. B. Årter-Jensen, and S. Mattsson. 2005. A Monte Carlo study of the energy dependence of Al₂O₃:C crystals for real-time in vivo dosimetry in mammography. *Radiat. Prot. Dosim.* 114(1-3):444-449.
- ⁶⁹Reft, C.S. 2009. The energy dependence and dose response of a commercial optically stimulated luminescent detector for kilovoltage photon, megavoltage photon, and electron, proton, and carbon beams. *Med. Phys.* 36(5):1690-1699.
- ⁷⁰Yukihara, E.G., C. Ruan, P.B.R. Gasparian, W.J. Clouse, C. Kalavagunta, and S. Ahmad. 2009. An optically stimulated luminescence system to measure dose profiles in x-ray computed tomography. *Phys. Med. Biol.* 54(20):6337.
- ⁷¹El-Faramawy, N.A., H.Y. Goksu, and W. Panzer. 2004. Thermoluminescence dosimetric properties of a new thin beta detector (LiF:Mg, Cu, P; GR-200F) in comparison with highly sensitive Al₂O₃:C beta dosimeters. *Journal of Radiological Protection* 24(3):273.

- ⁷²Rocha, F.D.G., and L.V.E. Caldas. 1999. Characterization of Al₂O₃ sintered pellets for dosimetric applications in radiotherapy. *Journal of Radiological Protection* 19(1):51.
- ⁷³Mobit, P., E. Agyingi, and G. Sandison. 2006. Comparison of the energy-response factor of LiF and Al₂O₃ in radiotherapy beams. *Radiat. Prot. Dosim.* 119(1-4):497-499.
- ⁷⁴Hubbell, J.H., and S.M. Seltzer. 1996. Tables of X-Ray Mass Attenuation Coefficients and Mass Energy-Absorption Coefficients from 1 keV to 20 MeV for Elements Z = 1 to 92 and 48 Additional Substances of Dosimetric Interest. NIST Standard Reference Database 126.
- ⁷⁵Berger, M.J., J.S. Coursey, M.A. Zucker, and J. Chang. 2005. Stopping-Power and Range Tables for Electrons, Protons, and Helium Ions. National Institute of Standards and Technology (NIST), Physical Measurement Laboratory.
- ⁷⁶Janssens, A., G. Eggermont, R. Jacobs, and G. Thielens. 1974. Spectrum perturbation and energy deposition models for stopping power ratio calculations in general cavity theory. *Phys. Med. Biol.* 19(5):619.
- ⁷⁷Almond, P.R., P.J. Biggs, B.M. Coursey, W.F. Hanson, M.S. Huq, R. Nath, and D.W.O. Rogers. 1999. AAPM's TG-51 protocol for clinical reference dosimetry of high-energy photon and electron beams. *Med. Phys.* 26(9):1847-1870.
- ⁷⁸Kerns, J.R., S.F. Kry, N. Sahoo, D.S. Followill, and G.S. Ibbott. 2011. Angular dependence of the nanoDot OSL dosimeter. *Med. Phys.* 38(7):3955-3962.
- ⁷⁹Viamonte, A., L.A.R. da Rosa, L.A. Buckley, A. Cherpak, and J.E. Cygler. 2008. Radiotherapy dosimetry using a commercial OSL system. *Med. Phys.* 35(4):1261-1266.
- ⁸⁰Aguirre, J., P. Alvarez, D. Followill, G. Ibbott, C. Amador, and A. Tailor. 2009. Optically Stimulated Light Dosimetry: Commissioning of An Optically Stimulated Luminescence (OSL) System for Remote Dosimetry Audits, the Radiological Physics Center Experience. AAPM.
- ⁸¹Jursinic, P.A. 2009. Changes in optically stimulated luminescent dosimeter (OSLD) dosimetric characteristics with accumulated dose. *Med. Phys.* 37(1):132-140.

- ⁸²Agyingi, E.O., P.N. Mobit, and G.A. Sandison. 2006. Energy response of an aluminium oxide detector in kilovoltage and megavoltage photon beams: an EGSnrc Monte Carlo simulation study. *Radiat. Prot. Dosim.* 118(1):28-31.
- ⁸³Mohan, R., C. Chui, and L. Lidofsky. 1985. Energy and angular distributions of photons from medical linear accelerators. *Med. Phys.* 12(5):592-597.
- ⁸⁴Sheikh-Bagheri, D., and D.W.O. Rogers. 2002. Monte Carlo calculation of nine megavoltage photon beam spectra using the BEAM code. *Med. Phys.* 29(3):391-402.
- ⁸⁵Brenner, D.J., and H. Hricak. 2010. Radiation Exposure From Medical Imaging. *JAMA: The Journal of the American Medical Association* 304(2):208-209.
- ⁸⁶National Research Council (U.S.) Committee to Assess Health Risks from Exposure to Low Level of Ionizing Radiation, N.R.C. 2006. Health Risks from exposure to low levels of ionizing radiation: BEIR VII Phase 2. National Academies Press.
- ⁸⁷Hall, E.J., and D.J. Brenner. 2008. Cancer risks from diagnostic radiology. *Br J Radiol* 81(965):362-378.
- ⁸⁸Ron, E. 2003. Cancer Risks from Medical Radiation. *Health Physics* 85(1):47-59.
- ⁸⁹Brenner, D.J., and E.J. Hall. 2007. Computed Tomography - An Increasing Source of Radiation Exposure. *New England Journal of Medicine* 357(22):2277-2284.
- ⁹⁰Pearce, M.S., J.A. Salotti, M.P. Little, K. McHugh, C. Lee, K.P. Kim, N.L. Howe, C.M. Ronckers, P. Rajaraman, A.W. Craft, L. Parker, and A. Berrington de González. 2012. Radiation exposure from CT scans in childhood and subsequent risk of leukaemia and brain tumours: a retrospective cohort study. *The Lancet*(0).
- ⁹¹McCollough, C.H., S. Leng, L. Yu, D.D. Cody, J.M. Boone, and M.F. McNitt-Gray. 2011. CT Dose Index and Patient Dose: They Are Not the Same Thing. *Radiology* 259(2):311-316.
- ⁹²Bogdanich, W. 2009. Radiation Overdoses Point Up Dangers of CT Scans. *In The New York Times*. New York, NY.

- ⁹³2009. (The Associated Press) Inquiry Looks at Overdoses of Radiation *In The New York Times*. New York, NY.
- ⁹⁴Bogdanich, W. 2010. After Stroke Scans, Patients Face Serious Health Risks. *In The New York Times*. New York, NY.
- ⁹⁵2010. Senate Bill 1237; Health and Safety Code Section 115113. *In Health and Safety Code*.
- ⁹⁶Bernier, M.O., J.L. Rehel, H.J. Brisse, X. Wu-Zhou, S. Caer-Lorho, S. Jacob, J.F. Chateil, B. Aubert, and D. Laurier. 2012. Radiation exposure from CT in early childhood: a French large-scale multicentre study. *British Journal of Radiology* 85(1009):53-60.
- ⁹⁷AAPM. 2010. Report No. 111: Comprehensive Methodology for the Evaluation of Radiation Dose in X-Ray Computed Tomography. *In Report of the AAPM Task Group 111: The Future of CT Dosimetry*.
- ⁹⁸Aznar, M.C., B. Hemdal, J. Medin, C.J. Marckmann, C.E. Andersen, L. Botter-Jensen, I. Andersson, and S. Mattsson. 2005. In vivo absorbed dose measurements in mammography using a new real-time luminescence technique. *Br J Radiol* 78(928):328-334.
- ⁹⁹Yukihara, E.G., and et al. 2005. High-precision dosimetry for radiotherapy using the optically stimulated luminescence technique and thin Al₂O₃:C dosimeters. *Phys. Med. Biol.* 50(23):5619.
- ¹⁰⁰Mrcela, I., T. Bokulic, J. Izewska, M. Budanec, A. Frobe, and Z. Kusic. 2011. Optically stimulated luminescence in vivo dosimetry for radiotherapy: physical characterization and clinical measurements in 60 Co beams. *Phys. Med. Biol.* 56(18):6065.
- ¹⁰¹Scarboro, S.B., D.S. Followill, J.R. Kerns, R.A. White, and S.F. Kry. 2012. Energy response of optically stimulated luminescent dosimeters for non-reference measurement locations in a 6 MV photon beam. *Phys. Med. Biol.* 57(9):2505.
- ¹⁰²Lavoie, L., M. Ghita, L. Brateman, and M. Arreola. 2011. Characterization of a commercially-available, optically-stimulated luminescent dosimetry system for use in computed tomography. *Health Physics* 101 (3):299-310.

- ¹⁰³Scarboro, S.B., and S.F. Kry. 2012. Characterization of energy response of Al₂O₃:C optically stimulated luminescent dosimeters (OSLD) using cavity theory. *Radiat. Prot. Dosim.*
- ¹⁰⁴June 2010. Radiological Physics Center (RPC), "The RPC has changed to optically stimulated luminescence dosimetry". *In* RPC Newsletter.
- ¹⁰⁵Funama, Y., K. Taguchi, D. Utsunomiya, S. Oda, H. Murasaki, Y. Yamashita, and K. Awai. 2011. Dose profiles for lung and breast regions at prospective and retrospective CT coronary angiography using optically stimulated luminescence dosimeters on a 64-detector CT scanner. *Physica Medica* In Press, Corrected Proof.
- ¹⁰⁶Ruan, C., E.G. Yukihiro, W.J. Clouse, P.B.R. Gasparian, and S. Ahmad. 2010. Determination of multislice computed tomography dose index (CTDI) using optically stimulated luminescence technology. *Med. Phys.* 37(7):3560-3568.
- ¹⁰⁷June 5, 2012. Landauer Irradiation Certificate Report No. 20120605-1236. 2 Science Road, Glenwood, IL 60425.
- ¹⁰⁸Mathieu, K.B., M.F. McNitt-Gray, D. Zhang, H.J. Kim, and D.D. Cody. 2010. Precision of dosimetry-related measurements obtained on current multidetector computed tomography scanners. *Med. Phys.* 37(8):4102-4109.

Appendices

Identification of Photon Spectra

6MV 10cm × 10cm Open Field Spectra

Spectrum ID	Depth in Water (cm)	Distance from Central Axis (cm)	Average Spectral Energy (MeV)
10_13101	0.5	0	1.56
10_13102	1.6	0	1.49
10_13103	3	0	1.45
10_13104	5	0	1.41
10_13105	8	0	1.40
10_13106	10	0	1.39
10_13107	12	0	1.40
10_13108	15	0	1.42
10_13109	20	0	1.46
10_13110	25	0	1.53
10_13201	1.6	5	1.39
10_13202	1.6	10	0.41
10_13203	1.6	15	0.40
10_13204	1.6	20	0.46
10_13205	1.6	25	0.43
10_13206	1.6	30	0.38
10_13207	1.6	40	0.29
10_13208	1.6	50	0.29
10_13501	5	5	1.32
10_13502	5	10	0.35
10_13503	5	15	0.31
10_13504	5	20	0.36
10_13505	5	25	0.35
10_13506	5	30	0.30
10_13507	5	40	0.26
10_13508	5	50	0.25
10_13701	20	5	1.44
10_13702	20	10	0.42
10_13703	20	15	0.31
10_13704	20	20	0.28
10_13705	20	25	0.27
10_13706	20	30	0.26
10_13707	20	40	0.24
10_13708	20	50	0.22

6MV 5cm × 5cm Open Field Spectra

Spectrum ID	Depth in Water (cm)	Distance from Central Axis (cm)	Average Spectral Energy (MeV)
5_13101	0.5	0	1.69
5_13102	1.6	0	1.65
5_13103	3	0	1.64
5_13104	5	0	1.65
5_13105	8	0	1.68
5_13106	10	0	1.70
5_13107	12	0	1.73
5_13108	15	0	1.77
5_13109	20	0	1.85
5_13110	25	0	1.94
5_13201	1.6	5	0.56
5_13202	1.6	10	0.57
5_13203	1.6	15	0.72
5_13204	1.6	20	0.84
5_13205	1.6	25	0.62
5_13206	1.6	30	0.38
5_13207	1.6	40	0.30
5_13208	1.6	50	0.31
5_13501	5	5	0.50
5_13502	5	10	0.45
5_13503	5	15	0.54
5_13504	5	20	0.66
5_13508	5	50	0.26
5_13701	20	5	0.66
5_13703	20	15	0.40
5_13708	20	50	0.23

6MV 20cm × 20cm Open Field Spectra

Spectrum ID	Depth in Water (cm)	Distance from Central Axis (cm)	Average Spectral Energy (MeV)
20_13101	0.5	0	1.38
20_13102	1.6	0	1.29
20_13106	10	0	1.06
20_13109	20	0	1.03
20_13110	25	0	1.08
20_13201	1.6	5	1.28
20_13207	1.6	40	0.21
20_13208	1.6	50	0.26
20_13501	5	5	1.15
20_13503	5	15	0.22
20_13504	5	20	0.20
20_13508	5	50	0.22
20_13701	20	5	1.04
20_13703	20	15	0.32
20_13704	20	20	0.23
20_13706	20	30	0.19
20_13708	20	50	0.17

6MV 10cm × 10cm Open Field Spectra with Lung Heterogeneity

Spectrum ID	Depth in Water (cm)	Distance from Central Axis (cm)	Average Spectral Energy (MeV)
10_13106L	10	0	1.50
10_13107L	12	0	1.44
10_13108L	15	0	1.39
10_13109L	20	0	1.39
10_13110L	25	0	1.45
10_13701L	20	5	1.39
10_13704L	20	20	0.30
10_13708L	20	50	0.24

6MV 10cm × 10cm Open Field Spectra with Bone Heterogeneity

Spectrum ID	Depth in Water (cm)	Distance from Central Axis (cm)	Average Spectral Energy (MeV)
10_13106B	10	0	1.35
10_13107B	12	0	1.39
10_13108B	15	0	1.43
10_13109B	20	0	1.49
10_13110B	25	0	1.56
10_13701B	20	5	1.48
10_13704B	20	20	0.29
10_13708B	20	50	0.22

6MV 10cm × 10cm Modulated Spectra

Spectrum ID	Depth in Water (cm)	Distance from Central Axis (cm)	Average Spectral Energy (MeV)
IMRT_13101	0.5	0	1.74
IMRT_13102	1.6	0	1.68
IMRT_13103	3	0	1.57
IMRT_13104	5	0	1.54
IMRT_13105	8	0	1.52
IMRT_13106	10	0	1.52
IMRT_13107	12	0	1.52
IMRT_13108	15	0	1.54
IMRT_13109	20	0	1.59
IMRT_13110	25	0	1.67
IMRT_13201	1.6	5	1.66
IMRT_13202	1.6	10	0.41
IMRT_13203	1.6	15	0.43
IMRT_13204	1.6	20	0.58
IMRT_13205	1.6	25	0.63
IMRT_13206	1.6	30	0.39
IMRT_13207	1.6	40	0.37
IMRT_13208	1.6	50	0.36
IMRT_13501	5	5	1.47
IMRT_13502	5	10	0.34
IMRT_13503	5	15	0.34
IMRT_13504	5	20	0.41
IMRT_13505	5	25	0.56
IMRT_13506	5	30	0.35
IMRT_13507	5	40	0.32
IMRT_13508	5	50	0.32
IMRT_13701	20	5	1.61
IMRT_13702	20	10	0.42
IMRT_13703	20	15	0.32
IMRT_13704	20	20	0.30
IMRT_13705	20	25	0.40
IMRT_13706	20	30	0.36
IMRT_13707	20	40	0.26
IMRT_13708	20	50	0.26

Photon Energy Spectra Tabular Data
6MV 10cm × 10cm Open Field Spectra

Energy Bin	10_13101	10_13102	10_13103	10_13104	10_13105	10_13106	10_13107	10_13108	10_13109	10_13110	10_13201	10_13202
6.31E-03	5.68E-06	6.94E-06	6.59E-06	6.56E-06	6.37E-06	6.46E-06	6.23E-06	6.55E-06	6.58E-06	7.20E-06	6.26E-06	2.36E-06
8.58E-03	1.67E-05	2.01E-05	1.98E-05	1.95E-05	1.96E-05	1.97E-05	1.89E-05	2.02E-05	1.98E-05	2.05E-05	1.93E-05	7.03E-06
1.17E-02	3.99E-05	5.05E-05	5.20E-05	5.04E-05	4.81E-05	4.87E-05	5.06E-05	4.79E-05	5.03E-05	5.40E-05	4.83E-05	1.83E-05
1.58E-02	8.27E-05	1.34E-04	1.33E-04	1.31E-04	1.28E-04	1.25E-04	1.29E-04	1.30E-04	1.27E-04	1.45E-04	1.19E-04	4.65E-05
2.15E-02	1.65E-04	2.86E-04	3.26E-04	3.41E-04	3.41E-04	3.39E-04	3.47E-04	3.49E-04	3.54E-04	3.78E-04	2.66E-04	1.35E-04
2.93E-02	3.80E-04	6.71E-04	8.24E-04	9.79E-04	1.12E-03	1.19E-03	1.26E-03	1.38E-03	1.51E-03	1.54E-03	6.80E-04	1.70E-03
3.98E-02	1.40E-03	2.16E-03	2.91E-03	3.82E-03	5.08E-03	5.82E-03	6.49E-03	7.44E-03	8.52E-03	8.33E-03	2.90E-03	1.68E-02
5.41E-02	3.92E-03	5.53E-03	7.36E-03	9.73E-03	1.29E-02	1.49E-02	1.66E-02	1.88E-02	2.11E-02	2.07E-02	7.91E-03	5.10E-02
7.36E-02	7.41E-03	1.02E-02	1.31E-02	1.67E-02	2.12E-02	2.38E-02	2.60E-02	2.86E-02	3.12E-02	3.03E-02	1.41E-02	8.47E-02
1.00E-01	1.23E-02	1.66E-02	2.04E-02	2.47E-02	2.94E-02	3.17E-02	3.36E-02	3.58E-02	3.77E-02	3.55E-02	2.16E-02	1.08E-01
1.36E-01	2.08E-02	2.64E-02	3.03E-02	3.44E-02	3.80E-02	3.97E-02	4.11E-02	4.23E-02	4.28E-02	4.08E-02	3.20E-02	1.25E-01
1.85E-01	3.66E-02	4.03E-02	4.25E-02	4.43E-02	4.55E-02	4.58E-02	4.59E-02	4.58E-02	4.51E-02	4.18E-02	4.68E-02	1.40E-01
2.51E-01	5.40E-02	5.62E-02	5.66E-02	5.68E-02	5.60E-02	5.51E-02	5.44E-02	5.32E-02	5.13E-02	4.69E-02	6.23E-02	1.35E-01
3.41E-01	5.93E-02	6.21E-02	6.19E-02	6.11E-02	5.88E-02	5.72E-02	5.56E-02	5.34E-02	5.07E-02	5.00E-02	6.70E-02	1.06E-01
4.64E-01	6.21E-02	6.62E-02	6.75E-02	6.65E-02	6.35E-02	6.13E-02	5.90E-02	5.60E-02	5.21E-02	4.98E-02	7.02E-02	6.43E-02
6.31E-01	7.26E-02	7.63E-02	7.89E-02	7.82E-02	7.53E-02	7.30E-02	7.07E-02	6.75E-02	6.31E-02	6.05E-02	7.98E-02	3.59E-02
8.58E-01	8.28E-02	8.21E-02	8.23E-02	8.20E-02	7.95E-02	7.74E-02	7.53E-02	7.23E-02	6.77E-02	6.50E-02	8.27E-02	2.17E-02
1.17E+00	1.01E-01	9.66E-02	9.20E-02	9.07E-02	8.90E-02	8.76E-02	8.60E-02	8.40E-02	8.04E-02	7.87E-02	9.05E-02	2.17E-02
1.58E+00	1.12E-01	1.05E-01	9.87E-02	9.61E-02	9.50E-02	9.44E-02	9.35E-02	9.25E-02	9.09E-02	9.14E-02	9.57E-02	2.34E-02
2.15E+00	1.09E-01	1.03E-01	1.00E-01	9.70E-02	9.54E-02	9.55E-02	9.58E-02	9.65E-02	9.74E-02	1.00E-01	9.64E-02	2.30E-02
2.93E+00	1.03E-01	9.69E-02	9.64E-02	9.30E-02	9.17E-02	9.20E-02	9.27E-02	9.40E-02	9.77E-02	1.03E-01	8.95E-02	2.10E-02
3.98E+00	8.62E-02	8.15E-02	7.95E-02	7.71E-02	7.62E-02	7.65E-02	7.73E-02	7.95E-02	8.41E-02	9.12E-02	7.41E-02	1.45E-02
5.41E+00	6.23E-02	5.90E-02	5.72E-02	5.57E-02	5.55E-02	5.60E-02	5.69E-02	5.90E-02	6.33E-02	6.95E-02	5.61E-02	5.40E-03
7.36E+00	1.32E-02	1.24E-02	1.08E-02	1.06E-02	1.05E-02	1.07E-02	1.11E-02	1.15E-02	1.27E-02	1.40E-02	9.26E-03	6.10E-04
1.00E+01	0.00E+00	0.00E+00	0.00E+00	0.00E+00	0.00E+00	0.00E+00	0.00E+00	0.00E+00	0.00E+00	0.00E+00	0.00E+00	0.00E+00

6MV 10cm × 10cm Open Field Spectra (Continued)

Energy Bin	10_13203	10_13204	10_13205	10_13206	10_13207	10_13208	10_13501	10_13502	10_13503	10_13504	10_13505	10_13506
6.31E-03	1.84E-06	2.07E-06	2.27E-06	2.03E-06	1.37E-06	1.55E-06	6.07E-06	1.60E-06	1.46E-06	1.62E-06	1.14E-06	1.39E-06
8.58E-03	6.31E-06	6.69E-06	7.89E-06	5.45E-06	4.38E-06	4.43E-06	1.80E-05	4.78E-06	4.87E-06	4.44E-06	4.27E-06	4.19E-06
1.17E-02	1.37E-05	1.83E-05	2.12E-05	1.49E-05	1.04E-05	3.82E-06	4.66E-05	1.13E-05	9.73E-06	1.17E-05	1.20E-05	5.61E-06
1.58E-02	3.83E-05	3.70E-05	4.50E-05	3.94E-05	4.58E-05	2.28E-05	1.21E-04	2.84E-05	2.34E-05	3.26E-05	3.29E-05	2.11E-05
2.15E-02	9.63E-05	1.15E-04	1.54E-04	1.18E-04	7.25E-05	6.81E-05	3.16E-04	1.05E-04	7.00E-05	8.08E-05	7.74E-05	8.31E-05
2.93E-02	2.20E-03	2.59E-03	2.88E-03	3.01E-03	2.96E-03	2.03E-03	1.02E-03	2.21E-03	2.93E-03	3.48E-03	3.89E-03	3.96E-03
3.98E-02	2.59E-02	2.98E-02	3.26E-02	3.23E-02	3.28E-02	2.72E-02	4.89E-03	2.19E-02	3.27E-02	3.95E-02	4.27E-02	4.46E-02
5.41E-02	7.62E-02	8.41E-02	8.76E-02	8.77E-02	8.63E-02	7.50E-02	1.29E-02	6.17E-02	8.99E-02	1.02E-01	1.09E-01	1.11E-01
7.36E-02	1.14E-01	1.20E-01	1.22E-01	1.19E-01	1.20E-01	1.09E-01	2.17E-02	9.69E-02	1.28E-01	1.37E-01	1.40E-01	1.41E-01
1.00E-01	1.30E-01	1.29E-01	1.28E-01	1.22E-01	1.29E-01	1.24E-01	3.04E-02	1.17E-01	1.39E-01	1.40E-01	1.38E-01	1.36E-01
1.36E-01	1.31E-01	1.21E-01	1.15E-01	1.16E-01	1.23E-01	1.31E-01	4.00E-02	1.27E-01	1.33E-01	1.26E-01	1.21E-01	1.18E-01
1.85E-01	1.29E-01	1.16E-01	1.06E-01	9.89E-02	1.09E-01	1.13E-01	4.96E-02	1.28E-01	1.21E-01	1.13E-01	1.03E-01	9.80E-02
2.51E-01	1.16E-01	1.01E-01	9.37E-02	9.08E-02	9.87E-02	9.36E-02	6.13E-02	1.17E-01	1.02E-01	9.00E-02	8.48E-02	8.34E-02
3.41E-01	8.86E-02	7.84E-02	7.52E-02	7.50E-02	8.74E-02	9.10E-02	6.49E-02	9.71E-02	8.16E-02	7.16E-02	6.95E-02	6.82E-02
4.64E-01	4.81E-02	4.35E-02	4.52E-02	5.14E-02	5.64E-02	6.38E-02	6.92E-02	7.21E-02	5.51E-02	4.67E-02	4.62E-02	4.86E-02
6.31E-01	2.19E-02	2.17E-02	2.59E-02	3.41E-02	3.55E-02	5.77E-02	8.04E-02	5.22E-02	3.24E-02	2.42E-02	2.54E-02	3.04E-02
8.58E-01	1.17E-02	1.37E-02	2.17E-02	3.03E-02	2.84E-02	3.69E-02	8.13E-02	2.84E-02	1.24E-02	1.11E-02	1.53E-02	2.33E-02
1.17E+00	1.34E-02	1.84E-02	3.02E-02	3.90E-02	3.51E-02	3.57E-02	8.67E-02	1.86E-02	1.13E-02	1.32E-02	1.88E-02	2.69E-02
1.58E+00	1.73E-02	2.53E-02	3.50E-02	4.62E-02	2.96E-02	2.75E-02	9.00E-02	1.63E-02	1.15E-02	1.71E-02	2.26E-02	3.09E-02
2.15E+00	2.36E-02	3.32E-02	3.53E-02	3.44E-02	1.82E-02	8.00E-03	8.99E-02	1.57E-02	1.49E-02	2.14E-02	2.36E-02	2.21E-02
2.93E+00	2.47E-02	3.03E-02	2.64E-02	1.63E-02	5.02E-03	3.60E-03	8.31E-02	1.40E-02	1.52E-02	2.04E-02	2.07E-02	1.17E-02
3.98E+00	1.70E-02	2.04E-02	1.11E-02	3.01E-03	1.23E-03	6.91E-04	7.00E-02	9.86E-03	1.04E-02	1.44E-02	9.87E-03	2.19E-03
5.41E+00	7.60E-03	9.63E-03	5.30E-03	5.95E-04	1.73E-04	0.00E+00	5.32E-02	3.64E-03	4.81E-03	6.79E-03	4.58E-03	5.52E-04
7.36E+00	1.07E-03	1.28E-03	7.19E-04	0.00E+00	0.00E+00	0.00E+00	8.85E-03	4.09E-04	6.26E-04	8.92E-04	6.57E-04	0.00E+00
1.00E+01	0.00E+00	0.00E+00	0.00E+00	0.00E+00	0.00E+00	0.00E+00	0.00E+00	0.00E+00	0.00E+00	0.00E+00	0.00E+00	0.00E+00

6MV 10cm × 10cm Open Field Spectra (Continued)

Energy Bin	10_13507	10_13508	10_13701	10_13702	10_13703	10_13704	10_13705	10_13706	10_13707	10_13801	10_13802	10_13803
6.31E-03	1.84E-06	8.87E-07	6.58E-06	2.00E-06	1.37E-06	1.17E-06	9.36E-07	1.81E-06	1.26E-06	1.27E-06	1.32E-06	5.49E-06
8.58E-03	3.53E-06	2.10E-06	1.96E-05	5.45E-06	3.92E-06	4.30E-06	3.87E-06	4.40E-06	2.71E-06	3.61E-06	3.81E-06	9.24E-06
1.17E-02	1.01E-05	8.89E-06	4.80E-05	1.41E-05	9.05E-06	8.47E-06	8.24E-06	4.60E-06	5.00E-06	8.77E-06	8.14E-06	1.16E-04
1.58E-02	2.34E-05	2.15E-05	1.31E-04	3.32E-05	2.46E-05	1.82E-05	1.34E-05	1.32E-05	5.12E-06	2.20E-05	2.28E-05	3.81E-05
2.15E-02	8.87E-05	4.69E-05	3.31E-04	1.31E-04	7.72E-05	6.66E-05	7.25E-05	7.87E-05	3.90E-05	6.85E-05	6.13E-05	9.90E-05
2.93E-02	4.10E-03	2.89E-03	1.50E-03	2.81E-03	3.47E-03	4.33E-03	4.73E-03	5.06E-03	5.74E-03	2.13E-04	1.95E-04	1.49E-03
3.98E-02	4.38E-02	3.87E-02	9.36E-03	2.74E-02	3.71E-02	4.58E-02	5.09E-02	5.52E-02	5.78E-02	9.74E-04	9.33E-04	2.13E-02
5.41E-02	1.10E-01	9.91E-02	2.33E-02	7.07E-02	9.45E-02	1.12E-01	1.23E-01	1.31E-01	1.37E-01	2.95E-03	2.80E-03	6.77E-02
7.36E-02	1.41E-01	1.33E-01	3.37E-02	9.87E-02	1.27E-01	1.41E-01	1.52E-01	1.56E-01	1.57E-01	5.72E-03	5.39E-03	9.68E-02
1.00E-01	1.42E-01	1.37E-01	3.96E-02	1.07E-01	1.33E-01	1.37E-01	1.40E-01	1.40E-01	1.35E-01	9.49E-03	8.83E-03	1.06E-01
1.36E-01	1.19E-01	1.25E-01	4.34E-02	1.06E-01	1.18E-01	1.21E-01	1.18E-01	1.17E-01	1.11E-01	1.67E-02	1.59E-02	1.03E-01
1.85E-01	1.00E-01	1.10E-01	4.49E-02	9.62E-02	9.99E-02	9.77E-02	9.47E-02	9.18E-02	9.93E-02	3.32E-02	3.07E-02	1.10E-01
2.51E-01	8.57E-02	8.70E-02	5.04E-02	8.97E-02	8.31E-02	8.25E-02	7.82E-02	7.49E-02	6.74E-02	5.11E-02	4.87E-02	1.02E-01
3.41E-01	7.59E-02	7.25E-02	5.00E-02	7.83E-02	7.22E-02	6.68E-02	6.40E-02	6.24E-02	5.82E-02	5.53E-02	5.49E-02	8.17E-02
4.64E-01	5.09E-02	5.93E-02	5.20E-02	6.97E-02	6.28E-02	5.74E-02	5.23E-02	5.08E-02	5.04E-02	5.80E-02	6.04E-02	5.26E-02
6.31E-01	3.31E-02	4.37E-02	6.38E-02	6.60E-02	5.40E-02	4.59E-02	4.14E-02	3.85E-02	3.67E-02	7.13E-02	7.76E-02	3.68E-02
8.58E-01	2.41E-02	3.05E-02	6.84E-02	5.47E-02	4.06E-02	3.05E-02	2.45E-02	2.29E-02	2.42E-02	8.49E-02	8.78E-02	3.80E-02
1.17E+00	2.56E-02	2.80E-02	7.92E-02	4.61E-02	2.94E-02	1.87E-02	1.36E-02	1.34E-02	1.96E-02	1.02E-01	1.04E-01	4.89E-02
1.58E+00	2.42E-02	2.17E-02	8.92E-02	3.59E-02	1.83E-02	1.06E-02	9.74E-03	1.22E-02	1.85E-02	1.12E-01	1.11E-01	6.31E-02
2.15E+00	1.52E-02	7.91E-03	9.57E-02	2.49E-02	1.12E-02	9.19E-03	1.14E-02	1.19E-02	1.48E-02	1.15E-01	1.13E-01	4.70E-02
2.93E+00	4.19E-03	2.24E-03	9.38E-02	1.54E-02	8.06E-03	9.22E-03	1.01E-02	1.02E-02	5.77E-03	1.11E-01	1.08E-01	1.87E-02
3.98E+00	1.00E-03	5.71E-04	8.50E-02	7.71E-03	4.95E-03	6.85E-03	7.28E-03	4.29E-03	1.19E-03	9.16E-02	9.15E-02	3.65E-03
5.41E+00	2.64E-05	0.00E+00	6.52E-02	2.56E-03	2.28E-03	3.40E-03	3.34E-03	1.80E-03	1.93E-04	6.57E-02	6.68E-02	6.87E-04
7.36E+00	0.00E+00	0.00E+00	1.10E-02	2.46E-04	2.76E-04	5.12E-04	5.11E-04	3.52E-04	0.00E+00	1.24E-02	1.15E-02	0.00E+00
1.00E+01	0.00E+00	0.00E+00	0.00E+00	0.00E+00	0.00E+00	0.00E+00	0.00E+00	0.00E+00	0.00E+00	0.00E+00	0.00E+00	0.00E+00

6MV 10cm × 10cm Open Field Spectra (Continued)

Energy Bin	10_13901	10_13902
6.31E-03	6.68E-06	6.83E-06
8.58E-03	2.01E-05	2.00E-05
1.17E-02	5.02E-05	5.12E-05
1.58E-02	1.24E-04	1.33E-04
2.15E-02	2.78E-04	3.57E-04
2.93E-02	5.80E-04	1.49E-03
3.98E-02	2.01E-03	8.51E-03
5.41E-02	5.26E-03	2.14E-02
7.36E-02	9.47E-03	3.13E-02
1.00E-01	1.51E-02	3.71E-02
1.36E-01	2.38E-02	4.18E-02
1.85E-01	3.70E-02	4.38E-02
2.51E-01	5.28E-02	4.94E-02
3.41E-01	6.07E-02	4.96E-02
4.64E-01	6.84E-02	5.19E-02
6.31E-01	7.98E-02	6.34E-02
8.58E-01	8.58E-02	6.84E-02
1.17E+00	9.77E-02	8.13E-02
1.58E+00	1.04E-01	9.19E-02
2.15E+00	1.04E-01	9.76E-02
2.93E+00	9.81E-02	9.83E-02
3.98E+00	8.32E-02	8.49E-02
5.41E+00	6.02E-02	6.51E-02
7.36E+00	1.09E-02	1.22E-02
1.00E+01	0.00E+00	0.00E+00

6MV 5cm × 5cm Open Field Spectra

Energy Bin	5_13101	5_13102	5_13103	5_13104	5_13105	5_13106	5_13107	5_13108	5_13109	5_13110	5_13201	5_13202
6.31E-03	5.56E-06	7.71E-06	7.33E-06	7.83E-06	7.55E-06	7.42E-06	8.15E-06	7.55E-06	8.64E-06	8.39E-06	2.54E-06	3.36E-06
8.58E-03	1.74E-05	2.25E-05	2.22E-05	2.26E-05	2.27E-05	2.42E-05	2.43E-05	2.28E-05	2.83E-05	2.63E-05	8.54E-06	5.89E-06
1.17E-02	3.77E-05	6.05E-05	5.81E-05	5.88E-05	6.13E-05	5.84E-05	6.20E-05	6.04E-05	6.08E-05	6.30E-05	1.82E-05	1.34E-05
1.58E-02	8.48E-05	1.39E-04	1.47E-04	1.49E-04	1.62E-04	1.58E-04	1.53E-04	1.71E-04	1.69E-04	1.76E-04	6.59E-05	6.55E-05
2.15E-02	1.62E-04	2.89E-04	3.40E-04	3.60E-04	3.79E-04	3.80E-04	3.94E-04	4.07E-04	4.34E-04	4.63E-04	2.92E-04	1.54E-04
2.93E-02	2.65E-04	5.05E-04	6.34E-04	7.56E-04	8.51E-04	8.97E-04	9.34E-04	1.00E-03	1.07E-03	1.16E-03	1.60E-03	1.73E-03
3.98E-02	5.71E-04	9.92E-04	1.36E-03	1.81E-03	2.36E-03	2.67E-03	2.94E-03	3.41E-03	3.92E-03	3.99E-03	9.20E-03	1.67E-02
5.41E-02	1.32E-03	2.03E-03	2.80E-03	3.75E-03	5.12E-03	5.91E-03	6.65E-03	7.62E-03	8.76E-03	8.71E-03	2.72E-02	5.17E-02
7.36E-02	2.52E-03	3.74E-03	4.90E-03	6.43E-03	8.36E-03	9.39E-03	1.03E-02	1.18E-02	1.30E-02	1.30E-02	4.94E-02	8.32E-02
1.00E-01	4.62E-03	6.60E-03	8.33E-03	1.03E-02	1.24E-02	1.35E-02	1.44E-02	1.54E-02	1.67E-02	1.55E-02	7.43E-02	1.06E-01
1.36E-01	9.59E-03	1.26E-02	1.46E-02	1.65E-02	1.82E-02	1.91E-02	1.98E-02	2.04E-02	2.08E-02	1.96E-02	1.03E-01	1.18E-01
1.85E-01	2.10E-02	2.30E-02	2.41E-02	2.47E-02	2.51E-02	2.53E-02	2.52E-02	2.51E-02	2.49E-02	2.28E-02	1.34E-01	1.28E-01
2.51E-01	3.87E-02	4.01E-02	4.00E-02	3.93E-02	3.83E-02	3.74E-02	3.66E-02	3.55E-02	3.38E-02	3.07E-02	1.45E-01	1.22E-01
3.41E-01	4.94E-02	5.08E-02	4.97E-02	4.79E-02	4.49E-02	4.30E-02	4.13E-02	3.91E-02	3.65E-02	3.45E-02	1.20E-01	9.59E-02
4.64E-01	6.26E-02	6.47E-02	6.33E-02	6.07E-02	5.62E-02	5.32E-02	5.06E-02	4.70E-02	4.21E-02	3.83E-02	8.18E-02	5.64E-02
6.31E-01	7.73E-02	8.03E-02	7.95E-02	7.73E-02	7.31E-02	7.04E-02	6.76E-02	6.34E-02	5.77E-02	5.39E-02	5.94E-02	3.56E-02
8.58E-01	9.02E-02	9.15E-02	9.00E-02	8.82E-02	8.42E-02	8.13E-02	7.86E-02	7.47E-02	6.90E-02	6.34E-02	3.04E-02	1.83E-02
1.17E+00	1.11E-01	1.09E-01	1.07E-01	1.06E-01	1.03E-01	1.02E-01	9.95E-02	9.62E-02	9.07E-02	8.68E-02	2.87E-02	1.77E-02
1.58E+00	1.21E-01	1.17E-01	1.17E-01	1.17E-01	1.16E-01	1.16E-01	1.15E-01	1.14E-01	1.11E-01	1.10E-01	3.29E-02	3.08E-02
2.15E+00	1.19E-01	1.15E-01	1.14E-01	1.14E-01	1.17E-01	1.18E-01	1.19E-01	1.20E-01	1.21E-01	1.24E-01	4.03E-02	3.42E-02
2.93E+00	1.13E-01	1.10E-01	1.11E-01	1.12E-01	1.15E-01	1.17E-01	1.19E-01	1.23E-01	1.28E-01	1.33E-01	2.91E-02	3.66E-02
3.98E+00	9.33E-02	9.05E-02	9.04E-02	9.16E-02	9.52E-02	9.77E-02	1.01E-01	1.06E-01	1.13E-01	1.22E-01	2.16E-02	2.88E-02
5.41E+00	6.81E-02	6.63E-02	6.66E-02	6.74E-02	6.99E-02	7.21E-02	7.45E-02	7.90E-02	8.74E-02	9.75E-02	1.15E-02	1.55E-02
7.36E+00	1.54E-02	1.49E-02	1.37E-02	1.41E-02	1.45E-02	1.52E-02	1.59E-02	1.71E-02	1.91E-02	2.14E-02	1.07E-03	2.10E-03
1.00E+01	0.00E+00	0.00E+00	0.00E+00	0.00E+00	0.00E+00	0.00E+00	0.00E+00	0.00E+00	0.00E+00	0.00E+00	0.00E+00	0.00E+00

6MV 5cm × 5cm Open Field Spectra (Continued)

Energy Bin	5_13203	5_13204	5_13205	5_13206	5_13207	5_13208	5_13501	5_13502	5_13503	5_13504	5_13508	5_13701
6.31E-03	3.05E-06	3.09E-06	2.85E-06	3.90E-06	2.24E-06	1.88E-06	3.03E-06	1.75E-06	3.14E-06	3.55E-06	2.25E-06	2.81E-06
8.58E-03	9.66E-06	1.43E-05	1.24E-05	1.13E-05	9.61E-06	1.03E-05	6.85E-06	4.48E-06	6.42E-06	7.97E-06	2.35E-06	9.05E-06
1.17E-02	2.00E-05	3.81E-05	2.25E-05	1.80E-05	1.24E-06	0.00E+00	1.79E-05	2.02E-05	1.85E-05	2.57E-05	1.89E-05	2.38E-05
1.58E-02	7.34E-05	6.64E-05	4.45E-05	2.56E-05	3.52E-05	3.75E-05	5.64E-05	2.96E-05	3.81E-05	6.29E-05	8.62E-06	6.55E-05
2.15E-02	1.33E-04	1.43E-04	1.55E-04	9.23E-05	1.12E-04	4.10E-05	2.80E-04	1.25E-04	1.30E-04	1.82E-04	2.44E-05	2.36E-04
2.93E-02	1.91E-03	2.00E-03	2.12E-03	1.99E-03	1.44E-03	1.53E-03	1.99E-03	2.06E-03	2.72E-03	2.87E-03	2.31E-03	2.34E-03
3.98E-02	2.24E-02	2.30E-02	2.63E-02	2.87E-02	2.23E-02	1.89E-02	1.23E-02	2.27E-02	3.08E-02	3.37E-02	3.04E-02	1.67E-02
5.41E-02	6.54E-02	6.43E-02	7.33E-02	7.71E-02	6.94E-02	5.38E-02	3.39E-02	6.38E-02	8.21E-02	8.71E-02	8.16E-02	4.34E-02
7.36E-02	9.83E-02	9.33E-02	1.01E-01	1.09E-01	1.01E-01	8.21E-02	5.76E-02	9.92E-02	1.18E-01	1.16E-01	1.18E-01	6.40E-02
1.00E-01	1.12E-01	1.03E-01	1.13E-01	1.20E-01	1.26E-01	1.07E-01	8.03E-02	1.18E-01	1.27E-01	1.18E-01	1.30E-01	7.59E-02
1.36E-01	1.13E-01	1.01E-01	1.08E-01	1.19E-01	1.24E-01	1.20E-01	1.02E-01	1.24E-01	1.19E-01	1.07E-01	1.29E-01	8.47E-02
1.85E-01	1.09E-01	9.69E-02	1.04E-01	1.16E-01	1.18E-01	1.15E-01	1.16E-01	1.21E-01	1.08E-01	9.48E-02	1.22E-01	8.29E-02
2.51E-01	9.71E-02	8.58E-02	8.89E-02	9.84E-02	1.17E-01	9.64E-02	1.21E-01	1.09E-01	9.07E-02	7.95E-02	9.46E-02	8.70E-02
3.41E-01	7.82E-02	6.75E-02	7.48E-02	8.24E-02	8.78E-02	1.13E-01	1.07E-01	8.99E-02	7.55E-02	6.36E-02	9.74E-02	7.95E-02
4.64E-01	4.39E-02	4.03E-02	5.22E-02	5.08E-02	7.26E-02	6.42E-02	8.91E-02	6.60E-02	5.12E-02	4.34E-02	6.37E-02	7.20E-02
6.31E-01	2.36E-02	2.19E-02	2.92E-02	4.08E-02	4.58E-02	1.31E-01	7.95E-02	4.67E-02	3.14E-02	2.70E-02	4.24E-02	7.70E-02
8.58E-01	1.27E-02	1.65E-02	2.15E-02	3.20E-02	3.80E-02	3.47E-02	5.49E-02	2.30E-02	1.21E-02	1.50E-02	3.18E-02	6.82E-02
1.17E+00	1.59E-02	2.41E-02	2.67E-02	3.27E-02	3.39E-02	3.01E-02	4.01E-02	1.53E-02	1.29E-02	2.05E-02	2.93E-02	6.79E-02
1.58E+00	3.05E-02	4.19E-02	4.19E-02	3.42E-02	2.32E-02	2.50E-02	3.07E-02	2.09E-02	2.03E-02	2.93E-02	1.92E-02	6.06E-02
2.15E+00	4.82E-02	6.20E-02	4.53E-02	3.62E-02	1.38E-02	3.62E-03	2.97E-02	2.30E-02	3.13E-02	4.62E-02	5.65E-03	5.19E-02
2.93E+00	5.48E-02	7.13E-02	4.46E-02	1.64E-02	4.79E-03	3.45E-03	2.00E-02	2.42E-02	3.65E-02	5.24E-02	1.97E-03	3.58E-02
3.98E+00	4.66E-02	5.38E-02	2.94E-02	4.01E-03	8.61E-04	4.41E-04	1.48E-02	1.94E-02	3.14E-02	4.00E-02	1.01E-03	2.14E-02
5.41E+00	2.43E-02	2.75E-02	1.48E-02	1.23E-03	5.15E-05	0.00E+00	8.01E-03	1.05E-02	1.68E-02	2.13E-02	0.00E+00	7.99E-03
7.36E+00	2.82E-03	3.58E-03	2.74E-03	0.00E+00	0.00E+00	0.00E+00	6.94E-04	1.29E-03	2.14E-03	1.66E-03	0.00E+00	6.28E-04
1.00E+01	0.00E+00	0.00E+00	0.00E+00	0.00E+00	0.00E+00	0.00E+00	0.00E+00	0.00E+00	0.00E+00	0.00E+00	0.00E+00	0.00E+00

6MV 5cm × 5cm Open Field Spectra (Continued)

Energy Bin	5_13703	5_13708
6.31E-03	2.81E-06	8.52E-07
8.58E-03	4.91E-06	4.38E-06
1.17E-02	1.19E-05	6.05E-06
1.58E-02	3.33E-05	8.98E-06
2.15E-02	9.98E-05	4.38E-04
2.93E-02	3.28E-03	3.88E-03
3.98E-02	3.61E-02	5.66E-02
5.41E-02	9.51E-02	1.25E-01
7.36E-02	1.23E-01	1.47E-01
1.00E-01	1.26E-01	1.54E-01
1.36E-01	1.10E-01	1.11E-01
1.85E-01	9.48E-02	9.48E-02
2.51E-01	7.86E-02	8.40E-02
3.41E-01	7.78E-02	6.31E-02
4.64E-01	6.13E-02	5.00E-02
6.31E-01	5.39E-02	3.71E-02
8.58E-01	3.88E-02	2.22E-02
1.17E+00	2.79E-02	2.07E-02
1.58E+00	1.89E-02	1.63E-02
2.15E+00	1.52E-02	1.13E-02
2.93E+00	1.63E-02	3.07E-03
3.98E+00	1.36E-02	4.18E-04
5.41E+00	8.74E-03	0.00E+00
7.36E+00	1.10E-03	0.00E+00
1.00E+01	0.00E+00	0.00E+00

6MV 20cm × 20cm Open Field Spectra

Energy Bin	20_13101	20_13102	20_13106	20_13109	20_13110	20_13201	20_13207	20_13208	20_13501	20_13503	20_13504	20_13508
6.31E-03	5.12E-06	6.02E-06	4.87E-06	4.71E-06	4.63E-06	5.75E-06	5.61E-07	1.03E-06	5.27E-06	9.79E-07	8.28E-07	1.56E-06
8.58E-03	1.56E-05	1.69E-05	1.47E-05	1.43E-05	1.43E-05	1.76E-05	2.21E-06	2.87E-06	1.58E-05	3.03E-06	2.20E-06	4.21E-06
1.17E-02	3.71E-05	4.49E-05	3.67E-05	3.64E-05	3.71E-05	4.40E-05	8.71E-06	8.56E-06	4.03E-05	6.11E-06	5.59E-06	4.71E-06
1.58E-02	7.32E-05	1.12E-04	9.53E-05	9.41E-05	9.63E-05	1.09E-04	1.98E-05	2.55E-05	1.05E-04	1.55E-05	1.26E-05	1.17E-05
2.15E-02	1.54E-04	2.49E-04	2.63E-04	2.50E-04	2.67E-04	2.48E-04	6.70E-05	6.31E-05	2.79E-04	6.25E-05	4.38E-05	6.84E-05
2.93E-02	5.32E-04	8.35E-04	1.64E-03	2.05E-03	2.01E-03	7.84E-04	3.65E-03	2.91E-03	1.22E-03	2.78E-03	3.53E-03	4.53E-03
3.98E-02	3.44E-03	4.96E-03	1.24E-02	1.70E-02	1.64E-02	4.49E-03	4.33E-02	3.56E-02	7.86E-03	3.06E-02	4.01E-02	4.92E-02
5.41E-02	1.06E-02	1.44E-02	3.34E-02	4.39E-02	4.25E-02	1.29E-02	1.14E-01	9.52E-02	2.17E-02	8.46E-02	1.08E-01	1.24E-01
7.36E-02	1.88E-02	2.47E-02	5.06E-02	6.22E-02	5.99E-02	2.23E-02	1.50E-01	1.28E-01	3.51E-02	1.24E-01	1.47E-01	1.50E-01
1.00E-01	2.71E-02	3.47E-02	6.10E-02	6.88E-02	6.60E-02	3.14E-02	1.46E-01	1.30E-01	4.59E-02	1.40E-01	1.52E-01	1.41E-01
1.36E-01	3.76E-02	4.59E-02	6.70E-02	7.07E-02	6.82E-02	4.26E-02	1.28E-01	1.24E-01	5.56E-02	1.41E-01	1.40E-01	1.19E-01
1.85E-01	5.50E-02	6.01E-02	6.82E-02	6.64E-02	6.36E-02	5.76E-02	1.05E-01	1.08E-01	6.37E-02	1.32E-01	1.22E-01	1.01E-01
2.51E-01	6.93E-02	7.12E-02	7.05E-02	6.57E-02	6.22E-02	7.01E-02	8.91E-02	8.35E-02	7.10E-02	1.13E-01	9.87E-02	7.80E-02
3.41E-01	6.58E-02	6.85E-02	6.66E-02	6.15E-02	6.05E-02	7.08E-02	7.45E-02	7.14E-02	7.05E-02	8.96E-02	7.69E-02	6.38E-02
4.64E-01	5.96E-02	6.40E-02	6.38E-02	5.80E-02	5.78E-02	6.92E-02	5.02E-02	5.76E-02	6.97E-02	6.04E-02	4.86E-02	5.25E-02
6.31E-01	6.55E-02	6.76E-02	6.78E-02	6.24E-02	6.25E-02	7.44E-02	3.29E-02	5.92E-02	7.46E-02	3.85E-02	2.58E-02	4.33E-02
8.58E-01	7.37E-02	7.10E-02	6.46E-02	6.02E-02	6.04E-02	7.57E-02	2.31E-02	4.26E-02	7.16E-02	1.58E-02	9.25E-03	2.96E-02
1.17E+00	8.83E-02	8.21E-02	6.71E-02	6.39E-02	6.49E-02	8.35E-02	2.09E-02	3.55E-02	7.53E-02	8.93E-03	7.61E-03	2.43E-02
1.58E+00	9.79E-02	8.99E-02	6.90E-02	6.59E-02	6.82E-02	8.77E-02	1.06E-02	1.86E-02	7.71E-02	6.58E-03	8.05E-03	1.25E-02
2.15E+00	9.53E-02	8.75E-02	6.87E-02	6.61E-02	6.91E-02	8.93E-02	4.82E-03	5.35E-03	7.76E-02	5.71E-03	6.79E-03	4.78E-03
2.93E+00	9.05E-02	8.29E-02	6.57E-02	6.34E-02	6.66E-02	8.27E-02	2.46E-03	1.73E-03	7.18E-02	3.87E-03	3.99E-03	1.42E-03
3.98E+00	7.53E-02	6.93E-02	5.46E-02	5.38E-02	5.75E-02	6.64E-02	8.75E-04	2.68E-04	5.82E-02	1.55E-03	1.30E-03	3.79E-04
5.41E+00	5.38E-02	4.95E-02	3.94E-02	3.98E-02	4.28E-02	4.88E-02	8.70E-05	0.00E+00	4.32E-02	3.35E-04	4.84E-04	0.00E+00
7.36E+00	1.14E-02	1.04E-02	7.50E-03	8.00E-03	8.68E-03	8.91E-03	0.00E+00	0.00E+00	7.93E-03	1.07E-05	7.89E-05	0.00E+00
1.00E+01	0.00E+00	0.00E+00	0.00E+00	0.00E+00	0.00E+00	0.00E+00	0.00E+00	0.00E+00	0.00E+00	0.00E+00	0.00E+00	0.00E+00

6MV 20cm × 20cm Open Field Spectra (Continued)

Energy Bin	20_13701	20_13703	20_13704	20_13706	20_13708
6.31E-03	4.69E-06	1.56E-06	9.47E-07	7.05E-07	2.58E-07
8.58E-03	1.45E-05	4.15E-06	3.04E-06	2.67E-06	1.37E-06
1.17E-02	3.64E-05	1.18E-05	7.51E-06	5.41E-06	4.35E-06
1.58E-02	9.43E-05	2.72E-05	2.02E-05	1.36E-05	1.16E-05
2.15E-02	2.51E-04	9.54E-05	6.45E-05	4.44E-05	5.34E-05
2.93E-02	2.00E-03	3.24E-03	4.07E-03	5.38E-03	6.05E-03
3.98E-02	1.66E-02	3.37E-02	4.41E-02	5.78E-02	6.62E-02
5.41E-02	4.30E-02	8.72E-02	1.12E-01	1.40E-01	1.52E-01
7.36E-02	6.04E-02	1.19E-01	1.45E-01	1.64E-01	1.71E-01
1.00E-01	6.70E-02	1.26E-01	1.41E-01	1.50E-01	1.53E-01
1.36E-01	6.89E-02	1.24E-01	1.24E-01	1.21E-01	1.26E-01
1.85E-01	6.53E-02	9.76E-02	9.79E-02	9.54E-02	8.70E-02
2.51E-01	6.48E-02	8.53E-02	8.06E-02	7.59E-02	7.00E-02
3.41E-01	6.08E-02	7.37E-02	7.05E-02	6.14E-02	5.55E-02
4.64E-01	5.80E-02	6.38E-02	5.85E-02	5.04E-02	4.71E-02
6.31E-01	6.33E-02	5.74E-02	4.75E-02	3.66E-02	3.31E-02
8.58E-01	6.17E-02	4.39E-02	3.32E-02	2.04E-02	1.56E-02
1.17E+00	6.51E-02	3.39E-02	2.15E-02	9.84E-03	9.35E-03
1.58E+00	6.71E-02	2.41E-02	1.19E-02	4.89E-03	4.79E-03
2.15E+00	6.79E-02	1.50E-02	5.66E-03	3.29E-03	2.49E-03
2.93E+00	6.41E-02	8.32E-03	2.30E-03	1.88E-03	1.22E-03
3.98E+00	5.54E-02	3.41E-03	6.80E-04	9.49E-04	4.13E-04
5.41E+00	4.11E-02	6.27E-04	1.59E-04	4.00E-04	3.90E-05
7.36E+00	7.08E-03	6.87E-06	1.00E-05	7.94E-05	0.00E+00
1.00E+01	0.00E+00	0.00E+00	0.00E+00	0.00E+00	0.00E+00

6MV 10cm × 10cm Open Field Spectra with Lung Heterogeneity

Energy Bin	10_13106L	10_13107L	10_13108L	10_13109L	10_13110L	10_13701L	10_13704L	10_13708L
6.31E-03	6.68E-06	6.61E-06	6.41E-06	6.26E-06	6.63E-06	6.41E-06	1.41E-06	5.76E-07
8.58E-03	2.06E-05	1.99E-05	1.99E-05	1.83E-05	1.93E-05	1.97E-05	3.81E-06	1.67E-06
1.17E-02	5.27E-05	5.00E-05	5.13E-05	4.94E-05	5.07E-05	4.97E-05	7.45E-06	3.73E-06
1.58E-02	1.38E-04	1.34E-04	1.30E-04	1.22E-04	1.35E-04	1.22E-04	1.96E-05	1.08E-05
2.15E-02	3.50E-04	3.62E-04	3.51E-04	3.53E-04	3.64E-04	3.22E-04	8.86E-05	6.43E-05
2.93E-02	8.57E-04	1.03E-03	1.16E-03	1.32E-03	1.40E-03	1.32E-03	3.73E-03	4.19E-03
3.98E-02	2.88E-03	3.93E-03	5.18E-03	6.66E-03	7.09E-03	7.13E-03	4.07E-02	4.66E-02
5.41E-02	7.34E-03	1.00E-02	1.34E-02	1.71E-02	1.77E-02	1.88E-02	1.03E-01	1.21E-01
7.36E-02	1.30E-02	1.74E-02	2.24E-02	2.74E-02	2.80E-02	2.96E-02	1.38E-01	1.49E-01
1.00E-01	2.02E-02	2.60E-02	3.16E-02	3.65E-02	3.69E-02	3.73E-02	1.40E-01	1.45E-01
1.36E-01	3.00E-02	3.62E-02	4.11E-02	4.41E-02	4.23E-02	4.41E-02	1.24E-01	1.22E-01
1.85E-01	4.34E-02	4.71E-02	4.89E-02	4.90E-02	4.60E-02	4.77E-02	1.05E-01	9.35E-02
2.51E-01	5.70E-02	5.86E-02	5.85E-02	5.64E-02	5.14E-02	5.44E-02	8.37E-02	7.80E-02
3.41E-01	5.97E-02	6.10E-02	5.97E-02	5.71E-02	5.51E-02	5.55E-02	7.32E-02	6.81E-02
4.64E-01	6.19E-02	6.38E-02	6.24E-02	5.85E-02	5.60E-02	5.80E-02	5.95E-02	5.06E-02
6.31E-01	7.14E-02	7.37E-02	7.27E-02	6.91E-02	6.64E-02	6.96E-02	4.40E-02	3.92E-02
8.58E-01	7.75E-02	7.65E-02	7.58E-02	7.22E-02	6.99E-02	7.26E-02	2.39E-02	2.61E-02
1.17E+00	9.09E-02	8.66E-02	8.49E-02	8.25E-02	8.13E-02	8.14E-02	1.36E-02	2.49E-02
1.58E+00	1.01E-01	9.49E-02	9.13E-02	8.97E-02	9.09E-02	8.84E-02	1.04E-02	1.66E-02
2.15E+00	1.03E-01	9.75E-02	9.36E-02	9.29E-02	9.60E-02	9.30E-02	1.14E-02	1.12E-02
2.93E+00	1.01E-01	9.53E-02	9.10E-02	9.11E-02	9.52E-02	8.98E-02	1.18E-02	2.96E-03
3.98E+00	8.45E-02	7.99E-02	7.74E-02	7.79E-02	8.28E-02	8.03E-02	8.86E-03	8.39E-04
5.41E+00	6.15E-02	5.86E-02	5.73E-02	5.84E-02	6.24E-02	6.04E-02	4.34E-03	1.05E-04
7.36E+00	1.16E-02	1.13E-02	1.11E-02	1.17E-02	1.27E-02	1.01E-02	7.15E-04	0.00E+00
1.00E+01	0.00E+00	0.00E+00	0.00E+00	0.00E+00	0.00E+00	0.00E+00	0.00E+00	0.00E+00

6MV 10cm × 10cm Open Field Spectra with Bone Heterogeneity

Energy Bin	10_13106B	10_13107B	10_13108B	10_13109B	10_13110B	10_13701B	10_13704B	10_13708B
6.31E-03	6.25E-06	6.61E-06	6.25E-06	7.15E-06	7.22E-06	6.64E-06	1.24E-06	4.47E-07
8.58E-03	1.90E-05	1.98E-05	1.93E-05	2.02E-05	2.28E-05	2.00E-05	3.09E-06	1.02E-05
1.17E-02	4.83E-05	5.03E-05	4.98E-05	5.23E-05	5.22E-05	5.15E-05	1.10E-05	5.08E-06
1.58E-02	1.11E-04	1.25E-04	1.28E-04	1.30E-04	1.40E-04	1.28E-04	2.50E-05	1.35E-05
2.15E-02	2.48E-04	3.14E-04	3.42E-04	3.71E-04	3.71E-04	3.34E-04	8.47E-05	2.32E-05
2.93E-02	6.79E-04	9.64E-04	1.25E-03	1.52E-03	1.59E-03	1.50E-03	3.52E-03	4.87E-03
3.98E-02	3.42E-03	5.11E-03	7.13E-03	9.07E-03	9.38E-03	9.71E-03	4.14E-02	5.37E-02
5.41E-02	1.24E-02	1.59E-02	2.00E-02	2.40E-02	2.48E-02	2.54E-02	1.07E-01	1.21E-01
7.36E-02	2.64E-02	2.94E-02	3.24E-02	3.60E-02	3.79E-02	3.71E-02	1.39E-01	1.50E-01
1.00E-01	3.90E-02	3.96E-02	4.03E-02	4.20E-02	4.21E-02	4.17E-02	1.37E-01	1.51E-01
1.36E-01	4.77E-02	4.61E-02	4.45E-02	4.30E-02	3.97E-02	4.38E-02	1.19E-01	1.31E-01
1.85E-01	5.04E-02	4.77E-02	4.56E-02	4.32E-02	4.02E-02	4.37E-02	9.81E-02	1.05E-01
2.51E-01	5.61E-02	5.33E-02	5.06E-02	4.76E-02	4.29E-02	4.71E-02	8.13E-02	6.74E-02
3.41E-01	5.63E-02	5.28E-02	4.98E-02	4.68E-02	4.56E-02	4.62E-02	6.90E-02	5.78E-02
4.64E-01	6.03E-02	5.58E-02	5.16E-02	4.71E-02	4.46E-02	4.74E-02	5.89E-02	5.08E-02
6.31E-01	7.53E-02	6.94E-02	6.45E-02	5.91E-02	5.56E-02	5.93E-02	4.93E-02	3.77E-02
8.58E-01	7.74E-02	7.43E-02	6.93E-02	6.37E-02	5.97E-02	6.39E-02	3.53E-02	2.33E-02
1.17E+00	8.54E-02	8.47E-02	8.16E-02	7.69E-02	7.38E-02	7.72E-02	2.20E-02	1.87E-02
1.58E+00	9.02E-02	9.17E-02	9.16E-02	8.94E-02	8.86E-02	9.05E-02	1.23E-02	1.51E-02
2.15E+00	9.13E-02	9.45E-02	9.75E-02	9.90E-02	1.00E-01	9.86E-02	8.68E-03	9.60E-03
2.93E+00	8.85E-02	9.23E-02	9.67E-02	1.03E-01	1.08E-01	1.00E-01	8.24E-03	2.15E-03
3.98E+00	7.56E-02	7.95E-02	8.38E-02	9.03E-02	9.79E-02	8.84E-02	6.37E-03	8.81E-04
5.41E+00	5.37E-02	5.66E-02	6.06E-02	6.65E-02	7.33E-02	6.55E-02	3.05E-03	4.21E-05
7.36E+00	9.55E-03	9.99E-03	1.07E-02	1.19E-02	1.34E-02	1.23E-02	5.07E-04	0.00E+00
1.00E+01	0.00E+00	0.00E+00	0.00E+00	0.00E+00	0.00E+00	0.00E+00	0.00E+00	0.00E+00

6MV 10cm × 10cm Modulated Spectra

Energy Bin	IMRT_13101	IMRT_13102	IMRT_13103	IMRT_13104	IMRT_13105	IMRT_13106	IMRT_13107	IMRT_13108	IMRT_13109
6.31E-03	5.77E-06	7.72E-06	7.11E-06	6.77E-06	6.49E-06	7.07E-06	7.65E-06	6.52E-06	7.12E-06
8.58E-03	1.78E-05	2.28E-05	2.15E-05	2.07E-05	2.10E-05	2.09E-05	2.11E-05	1.93E-05	2.18E-05
1.17E-02	4.15E-05	5.51E-05	5.46E-05	5.37E-05	5.27E-05	5.46E-05	5.30E-05	5.65E-05	5.42E-05
1.58E-02	8.45E-05	1.36E-04	1.45E-04	1.42E-04	1.43E-04	1.38E-04	1.37E-04	1.39E-04	1.47E-04
2.15E-02	1.56E-04	2.93E-04	3.56E-04	3.60E-04	3.61E-04	3.56E-04	3.75E-04	3.65E-04	3.85E-04
2.93E-02	3.31E-04	6.15E-04	8.31E-04	9.82E-04	1.13E-03	1.19E-03	1.29E-03	1.40E-03	1.50E-03
3.98E-02	1.18E-03	1.85E-03	2.74E-03	3.55E-03	4.72E-03	5.46E-03	6.05E-03	6.92E-03	7.91E-03
5.41E-02	3.21E-03	4.60E-03	6.72E-03	8.88E-03	1.17E-02	1.34E-02	1.50E-02	1.70E-02	1.95E-02
7.36E-02	5.84E-03	8.14E-03	1.17E-02	1.50E-02	1.90E-02	2.15E-02	2.36E-02	2.57E-02	2.79E-02
1.00E-01	9.58E-03	1.31E-02	1.81E-02	2.19E-02	2.62E-02	2.83E-02	3.02E-02	3.22E-02	3.41E-02
1.36E-01	1.61E-02	2.07E-02	2.67E-02	3.06E-02	3.41E-02	3.55E-02	3.68E-02	3.80E-02	3.84E-02
1.85E-01	2.87E-02	3.21E-02	3.75E-02	3.94E-02	4.05E-02	4.08E-02	4.11E-02	4.12E-02	4.12E-02
2.51E-01	4.40E-02	4.58E-02	5.07E-02	5.11E-02	5.07E-02	4.99E-02	4.93E-02	4.85E-02	4.61E-02
3.41E-01	4.79E-02	5.03E-02	5.49E-02	5.43E-02	5.24E-02	5.12E-02	5.00E-02	4.82E-02	4.61E-02
4.64E-01	5.16E-02	5.52E-02	6.07E-02	5.99E-02	5.74E-02	5.55E-02	5.36E-02	5.09E-02	4.71E-02
6.31E-01	6.29E-02	6.66E-02	7.19E-02	7.15E-02	6.87E-02	6.68E-02	6.47E-02	6.15E-02	5.74E-02
8.58E-01	7.92E-02	7.91E-02	8.09E-02	8.04E-02	7.75E-02	7.52E-02	7.30E-02	6.98E-02	6.46E-02
1.17E+00	9.43E-02	9.13E-02	8.76E-02	8.68E-02	8.53E-02	8.39E-02	8.27E-02	8.04E-02	7.62E-02
1.58E+00	1.18E-01	1.12E-01	1.01E-01	9.93E-02	9.82E-02	9.79E-02	9.70E-02	9.59E-02	9.33E-02
2.15E+00	1.27E-01	1.21E-01	1.12E-01	1.08E-01	1.06E-01	1.06E-01	1.06E-01	1.06E-01	1.07E-01
2.93E+00	1.17E-01	1.11E-01	1.06E-01	1.03E-01	1.02E-01	1.02E-01	1.03E-01	1.04E-01	1.08E-01
3.98E+00	1.05E-01	1.01E-01	9.28E-02	9.00E-02	8.95E-02	8.92E-02	8.94E-02	9.14E-02	9.68E-02
5.41E+00	7.20E-02	6.92E-02	6.45E-02	6.27E-02	6.22E-02	6.26E-02	6.37E-02	6.61E-02	7.16E-02
7.36E+00	1.65E-02	1.57E-02	1.29E-02	1.27E-02	1.24E-02	1.27E-02	1.32E-02	1.40E-02	1.52E-02
1.00E+01	0.00E+00	0.00E+00	0.00E+00	0.00E+00	0.00E+00	0.00E+00	0.00E+00	0.00E+00	0.00E+00

6MV 10cm × 10cm Modulated Spectra (Continued)

Energy Bin	IMRT_13110	IMRT_13201	IMRT_13202	IMRT_13203	IMRT_13204	IMRT_13205	IMRT_13206	IMRT_13207	IMRT_13208
6.31E-03	8.43E-06	7.25E-06	2.21E-06	1.92E-06	1.87E-06	1.54E-06	2.21E-06	3.12E-06	2.44E-06
8.58E-03	2.13E-05	2.15E-05	5.68E-06	5.46E-06	1.15E-05	8.84E-06	4.06E-06	1.67E-06	1.23E-05
1.17E-02	5.42E-05	5.27E-05	1.62E-05	1.47E-05	2.06E-05	3.26E-05	9.99E-06	1.63E-05	4.15E-06
1.58E-02	1.45E-04	1.29E-04	5.07E-05	2.77E-05	5.65E-05	5.08E-05	1.90E-05	6.08E-05	1.38E-05
2.15E-02	3.70E-04	2.69E-04	1.17E-04	1.07E-04	1.44E-04	1.91E-04	1.13E-04	1.33E-04	1.29E-04
2.93E-02	1.49E-03	5.63E-04	1.91E-03	2.10E-03	2.56E-03	2.34E-03	1.92E-03	1.93E-03	2.05E-03
3.98E-02	7.39E-03	1.83E-03	1.88E-02	2.45E-02	2.52E-02	2.41E-02	2.24E-02	2.06E-02	1.54E-02
5.41E-02	1.86E-02	4.54E-03	5.57E-02	7.11E-02	7.07E-02	6.60E-02	6.29E-02	6.18E-02	4.91E-02
7.36E-02	2.75E-02	8.08E-03	9.13E-02	1.07E-01	1.02E-01	9.72E-02	9.44E-02	8.97E-02	7.71E-02
1.00E-01	3.14E-02	1.26E-02	1.14E-01	1.25E-01	1.12E-01	1.07E-01	1.13E-01	1.04E-01	1.03E-01
1.36E-01	3.59E-02	1.97E-02	1.28E-01	1.25E-01	1.11E-01	1.03E-01	1.56E-01	1.18E-01	1.21E-01
1.85E-01	3.81E-02	3.09E-02	1.42E-01	1.22E-01	1.08E-01	1.02E-01	1.04E-01	1.11E-01	1.09E-01
2.51E-01	4.18E-02	4.53E-02	1.34E-01	1.14E-01	9.95E-02	9.55E-02	9.61E-02	1.05E-01	1.02E-01
3.41E-01	4.41E-02	5.29E-02	1.05E-01	8.84E-02	7.90E-02	8.08E-02	8.79E-02	9.64E-02	9.82E-02
4.64E-01	4.45E-02	5.98E-02	5.78E-02	4.83E-02	4.92E-02	4.84E-02	5.41E-02	6.83E-02	8.93E-02
6.31E-01	5.53E-02	7.23E-02	2.89E-02	2.35E-02	2.67E-02	3.30E-02	4.43E-02	5.27E-02	6.96E-02
8.58E-01	6.20E-02	7.87E-02	1.16E-02	1.48E-02	1.88E-02	2.42E-02	3.29E-02	4.87E-02	5.21E-02
1.17E+00	7.42E-02	9.56E-02	1.50E-02	1.89E-02	2.44E-02	3.22E-02	3.49E-02	4.96E-02	6.22E-02
1.58E+00	9.40E-02	1.05E-01	2.21E-02	2.78E-02	3.70E-02	4.25E-02	4.01E-02	3.97E-02	3.50E-02
2.15E+00	1.10E-01	1.16E-01	2.42E-02	3.41E-02	4.85E-02	5.23E-02	3.41E-02	2.02E-02	8.97E-03
2.93E+00	1.14E-01	1.13E-01	2.44E-02	3.23E-02	4.40E-02	4.29E-02	1.34E-02	7.78E-03	3.40E-03
3.98E+00	1.05E-01	9.70E-02	1.87E-02	1.68E-02	2.75E-02	2.65E-02	5.72E-03	3.29E-03	1.58E-03
5.41E+00	7.75E-02	7.53E-02	6.25E-03	4.05E-03	1.29E-02	1.83E-02	1.46E-03	5.54E-04	4.66E-04
7.36E+00	1.70E-02	1.11E-02	1.96E-04	4.45E-04	8.14E-04	1.49E-03	0.00E+00	0.00E+00	0.00E+00
1.00E+01	0.00E+00	0.00E+00	0.00E+00	0.00E+00	0.00E+00	0.00E+00	0.00E+00	0.00E+00	0.00E+00

6MV 10cm × 10cm Modulated Spectra (Continued)

Energy Bin	IMRT_13501	IMRT_13502	IMRT_13503	IMRT_13504	IMRT_13505	IMRT_13506	IMRT_13507	IMRT_13508	IMRT_13701
6.31E-03	6.62E-06	1.37E-06	1.12E-06	1.53E-06	2.29E-06	1.28E-06	2.27E-06	0.00E+00	7.19E-06
8.58E-03	2.09E-05	4.77E-06	5.69E-06	4.00E-06	1.09E-05	2.64E-06	4.15E-06	3.65E-06	2.18E-05
1.17E-02	5.22E-05	9.53E-06	1.30E-05	1.38E-05	2.03E-05	1.47E-05	2.65E-05	1.13E-05	5.95E-05
1.58E-02	1.35E-04	2.97E-05	2.83E-05	2.97E-05	4.63E-05	1.69E-05	2.23E-05	1.71E-05	1.52E-04
2.15E-02	3.34E-04	9.28E-05	7.60E-05	9.35E-05	1.11E-04	1.32E-04	7.69E-05	1.70E-04	3.53E-04
2.93E-02	1.03E-03	2.36E-03	3.12E-03	3.29E-03	3.16E-03	2.95E-03	3.05E-03	2.10E-03	1.47E-03
3.98E-02	4.60E-03	2.33E-02	3.22E-02	3.61E-02	3.48E-02	3.71E-02	3.20E-02	2.33E-02	8.34E-03
5.41E-02	1.17E-02	6.63E-02	8.68E-02	9.31E-02	8.96E-02	9.12E-02	8.54E-02	6.89E-02	2.04E-02
7.36E-02	1.94E-02	1.02E-01	1.26E-01	1.27E-01	1.19E-01	1.21E-01	1.15E-01	1.04E-01	3.01E-02
1.00E-01	2.70E-02	1.23E-01	1.34E-01	1.32E-01	1.20E-01	1.28E-01	1.23E-01	1.22E-01	3.53E-02
1.36E-01	3.52E-02	1.29E-01	1.29E-01	1.20E-01	1.06E-01	1.18E-01	1.18E-01	1.18E-01	3.86E-02
1.85E-01	4.34E-02	1.29E-01	1.18E-01	1.06E-01	9.71E-02	1.05E-01	1.07E-01	1.09E-01	4.05E-02
2.51E-01	5.40E-02	1.16E-01	9.90E-02	8.90E-02	8.23E-02	9.09E-02	9.73E-02	9.57E-02	4.45E-02
3.41E-01	5.82E-02	9.51E-02	8.09E-02	7.16E-02	7.11E-02	7.65E-02	8.52E-02	8.04E-02	4.47E-02
4.64E-01	6.18E-02	6.79E-02	5.52E-02	5.19E-02	4.63E-02	5.26E-02	5.75E-02	9.02E-02	4.61E-02
6.31E-01	7.21E-02	4.94E-02	3.39E-02	3.03E-02	2.99E-02	3.86E-02	4.51E-02	4.99E-02	5.66E-02
8.58E-01	7.28E-02	2.30E-02	1.37E-02	1.73E-02	2.03E-02	2.98E-02	3.88E-02	4.25E-02	6.11E-02
1.17E+00	8.82E-02	1.48E-02	1.27E-02	1.81E-02	2.38E-02	2.79E-02	3.37E-02	4.91E-02	7.64E-02
1.58E+00	9.39E-02	1.43E-02	1.73E-02	2.43E-02	3.16E-02	3.14E-02	2.94E-02	3.04E-02	8.98E-02
2.15E+00	9.90E-02	1.47E-02	2.16E-02	3.06E-02	4.17E-02	2.86E-02	1.92E-02	1.05E-02	1.02E-01
2.93E+00	9.82E-02	1.47E-02	2.08E-02	2.71E-02	3.87E-02	1.38E-02	7.98E-03	2.61E-03	1.10E-01
3.98E+00	8.58E-02	1.17E-02	1.17E-02	1.64E-02	2.39E-02	4.27E-03	2.52E-03	1.27E-03	1.01E-01
5.41E+00	6.36E-02	4.06E-03	3.09E-03	5.39E-03	1.85E-02	1.80E-03	2.14E-04	1.04E-04	7.97E-02
7.36E+00	9.55E-03	1.53E-04	2.93E-04	5.78E-04	1.64E-03	0.00E+00	0.00E+00	0.00E+00	1.19E-02
1.00E+01	0.00E+00	0.00E+00	0.00E+00	0.00E+00	0.00E+00	0.00E+00	0.00E+00	0.00E+00	0.00E+00

6MV 10cm × 10cm Modulated Spectra (Continued)

Energy Bin	IMRT_13702	IMRT_13703	IMRT_13704	IMRT_13705	IMRT_13706	IMRT_13707	IMRT_13708
6.31E-03	1.79E-06	1.61E-06	1.09E-06	1.79E-06	3.67E-06	2.38E-06	4.50E-07
8.58E-03	6.06E-06	5.03E-06	1.32E-06	4.92E-06	1.71E-06	1.12E-06	2.53E-06
1.17E-02	1.24E-05	9.25E-06	6.70E-06	1.16E-05	5.11E-06	2.28E-06	1.21E-05
1.58E-02	4.77E-05	3.37E-05	4.45E-05	1.99E-05	6.43E-05	7.37E-06	1.34E-06
2.15E-02	1.21E-04	4.61E-05	7.07E-05	1.24E-04	1.36E-04	2.80E-05	8.91E-06
2.93E-02	2.76E-03	3.62E-03	4.22E-03	3.86E-03	4.66E-03	4.46E-03	5.30E-03
3.98E-02	2.79E-02	3.89E-02	4.41E-02	4.59E-02	5.01E-02	5.72E-02	5.09E-02
5.41E-02	7.21E-02	9.85E-02	1.09E-01	1.13E-01	1.25E-01	1.37E-01	1.23E-01
7.36E-02	1.01E-01	1.27E-01	1.38E-01	1.50E-01	1.48E-01	1.71E-01	1.41E-01
1.00E-01	1.09E-01	1.28E-01	1.35E-01	1.32E-01	1.34E-01	1.41E-01	1.41E-01
1.36E-01	1.05E-01	1.15E-01	1.20E-01	1.14E-01	1.06E-01	1.06E-01	1.08E-01
1.85E-01	9.45E-02	9.70E-02	9.59E-02	8.59E-02	8.36E-02	8.12E-02	8.46E-02
2.51E-01	8.63E-02	8.05E-02	8.08E-02	7.03E-02	7.44E-02	6.40E-02	9.45E-02
3.41E-01	7.91E-02	7.24E-02	6.70E-02	6.30E-02	5.88E-02	5.89E-02	6.64E-02
4.64E-01	6.88E-02	6.25E-02	5.74E-02	5.06E-02	5.30E-02	5.23E-02	5.41E-02
6.31E-01	6.57E-02	5.42E-02	4.78E-02	3.85E-02	4.03E-02	3.24E-02	4.15E-02
8.58E-01	5.35E-02	4.11E-02	3.23E-02	2.71E-02	2.56E-02	2.61E-02	2.45E-02
1.17E+00	4.55E-02	3.02E-02	2.10E-02	1.90E-02	1.83E-02	2.41E-02	2.50E-02
1.58E+00	3.56E-02	2.00E-02	1.45E-02	1.64E-02	1.86E-02	1.97E-02	2.02E-02
2.15E+00	2.53E-02	1.25E-02	1.27E-02	2.10E-02	2.18E-02	1.52E-02	1.32E-02
2.93E+00	1.61E-02	9.10E-03	1.07E-02	2.10E-02	1.84E-02	7.46E-03	4.23E-03
3.98E+00	7.64E-03	6.51E-03	6.56E-03	1.83E-02	1.06E-02	2.46E-03	2.83E-03
5.41E+00	2.99E-03	2.92E-03	2.61E-03	9.62E-03	7.01E-03	8.55E-04	3.81E-04
7.36E+00	1.06E-04	1.05E-04	3.02E-04	5.89E-04	1.11E-03	0.00E+00	0.00E+00
1.00E+01	0.00E+00	0.00E+00	0.00E+00	0.00E+00	0.00E+00	0.00E+00	0.00E+00

Energy Correction Factors for TLD and OSLD for non-reference conditions in 6MV beam

6MV 10cm × 10cm Open Field Spectra Non-Reference Energy Correction Factors

Spectrum ID	Average Spectral Energy (MeV)	k _{PE} TLD	k _E OSLD
10_13101	1.56	1.00	1.00
10_13102	1.49	1.00	1.00
10_13103	1.45	1.00	1.00
10_13104	1.41	1.00	1.00
10_13105	1.40	1.00	1.00
10_13106	1.39	1.00	0.99
10_13107	1.40	1.00	0.99
10_13108	1.42	1.00	0.99
10_13109	1.46	1.00	0.99
10_13110	1.53	1.00	0.99
10_13201	1.39	1.00	1.00
10_13202	0.41	0.98	0.91
10_13203	0.40	0.98	0.88
10_13204	0.46	0.98	0.89
10_13205	0.43	0.98	0.89
10_13206	0.38	0.98	0.88
10_13207	0.29	0.97	0.85
10_13208	0.29	0.97	0.86
10_13501	1.32	1.00	0.99
10_13502	0.35	0.98	0.89
10_13503	0.31	0.97	0.84
10_13504	0.36	0.97	0.85
10_13505	0.35	0.97	0.84
10_13506	0.30	0.96	0.83
10_13507	0.26	0.96	0.81
10_13508	0.25	0.96	0.82
10_13701	1.44	1.00	0.99
10_13702	0.42	0.98	0.91
10_13703	0.31	0.97	0.85
10_13704	0.28	0.96	0.81
10_13705	0.27	0.96	0.80
10_13706	0.26	0.95	0.78
10_13707	0.24	0.95	0.77
10_13708	0.22	0.95	0.76

6MV 5cm × 5cm Open Field Spectra Non-Reference Energy Correction Factors

Spectrum ID	Average Spectral Energy (MeV)	k _{PE} TLD	k _E OSLD
5_13101	1.69	1.00	1.00
5_13102	1.65	1.00	1.00
5_13103	1.64	1.00	1.00
5_13104	1.65	1.00	1.00
5_13105	1.68	1.00	1.00
5_13106	1.70	1.00	1.00
5_13107	1.73	1.00	1.00
5_13108	1.77	1.00	1.00
5_13109	1.85	1.00	1.00
5_13110	1.94	1.00	1.00
5_13201	0.56	0.99	0.96
5_13202	0.57	0.99	0.94
5_13203	0.72	0.99	0.94
5_13204	0.84	0.99	0.95
5_13205	0.62	0.99	0.93
5_13206	0.38	0.98	0.89
5_13207	0.30	0.97	0.88
5_13208	0.31	0.98	0.90
5_13501	0.50	0.99	0.95
5_13502	0.45	0.98	0.91
5_13503	0.54	0.98	0.90
5_13504	0.66	--	0.92
5_13508	0.26	0.96	0.84
5_13701	0.66	0.99	0.96
5_13703	0.40	0.97	0.87
5_13708	0.23	0.95	0.77

6MV 20cm × 20cm Open Field Spectra Non-Reference Energy Correction Factors

Spectrum ID	Average Spectral Energy (MeV)	k _{PE} TLD	k _E OSLD
20_13101	1.38	1.00	1.00
20_13102	1.29	1.00	0.99
20_13106	1.06	1.00	0.98
20_13109	1.03	--	0.97
20_13110	1.08	1.00	0.98
20_13201	1.28	1.00	0.99
20_13207	0.21	0.95	0.77
20_13208	0.26	0.96	0.83
20_13501	1.15	1.00	0.99
20_13503	0.22	0.96	0.81
20_13504	0.20	0.95	0.76
20_13508	0.22	0.95	0.77
20_13701	1.04	1.00	0.97
20_13703	0.32	0.97	0.86
20_13704	0.23	0.95	0.79
20_13706	0.19	0.94	0.72
20_13708	0.17	0.93	0.69

6MV 10cm × 10cm Open Field Spectra with Lung Heterogeneity Non-Reference Energy Correction

Factors

Spectrum ID	Average Spectral Energy (MeV)	k _{PE} TLD	k _E OSLD
10_13106L	1.50	1.00	1.00
10_13107L	1.44	1.00	1.00
10_13108L	1.39	1.00	0.99
10_13109L	1.39	1.00	0.99
10_13110L	1.45	1.00	0.99
10_13701L	1.39	1.00	0.99
10_13704L	0.30	0.96	0.83
10_13708L	0.24	0.95	0.79

6MV 10cm × 10cm Open Field Spectra with Bone Heterogeneity Non-Reference Energy Correction

Factors

Spectrum ID	Average Spectral Energy (MeV)	k _{PE} TLD	k _E OSLD
10_13106B	1.35	1.00	1.00
10_13107B	1.39	1.00	0.99
10_13108B	1.43	1.00	0.99
10_13109B	1.49	1.00	0.99
10_13110B	1.56	1.00	0.99
10_13701B	1.48	1.00	0.99
10_13704B	0.29	0.96	0.82
10_13708B	0.22	0.95	0.76

6MV 10cm × 10cm Modulated Spectra Non-Reference Energy Correction Factors

Spectrum ID	Average Spectral Energy (MeV)	k _{PE} TLD	k _E OSLD
IMRT_13101	1.74	1.00	1.00
IMRT_13102	1.68	1.00	1.00
IMRT_13103	1.57	1.00	1.00
IMRT_13104	1.54	1.00	1.00
IMRT_13105	1.52	1.00	1.00
IMRT_13106	1.52	1.00	1.00
IMRT_13107	1.52	1.00	1.00
IMRT_13108	1.54	1.00	0.99
IMRT_13109	1.59	1.00	0.99
IMRT_13110	1.67	1.00	1.00
IMRT_13201	1.66	1.00	1.00
IMRT_13202	0.41	0.98	0.91
IMRT_13203	0.43	0.98	0.90
IMRT_13204	0.58	0.99	0.92
IMRT_13205	0.63	0.99	0.93
IMRT_13206	0.39	0.98	0.90
IMRT_13207	0.37	0.98	0.91
IMRT_13208	0.36	0.98	0.92
IMRT_13501	1.47	1.00	1.00
IMRT_13502	0.34	0.97	0.88
IMRT_13503	0.34	0.97	0.86
IMRT_13504	0.41	0.98	0.87
IMRT_13505	0.56	0.98	0.91
IMRT_13506	0.35	0.97	0.86
IMRT_13507	0.32	0.97	0.86
IMRT_13508	0.32	0.97	0.88
IMRT_13701	1.61	1.00	0.99
IMRT_13702	0.42	0.98	0.90
IMRT_13703	0.32	0.97	0.85
IMRT_13704	0.30	0.96	0.82
IMRT_13705	0.40	0.97	0.85
IMRT_13706	0.36	0.97	0.83
IMRT_13707	0.26	0.95	0.78
IMRT_13708	0.26	0.96	0.80

Vita

Sarah Brashear Scarboro was born in Plattsburgh, New York on January 23, 1984, the daughter of Steven and Katherine Brashear. After completing high school at Albemarle High School, Charlottesville, Virginia in 2002, she entered Georgia Institute of Technology in Atlanta, Georgia. She graduated with Highest Honors with a Bachelor of Science in Nuclear and Radiological Engineering in December 2006. She continued in the Medical Physics program at Georgia Institute of Technology, and received a Master's of Science in Medical Physics in May 2008. In August of 2008 she entered The University of Texas Health Science Center at Houston Graduate School of Biomedical Sciences. Sarah is married to Paul R. Scarboro, Jr, and they have one son, Asher Leo Scarboro, born on January 5, 2011.

Permanent address:
99 Claymont Drive
Earlysville, VA 22936